**TÜRKİYE CUMHURİYETİ**
**ADANA ALPARSLAN TÜRKEŞ SCIENCE AND TECHNOLOGY UNIVERSITY**

**GRADUATE SCHOOL**
**ELECTRICAL AND ELECTRONIC ENGINEERING DEPARTMENT**

# DESIGN AND MODELING OF MULTIPORT DC-DC CONVERTER FOR RENEWABLE ENERGY SOURCES AND ENERGY STORAGE INTEGRATED SYSTEM

**Alihan ATAY**

**M.Sc.**

**ADANA YEAR**

**TÜRKİYE CUMHURİYETİ**
**ADANA ALPARSLAN TÜRKEŞ SCIENCE AND TECHNOLOGY UNIVERSITY**

**GRADUATE SCHOOL**
**ELECTRICAL AND ELECTRONIC ENGINEERING DEPARTMENT**

# DESIGN AND MODELING OF MULTIPORT DC-DC CONVERTER FOR RENEWABLE ENERGY SOURCES AND ENERGY STORAGE INTEGRATED SYSTEM

**Alihan ATAY**

**M.Sc.**

**THESIS ADVISOR**
**Assoc. Prof. Dr. M. Mustafa SAVRUN**

**ADANA, 2023**

# ÖZET


## YENİLENEBİLİR ENERJİ KAYNAKLARI VE ENERJİ DEPOLAMA ENTEGRE SİSTEMLERİ İÇİN ÇOK PORTLU DC-DC DÖNÜŞTÜRÜCÜ TASARIMI VE MODELLEMESİ

Alihan ATAY

Yüksek Lisans, Elektrik-Elektronik Anabilim Dalı

Danışman: Doç Dr. M. Mustafa SAVRUN

07 2023, 90 sayfa

Bu tezde, yenilenebilir enerji sistemleri (YES), enerji depolama sistemleri ve yüklerin entegrasyonunu, birbirleri arasında optimum güç akışını mümkün kılan çok-portlu DA-DA dönüştürücü ve kontrol şemaları üzerine tasarım ve modelleme çalışmaları gerçekleştirilmiştir. Bu kapmsada, farklı dönüştürücü modelleri geliştirilmiş olup, YES ünitelerinde maksimum güç noktasının takibinin yapılabilmesi, enerji depolama ünitelerinde standartlara uygun şarj algoritmalarının uygulanabilmesi, yüklere kesintisiz güç sağlanabilmesi, ve çift yönlü güç akışının sağlanabilmesi amaçlanmıştır.

Bu amaçlara yönelik olarak, tez kapsamında dört farklı çok-portlu DA-DA dönüştürücü topolojisi ve kontrolcüsü tasarlanmış ve modellenmiştir. Tasarım aşamasında topolojilerin matematiksel hesaplamaları gerçekleştirilmiş, kontrol şemaları ve anahtarlama durumları derinlemesine incelenmiş ve sunulmuştur. Önerilen dönüştürücüler, MATLAB/Simulink ve PSIM ortamlarında geliştirilmiş ve olası tüm güç akış senaryolarında sistem performansları test edilmiştir. Gerçekleştirilen performans inceleme çalışmaları neticesinde tasarımı gerçekleştirilen tüm dönüştürücü topoloji/kontrolcülerinin etkinliği ve uygulanabilirliği doğrulanmıştır.



**Anahtar Kelimeler:** Çok portlu Dönüştürücü, DA-DA Dönüştürücü, FV Panel, Batarya, Çift yönlü güç akışı

# ABSTRACT

## DESIGN AND MODELING OF MULTIPORT DC-DC CONVERTER FOR RENEWABLE ENERGY SOURCES AND ENERGY STORAGE INTEGRATED SYSTEM

Alihan ATAY

M.Sc., Department of Electric-Electronics

Supervisor: Assoc. Prof. Dr. M. Mustafa SAVRUN

07 2023, 90 pages

In this thesis, design and modeling studies have been conducted on multiport DC-DC converters and control schemes that enable the integration of renewable energy systems (RES), energy storage systems, and loads, allowing for optimal power flow between them. Within this scope, different converter models have been developed to achieve the following objectives: tracking the maximum power point in RES units, implementing standardized charging algorithms for energy storage units, providing uninterrupted power supply to the loads, and enabling bidirectional power flow.

To achieve these objectives, four different multiport DC-DC converter topologies and their controllers have been designed and modeled in the thesis. During the design phase, the mathematical calculations of the topologies have been performed, and the control schemes and switching states have been thoroughly investigated and presented. The proposed converters have been developed in MATLAB/Simulink and PSIM environments, and their performance was tested in all possible power flow scenarios. Through the conducted performance analysis, the efficiency, and applicability of all designed converter topologies/controllers have been validated.

**Keywords:** Multiport Converters, DC-DC Converters, PV Panel, Battery, Bidirectional Power Flow

*Dedication*

*Kıymetli Eşim ve Aileme.*

# ACKNOWLEDGEMENTS

I would like to express my heartfelt thanks to my supervisor Assoc. Prof. Dr. M. Mustafa SAVRUN for his supervision, guidance, encouragements and extremely useful suggestions throughout this thesis. It has been a great honor to have Assoc. Prof. Dr. M. Mustafa SAVRUN as supervisor.

I would like to thank Dr. A. Özgür POLAT and Dr. Bülent BÜYÜKGÜZEL for their support and guidance.

I would like to thank to Assoc. Prof. Dr. Mehmet Uğraş CUMA and Asst. Prof. Dr. Tahsin KÖROĞLU for accepting to be the member of examining committee for my thesis.

I would like to thank my family, my nephew and childhood friends for their encouragement and faith in me during my thesis.

Finally, I would like to convey my heartfelt appreciation to my wife, Şevval ATAY for her encouragement, support, and inspiration.

# TABLE OF CONTENS

# LIST OF FIGURES

# LIST OF TABLES

# LIST OF ABBREVIATIONS

| | |
|---|---|
| AC | : Alternative Current |
| CC | : Constant Current |
| CCM | : Continuous Conduction Mode |
| CV | : Constant Voltage |
| DAB | : Dual Active Bridge |
| DC | : Direct Current |
| EM | : Electric Motor |
| ESU | : Energy Storage Unit |
| EV | : Electric Vehicle |
| HFT | : High Frequency Transformer |
| MPC | : Multiport Converter |
| MPPT | : Maximum Power Point Tracking |
| P&O | : Perturb And Observe |
| PI | : Proportional Integral |
| PV | : Photovoltaic |
| PWM | : Pulse Width Modulation |
| qZ_iMPC | : Quasi Z Source Multiport Converter |
| qZ_RiMPC | : Resonant Tank Integrated Isolated Quasi Z-Source Multiport Converter |
| qZSI | : Quasi Z Source Inverter |
| RES | : Renewable Energy Source |
| UPS | : Uninterruptible Power Supply |
| V2G | : Vehicle to Grid |
| ZVS | : Zero Voltage Switching |

# LIST OF SYMBOLS

| | |
|---|---|
| ø | : Phase Shift Angle |
| $C_{out}$ | : Output Capacitor |
| $C_r$ | : Series Capacitor |
| $f_r$ | : Resonant Frequency |
| $f_{sw}$ | : Switching Frequency |
| D | : Duty Cycle |
| $I_b$ | : Battery Current |
| $I_{berror}$ | : Battery Current Error |
| $I_{bref}$ | : Battery Reference Current |
| $I_{pv}$ | : Photovoltaic Current |
| $L_r$ | : Series Inductor |
| $P_{EM}$ | : Electric Motor Power |
| $P_{ESU}$ | : Energy Storage Unit Power |
| $P_{pv}$ | : PV Power |
| Q | : Quality Factor |
| $T_s$ | : Switching Cycle |
| $V_{bat}$ | : Battery Voltage |
| $V_{berror}$ | : Battery Voltage Error |
| $V_{bref}$ | : Battery Voltage Reference |
| $V_{Cq1}$ | : $C_{q1}$ Capacitor Voltage |
| $V_{Cq2}$ | : $C_{q2}$ Capacitor Voltage |
| $V_{D2}$ | : $S_2$ Switching Element Freewheeling Diode Voltage |
| $V_{dc}$ | : DC-Link Voltage |
| $V_{dcref}$ | : DC-Link Voltage Reference |
| $V_{Lq1}$ | : $L_{q1}$ Inductor Voltage |
| $V_{Lq2}$ | : $L_{q2}$ Inductor Voltage |
| $V_{out}$ | : Output Voltage |
| $V_{PN}$ | : Quasi Z-Source Converter Voltage |
| $V_{pv}$ | : Photovoltaic Voltage |
| $V_s$ | : Supercapacitor Voltage |

# 1. INTRODUCTION

The so-called "traditional energy sources" of so-called fossil fuels have been progressively running out for about 25 years. Additionally, because of rising greenhouse gas emissions, they are becoming economically outdated and their carbon impact is expanding daily. These elements have sparked a rise in demand for RES on a worldwide scale[1], [2]. Although RES are not as commonly employed as conventional energy sources, technical advancements have considerably increased their application in distributed generation systems, microgrids, and electric vehicles (EVs).

However, the capacity and availability of power produced by RES is unpredictable because to shifting environmental variables as wind speed and sun radiation/temperature. As a result, RES and energy storage units (ESUs) are frequently used together to produce continuous electricity. Furthermore, because RESs cannot retain the energy they produce, they must be linked to load and ESUs. ESUs may store energy produced by RESs and then transmit it to loads.

The maximum power point tracking (MPPT) algorithm is required to enable wind and solar energy sources to generate their maximum power. At this point, power electronic systems are needed for the commercial utilization and maximum power point tracking of RESs. Systems that can operate the MPPT algorithm and control the DC-Link voltage are frequently employed in DC-DC converter or DC-AC converter systems. ESUs are no longer a choice, but rather a requirement as RES energy systems become more and more integrated with the infrastructure. Multiport converters (MPCs) are frequently employed in systems with several energy sources or energy storage components to provide power flow.

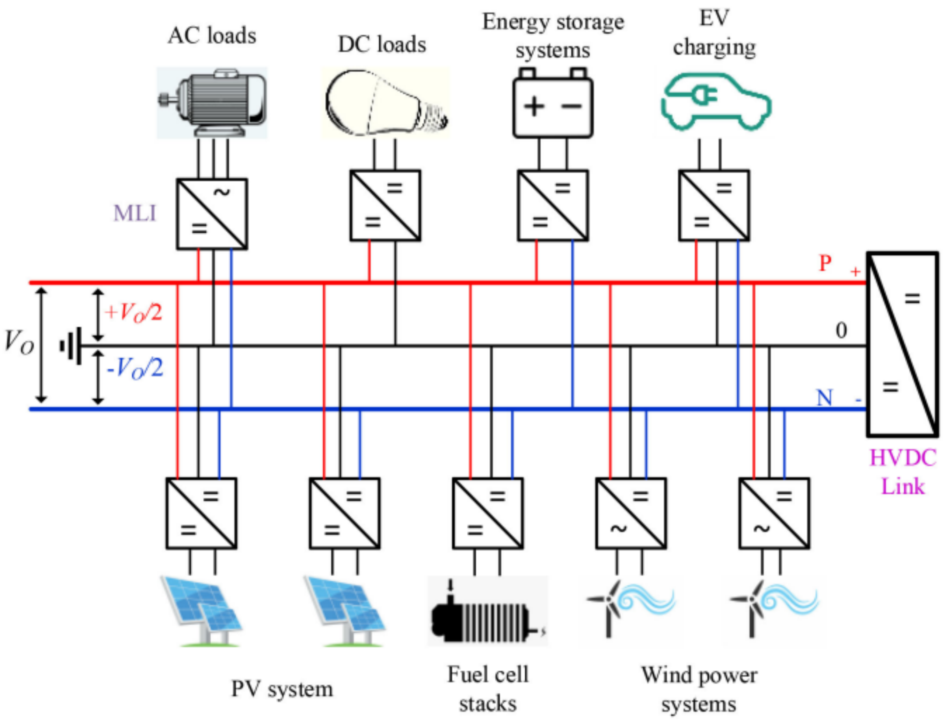


**Figure 1.1.** Conventional Multiport Converter[3]

Traditional multiport converters need independent power electronic converters for each port to accomplish regulate the power flow. As seen in Figure 1.1, unidirectional DC-DC or AC-DC converters are needed for RESs like photovoltaics (PVs) and wind turbines, whereas bidirectional DC-DC converters are employed for ESUs. Individual power electronic converters raise the system's total cost and complexity. Researchers have lately conducted extensive literature study on a new generation of multiport DC-DC converters that incorporate ESUs and RESs to accomplish this address these drawbacks.

EVs employ multiport converters[4] to regulate the power flow between various energy sources and loads. An EV often contains several loads, such as auxiliary systems, as well as various energy sources, including a battery pack and a motor. To manage the power flow between these numerous sources and loads, a multiport converter can be employed. Depending on the operating conditions, multi-port converters can execute a number of functions. For example, it can convert DC power from the battery pack into AC power for the motor while also charging the battery with the excess power from the motor. Bidirectional power flow is what this is known as, and it uses the available energy more effectively. The multiport converter also serves the purpose of connecting to outside power sources, such as a wallbox or a charging station, to charge the battery pack. To accomplish this, perform the related power transfer, the converter is needed to be equipped with AC-to-DC conversion capability [5]. In a hybrid or EV, multiport converters can also be utilized to control the power flow between several motors. For this to be possible, the converter must be able to independently adjust the torque and speed of each motor. The multiport converter, which offers effective power management between various energy sources and loads, contributes significantly to the operation and effectiveness of EV overall.

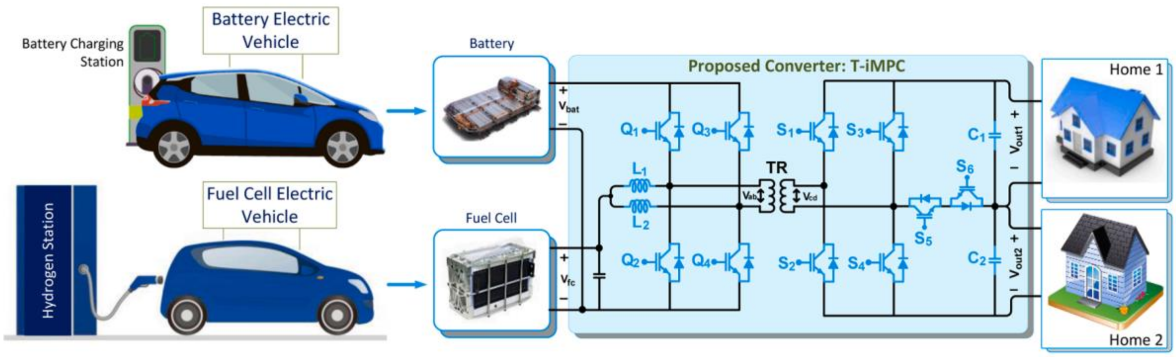


**Figure 1.2** Multiport Converter in EV [6]

In microgrid systems, multiport converters are also utilized to regulate the power flow between various sources and loads. A small collection of electrical sources and loads that may function independently from the main grid is known as a microgrid. Both traditional energy sources like diesel generators or batteries and RES like solar cells or wind turbines can be used as sources. In application areas such as vehicle-to-grid(V2G)[7], multiport converters allow energy to Flow in both ways, from source to load and load to source. To guarantee that the power delivered to loads is steady and dependable, the multiport converter may also provide voltage and frequency control. In order to maintain a high degree of power efficiency, it may also provide power quality management. Additionally, when necessary, microgrids may be linked to the broader power grid via multiport converters. This is crucial for times when the microgrid is unable to fulfill the demand for power and must draw extra power from the grid. In conclusion, multiport converters are essential to the administration and operation of microgrid systems because they enable effective power transfer between various sources and loads while preserving power quality and stability.

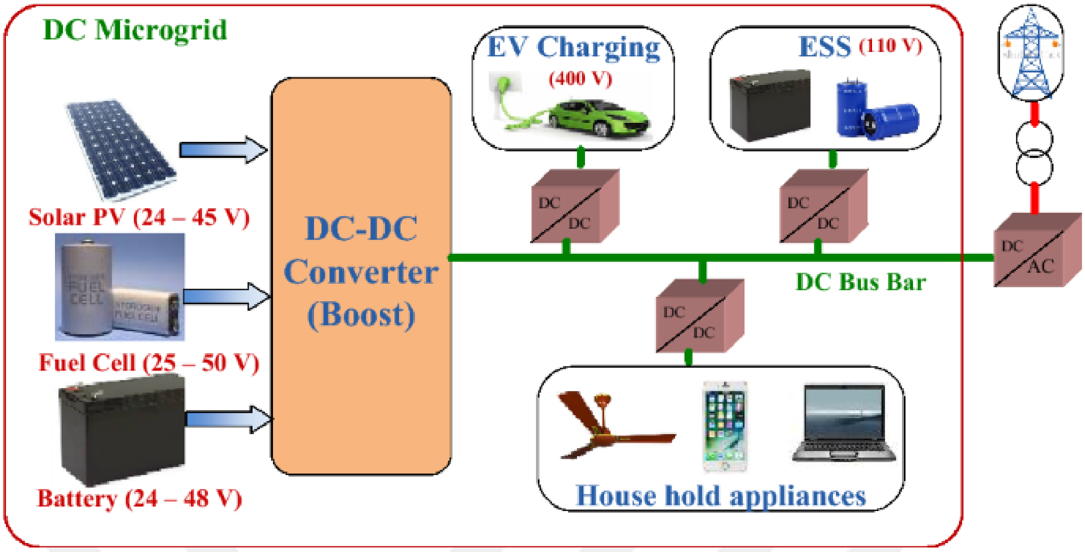


**Figure 1.3** Multiport Converter in Microgrid [8]

### 1.1. Scope of Thesis

This thesis presents the design and modeling of multiport converters powered by ESUs and RESs. In many diverse application areas, including microgrid, EV with RESs, and ESUs, multiport converters are typically selected. For this reason, research has been done and reported in this thesis in a variety of application areas. Additionally, the RES is compensated by charging and discharging the ESU to provide various power flow scenarios when the generating capacity is insufficient or the RES is able to supply all the power needed by the load.

In simulation environments like PSIM and MATLAB/Simulink, control algorithms for MPPT in RESs, constant current(CC) constant voltage(CV) charging/discharging of ESUs, and reverse power transfer referred to in the studies as regenerative braking are developed and verified. Different power circuits can be integrated with one another to build multiport converters. But at this stage, a lot of switching components are required. The number of switching elements is decreased by utilizing shared switching elements among the power circuits as opposed to separate switching elements in each power circuit.

## 1.2. Contributions of the Thesis

The following unique contributions to the literature and application of multiport DC-DC converters are made by this thesis.

- Different DC-DC or DC-AC converter topologies are integrated on top of each other to form conventional multiport converters.
- Bidirectional power transmission, CC, CV charge control, DC-Link control and MPPT control algorithm on the same switching elements are controlled from a single control center.
- Two separate load ports that are provided in the interleaved based isolated multiport converter architecture can be controlled independently.
- The switched capacitor multiport converter circuit offers high gain and is recommended for use in low voltage solar panel microgrid applications.
- The multiport converter, which is based on a quasi-Z-source converter, provides significant voltage gain while using a low input battery/supercapacitor voltage and a lower duty cycle.
- A full bridge rectifier and Quasi-z source and interleaved isolated MPC topology using the same switching elements are proposed.
- A resonant tank system is integrated into the Quazi Z-Source multiport converter topology to enhance the efficiency of the system.
- In the Resonant Tank Quasi Z-Source topology, the supercapacitor is charged/discharged under different operating conditions with the switching element added to the quasi z-source circuit.

## 1.3. Outline of the Thesis

The general structure of the thesis is as follows:

Chapter 1 includes an overview of multiport converters and an introduction to the reasons for their necessity. The scope of the thesis is outlined, and the thesis contributions are mentioned. In Chapter 2, a literature review on multiport converters is presented. Multiport converter topologies and control algorithms are analyzed. In Chapter 3, the power circuit designs and calculations of the multiport converters are presented. In Section 4, the control algorithms of the multiport converters are presented. In Section 5, simulation studies, results of different case studies and performance analysis of the multiport converter topologies are presented.

# 2. THEORETICAL FOUNDATIONS AND LITERATURE REVIEW

Multiport converters are the development of conventional DC-DC or DC-AC converters. DC-DC converters are divided into different classes as seen in Figure 2.1. DC-DC converters are selected according to their suitability for different power applications and usage areas. Isolated DC-DC converter topologies are generally utilized in applications where isolation between input and output is required or in applications above a certain power.

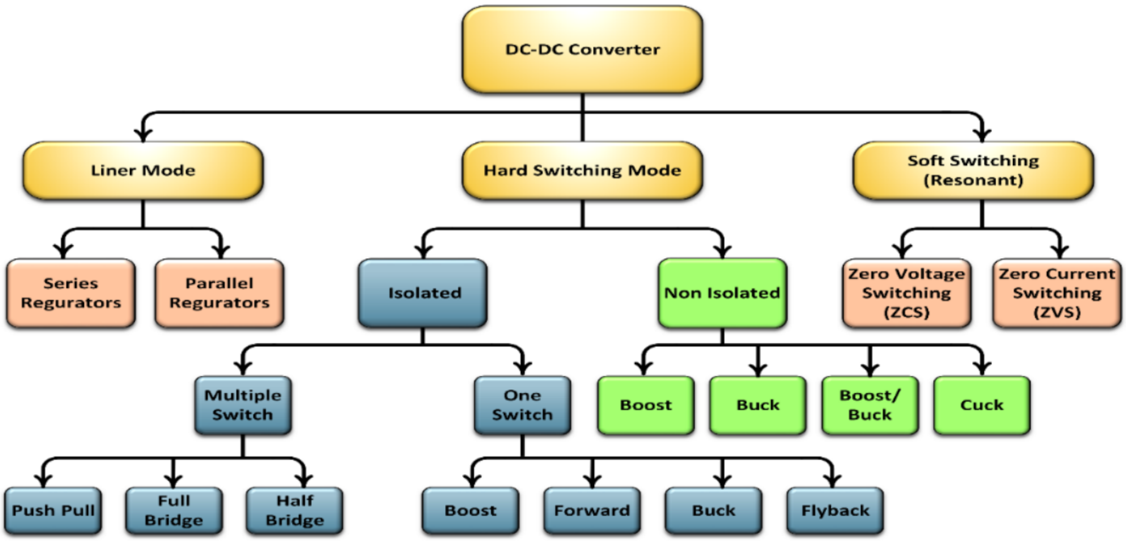


**Figure 2.1** DC-DC Converter Topology Classification [9]

Multiple converter integrations can provide connection ports for RES, ESUs, and loads. However, the system price tag and control complexity grow. To mitigate the aforementioned adverse effects, systems can be integrated at a single location utilizing multiport converters.

Multiport converters may be equipped with either isolated or non-isolated DC-DC converter topologies according to the classifications above since they are endowed with various RESs, ESUs, and loads. The major goal of creating non-isolated topologies is to increase efficiency while lowering cost and control complexity by minimizing the number of switching elements. The major goals of building isolated topologies are efficient operation at greater powers and variable voltage ranges for power flow routing.

## 2.1. Classification of Multiport DC-DC Converter Topologies

Multiport converters are classified into three categories:

- Non-isolated topologies, in which each port is coupled to a single ground line,
- Partially isolated topologies are topologies in which some ports are linked to the same ground while the rest ports are connected to a different ground.
- Completely isolated topologies are topologies in which all ports are connected to distinct ground lines.

Non-isolated topologies, which are often employed in low and medium power applications, are developed from conventional DC-DC converter topologies. Because there is no high frequency transformer (HFT), non-isolated topologies have the benefit of being simpler and more compact, but they are unable to offer isolation and a wide voltage range. By offering a wide voltage range with the turns ratio of the HFT, fully and partially isolated multiport converters may handle energy sources and storage units with varying wide voltage levels.

### 2.1.1 Non-Isolated Multiport Converter Topologies

The non-isolated MPC are the subject of this section. Non-isolated multiport converters are typically referred to as multi-input or multi-output devices in the literature. The energy source is varied in multi-input topologies to increase the utilization of RESs or ESUs. The outputs of RESs are in DC format. Therefore, a multi-input DC-DC converter can be used practically. Figure 2.2 shows the topology of a multi-input buck-boost converter [10].

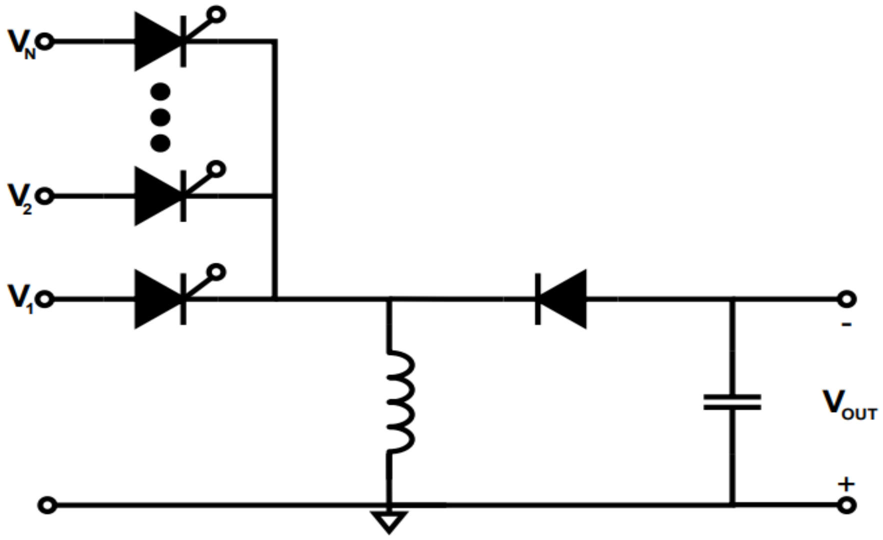


**Figure 2.2** Multi-input Buck-Boost Converter[10]

The topology illustrated in Figure 2.2 is reproduced from a parallel-connected buck-boost converter architecture that utilizes a shared inductor and an output capacitor. RESs like PVs, fuel cells, and ESUs like batteries and supercapacitors can all be attached to the input ports. The converter's output is negatively referenced, as is evident from Figure 2.2. However, they contain inputs that enable the terminals of the energy sources and ESU to be switched in the other direction. Because of the risk of overcurrent in a multi-input DC-DC converter architecture, the sources cannot transfer power to the load simultaneously. Consequently, the multi-input buck-boost converter architecture has a very restricted use.

As seen in Figure 2.3, a multi-input interleaved DC-DC converter[11], [12] architecture is suggested. The architecture uses an interleaved boost DC-DC converter to link the input ports to a single DC bus. The topology's input ports are not isolated, despite the fact that the topology's AC output port is.

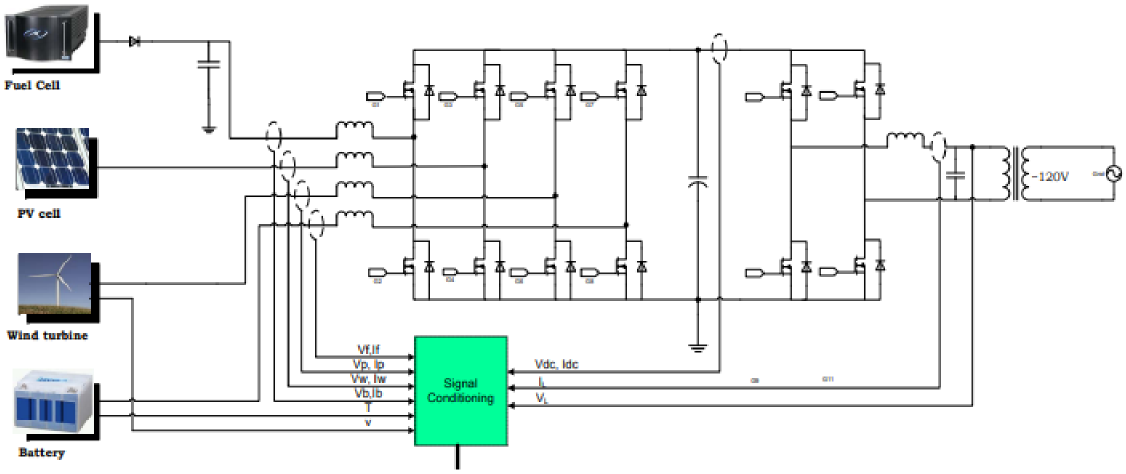


**Figure 2.3** Interleaved Boost Converter-Based MPC[11]

The ports in the architecture shown in Figure 2.3 cannot transfer power simultaneously. When two energy sources are put into conduction at the same time, power transfer can occur between them. The ports can transfer power with some phase variations in this architecture. It thus increases control complexity. A control algorithm that works for various power circumstances must be created. Continuous power cannot be obtained from the input ports, especially in the case of discontinuous energy sources like RESs. In this scenario, the DC-Link voltage stability may worsen. Additionally, the DC-Link voltage can be maintained by constructing a high-capacity DC-link, but a costly DC-Link line is produced in the process.

A multi-input DC-DC converter's structure is illustrated in Figure 2.4 [13]. In this design, the capacitive coupling circuit of a typical boost DC-DC converter combines two separate energy sources.

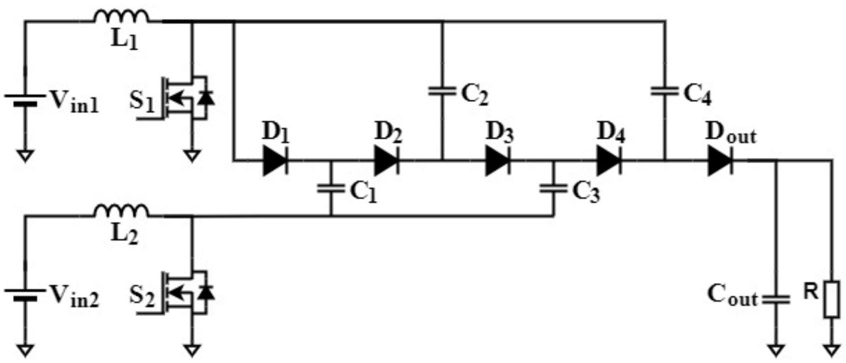


**Figure 2.4** Capacitive Coupling Multiport DC-DC Converter[13]

The charge pump operation of the capacitive coupling circuit in Figure 2.4 allows enhancing the output voltage using a high gain DC-DC converter. In the topology, each input port may transmit unidirectional power without relying on the other. However, due to the power transmission of this architecture through the capacitors, the capacitors utilized at the point of application degrade quickly.

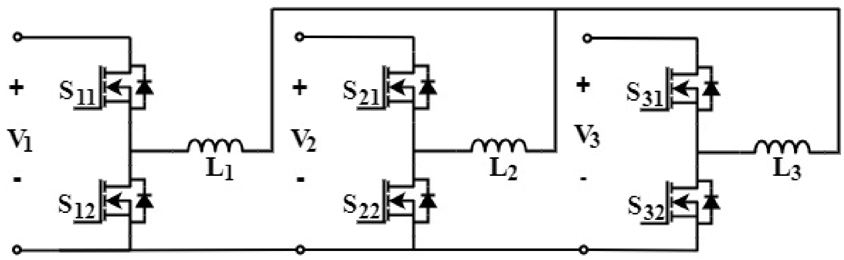


**Figure 2.5** Three Port Non-Isolated DC-DC Converter [14][15]

A three-port non-isolated converter is seen in Figure 2.5. Each port is created using an established buck converter architecture. At the halfway of the leg, where the two switching components are situated, a coil is put in each port. The planned three-port non-isolated converters' coils are connected to create the DC-Link line. Single input, dual output, and dual input single output are the two operational modes available.

The advantages of a three-port non-isolated converter are: Instead of several independent DC-DC converters, it can transfer power through three different ports that can work together independently of each other. It can smoothly switch between CC and CV control mode.

The switching element is under a lot of stress, and sophisticated modulation techniques and controller design are drawbacks. The sources that must be linked to at least two of the active ports must be capable of bidirectional transmission.

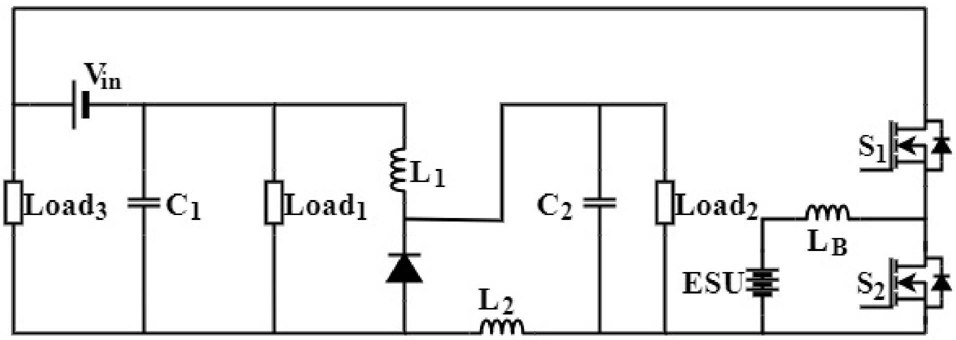


**Figure 2.6** Switch-Leg Based Multiport Converter[16]

The multiport converter seen in Figure 2.6 is composed of a source port, an ESU, and three load ports. A bidirectional buck-boost converter integrates the ESU with the other ports. Depending on its status during charging and discharging, the ESU can operate in one of two alternative ways. The buck-boost converter works in buck mode when the ESU is being charged, and it operates in boost mode when the ESU is being discharged. As a result, load 3 has a greater voltage level than the source port and other ports.

The advantages of this topology include significant cost reduction by having only two switching elements, simplicity of the control mechanism, and absence of algorithmic overlap.

The drawbacks of this topology are that it cannot be connected to a load that is sensitive to a voltage of load 3 due to high capacitor values and high switching element voltage, and the switching elements in the system cannot be operated with software switches.

### 2.1.2 Partially Isolated Multiport DC-DC Converter

This section offers the subject of Partial isolated topologies.  Topologies that have certain ports galvanically separated are said to be partially isolated topologies.

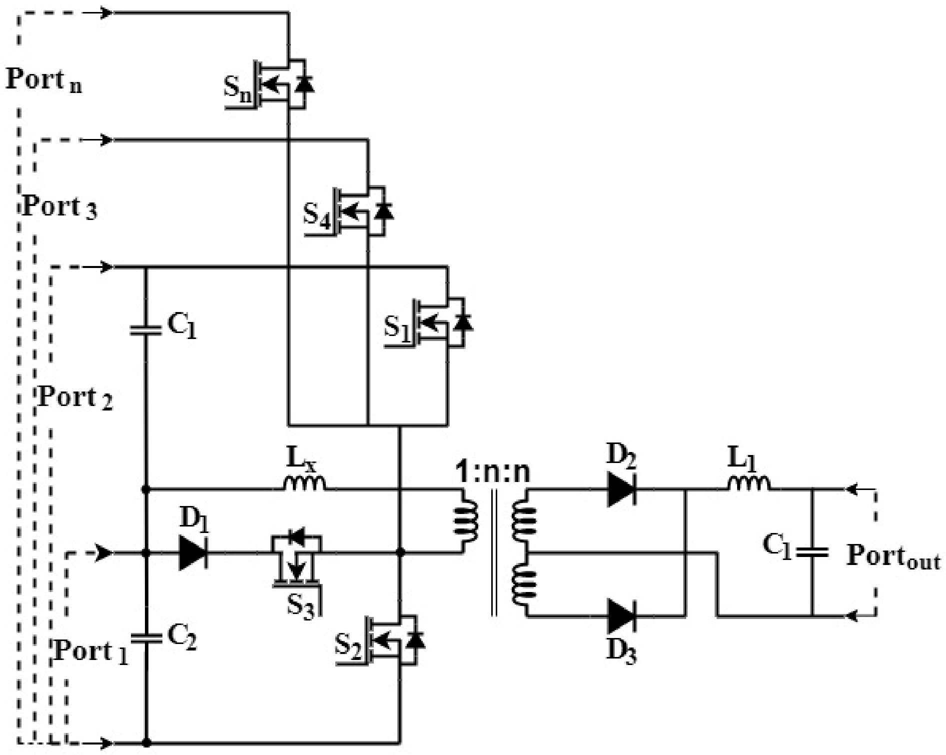


**Figure 2.7** Multi-input partially isolated converter [17][18]

A multiport converter is illustrated in Figure 2.7 combining numerous power sources on the input port by utilizing a switch for each source. A transformer is used to galvanically insulate the output port. The transformer’s secondary windings can be multiplied to provide new isolated ports. The multi-input converters covered in the section on non-isolated multiport converter topologies are comparable to this converter. As a result, this topology suffers from the same limitations as non-isolated topologies since the input ports cannot transfer power at the same time. Partially isolated topologies frequently employ multiport converter architectures, which are a development of conventional converter topologies.

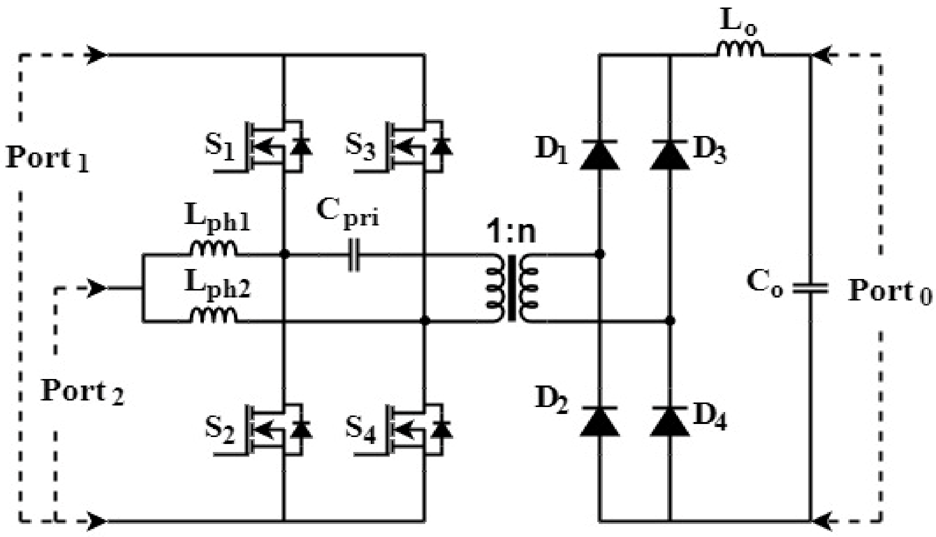


**Figure 2.8** Symmetric Boost Integrated Phase Shift Converter [19]

A partly isolated 3-port DC-DC converter topology is seen in Figure 2.8. In the related topology, ports 1 and 2 is able to transfer power in both directions, however port 0 can only do so in one way. In complementary mode, switch $S_1$ drives switch $S_2$ and switch $S_3$ drives switch $S_4$. The power at ports 1 and 2 is successfully delivered to port 0 when the four switches are controlled using the traditional phase shift control approach. Additionally, the duty cycle values of switches $S_1$ and $S_2$ may be used to govern the flow of power between port 1 and port 2. The design in Figure 2.8 offers a wide output voltage range thanks to its voltage gain. Additionally, it makes it possible to connect low voltage energy sources via port 2. Finally, it may simultaneously deliver power flow from ports 1 and 2 to port 3. The disadvantage of the proposed converter is that the power supply connected to Port 1 has a limited voltage range depending on the voltage value of the power supply connected to Port 2.

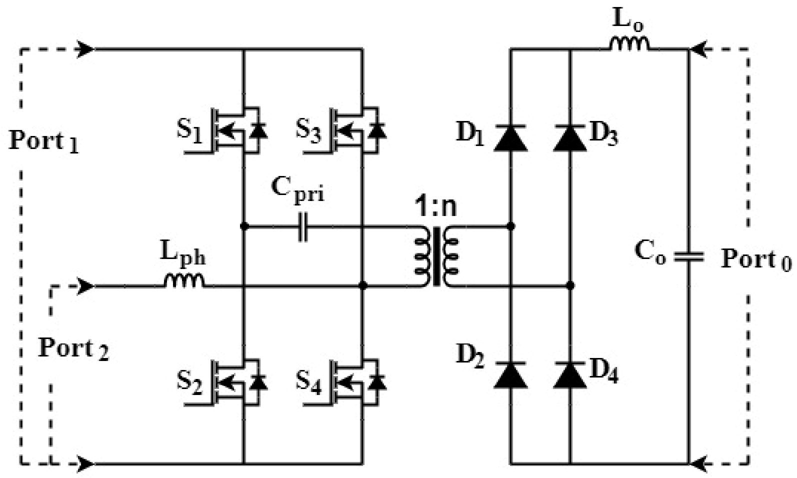


**Figure 2.9** Asymmetric Boost Integrated Phase Shift Converter [20]

Figure 2.8 shows another three-port partially isolated converter topology developed by removing the $L_{ph1}$ coil from the three-port partially isolated topology described in Figure 2.9. The benefit of this topology is that the rectifier diode voltage is less than that of the Symmetric Boost Integrated Phase Shift Converter, offering a wider zero voltage switching (ZVS) range. The disadvantages of this topology are that Port 2 operates at higher voltage levels; it is also less efficient than the symmetric boost integrated phase shift converter.

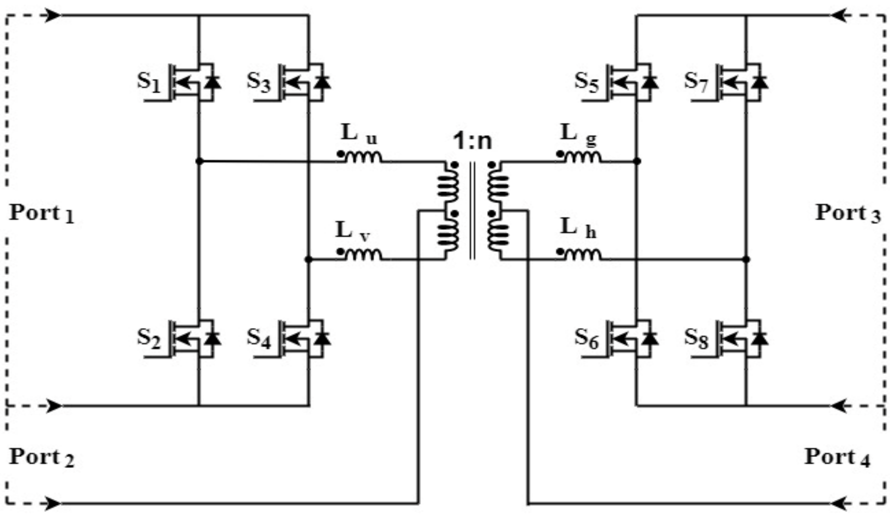


**Figure 2.10** Multiport Converter with Magnetic Coupling Inductor [21]

Figure 2.10 depicts a partially isolated four-port converter generated from interleaved multiphase and bidirectional isolated DC-DC converters. The converter is also consisting of a transformer and two connected inductors. The transmitted power is affected by the phase shift between the two active bridges, switch duty ratio, inductor self-inductance, and coupling coefficient.

The benefits of this topology are that the converter is small and can function independently as a complete bridge DC-DC converter or a multiphase converter. The voltage of port 1 is considered to be equal to the voltage of port 3 on the primary side, and the coupling coefficient of the primary coupled inductors is assumed to be the same as the following when evaluating the system. The efficiency ranges from 90% to 94%, while the switch usage factor is low.

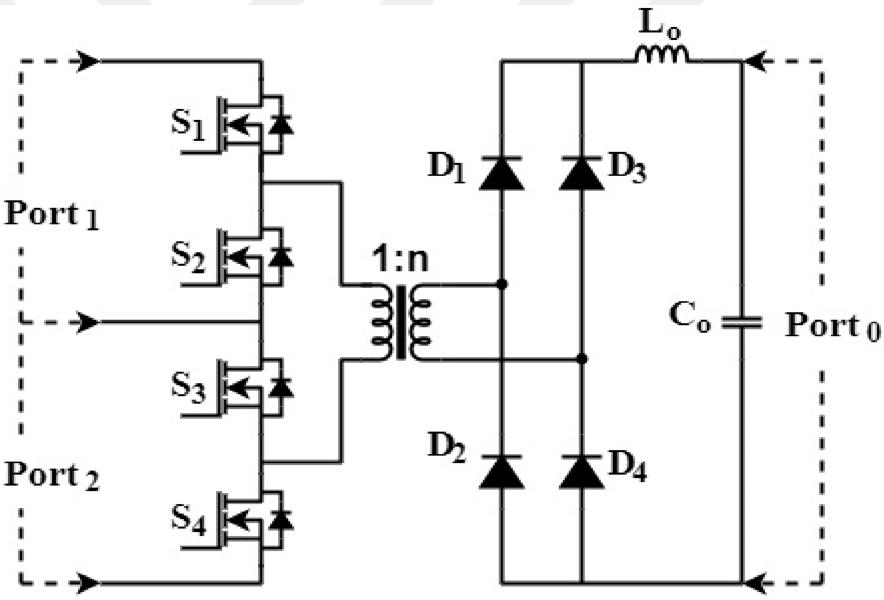


**Figure 2. 11** Full Bridge Three Port Converter [22]

The article [22] describes a three-port partly isolated converter, as seen in Figure 2.11. While port 1 is used to connect the PV array, port 2 is used to connect the battery, and Port 0 is used to connect the load. Power flow from the PV to the load, then to the battery, and finally to the load. For soft switching, a magnetizing inductance transformer is utilized. There are three different operating modes: single input, single output, dual input, and dual output. Each mode's magnetizing current has a distinct value and direction.

Ports 1 and 2 are employed as energy source ports and can send power in two way, whereas Port 0 serves as a load port. Power can be sent to port 0 simultaneously from either one or both of the topology's ports 1, 2. On the primary side, every switching component has ZVS capability. The secondary side of the transformer's complete bridge rectifier structure can be changed into an active rectifier structure. While the system's efficiency ranges between 88% and 92%, it falls as a result of rising current levels and falling voltages at Ports 1 and 2. The diode rectifier on the secondary side of the transformer causes losses to rise.

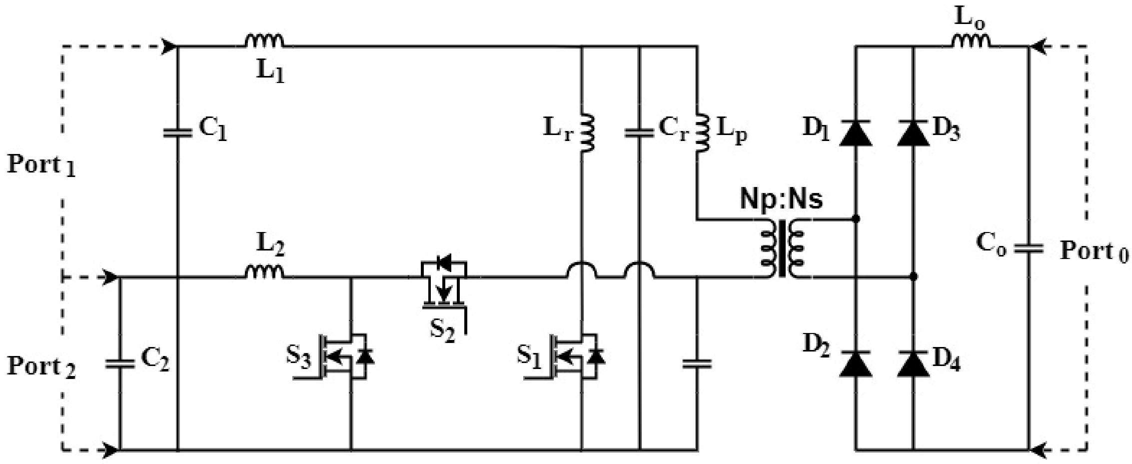


**Figure 2. 12** Isolated Three Port LCL Resonant Bi-Directional DC-DC Converter [23]

In the article of [23], a three-port converter that is only partially isolated, as seen in Figure 2.12 has been proposed. The PV array and batteries are connected to two low voltage ports, while the load is connected to one high voltage port.

Although the topology has the benefit of soft switching in the S1 switch, it also has some disadvantages. The drawbacks are: High switching stress, greater switch $S_1$ usage than switches $S_2$ and $S_3$, hard switching on switches $S_2$ and $S_3$, various control loops interacting, efficiency varying from 86% at low loads to 94.5% at 70W, falling to 93% at full load.

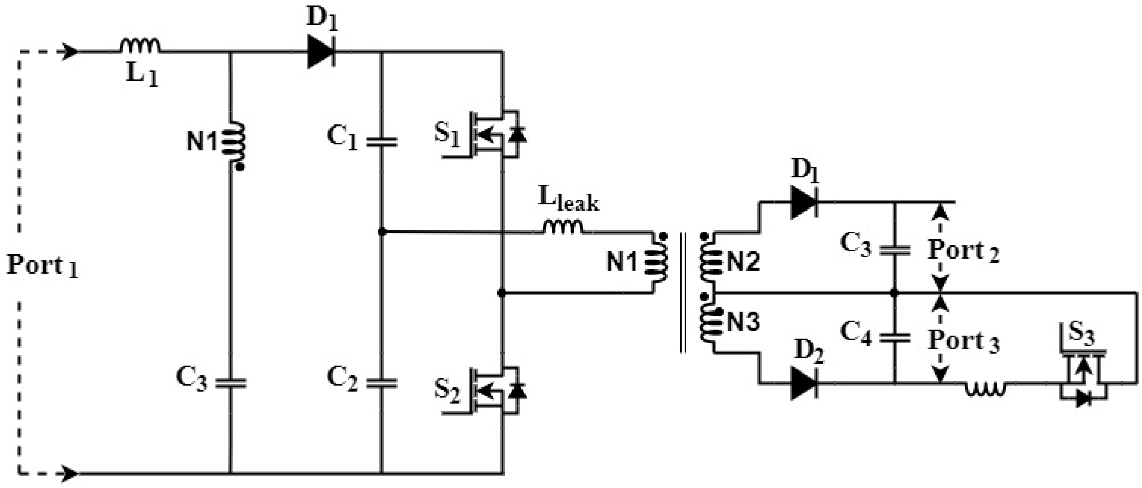


**Figure 2. 13** PV Isolated Three Port Converter [24]

PV, ESU, and the load port are each linked to a different port. This system has three separate operation modes. In the first scenario, as the ESU in port-2 is being charged, port-1 simultaneously sends power to ports 2 and 3. In the second scenario, electricity is transferred from ports 1 and 2 to port 3's load port. The ESU is now releasing. In the third scenario, port 1's PV fails to provide any electricity. The load port is therefore controlled by the ESU at port 2.

### 2.1.3 Fully Isolated Multiport DC-DC Converter

This chapter discusses fully isolated multiport converter topologies where all ports are galvanically isolated.

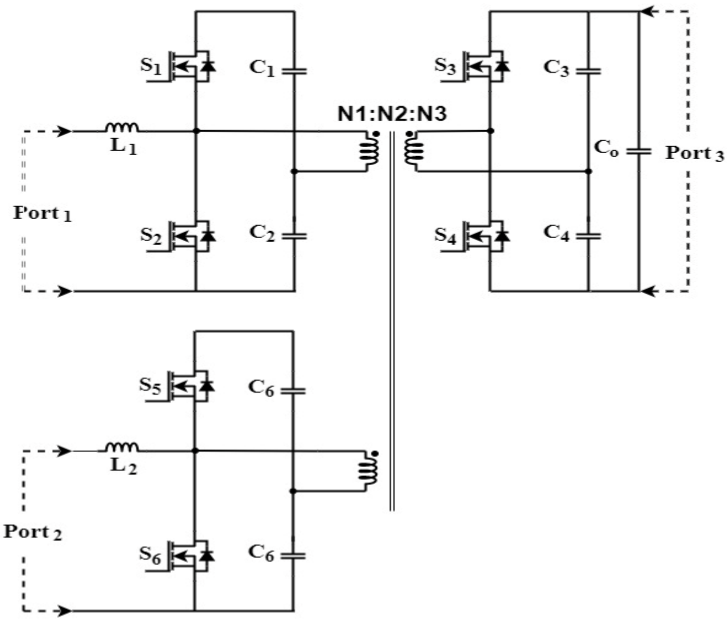


**Figure 2.14** Isolated Three Port Half Bridge DC-DC Converter[25], [26]

The DC-DC converter architecture in Figure 2.14 has three ports: two source ports and one load port. Phase shift and duty cycle control methods are used in the topology. By allowing the ports to function in step-down or step-up mode, the duty cycle control approach enables the ports to work in charge/discharge mode. The phase shift control method determines the direction of power flow between the ports.

All ports of the topology are able to transmit power in both directions, and this topology uses less switching components than complete bridge converters. It also uses soft switching without the requirement of auxiliary components.

The disadvantage of this particular topology is its suitability for low-power applications. The high current flowing through the capacitors equipped in the half-bridge converters adversely affects these capacitors ($C_1$,$C_2$,...,$C_6$). Capacitor values rise in applications requiring high power.

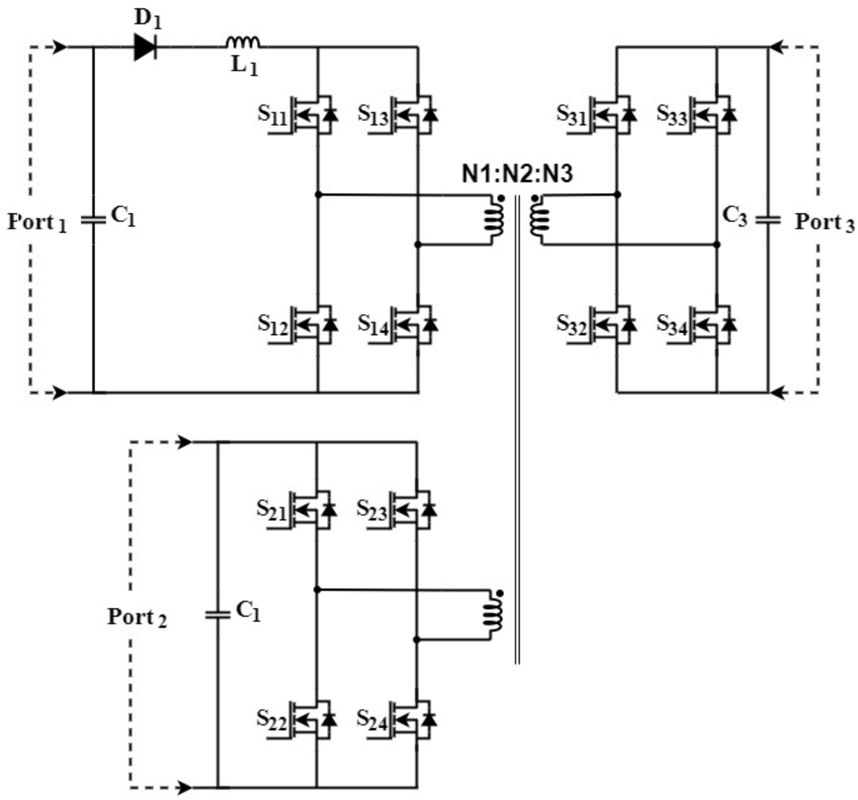


**Figure 2.15** Isolated Three Port Bi-Directional DC-DC Converter [27]

A three-port converter topology in [27] featuring two energy sources and a load port is shown in Figure 2.15. Furthermore, bidirectional power transfer to the ports is possible. As the RESs are not suitable for bidirectional power transfer, the diode $D_1$ is employed to protect them from reverse current, while $L_f$ is used as a filter coil to reduce current fluctuations. By altering the phase shifts between the h-bridges of ports in the architecture, power transmission may be accomplished. The advantages of this topology are that: It reduces the hybrid system's number of switches, it provides high security due to isolation, the control loops operate almost independently of each other. However, the disadvantages of the topology are: Fast changes in phase shift are not taken into account by the controller, all switching elements are driven by hard switching, system efficiency varies between 78% and 91%.

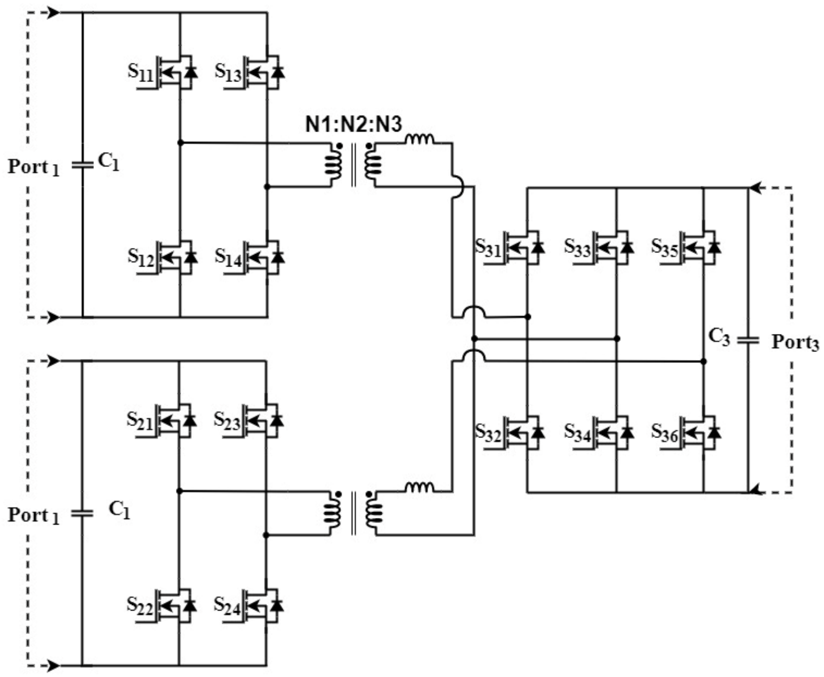


**Figure 2.16** Dual Transformer-Based Asymmetrical Triple Port Active Bridge Converter [28]

Asymmetric three-port active bridge converter topology [28], reproduced from the Dual Active Bridge (DAB) topology, is seen in Figure 2.16. Two full bridge converters, two HFTs, and one three-legged converter comprise the proposed topology. Two distinct operating modes of two-port and three-ports are available for the specified topology. In the three-port mode, the power supply is connected to the port-1 and port-2 terminals of the converter, while the load is connected to the port-3 terminal. Two ports are utilized for power transfer activities in the two-port mode, and one port is completely disconnected from the rest of the system. Power is transmitted from the source ports to the load ports in this mode of operation.

The advantages of this topology are soft switching capability, bidirectional power flow, and simultaneous operation for the ports. However, it has such disadvantages as; there are more switching elements compared to the three-port DAB topology, as well as the use of two different HFTs, which increases the cost.

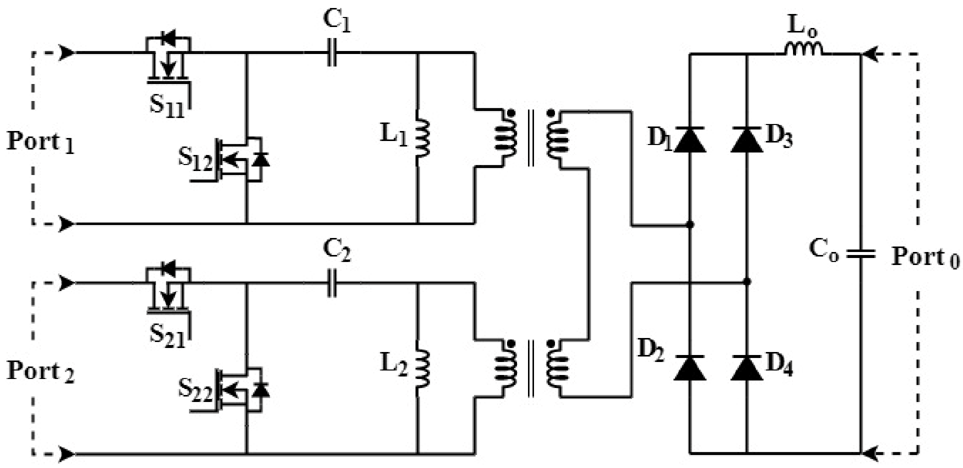


**Figure 2.17** Multiport CLL- Resonant Converter [29]

Figure 2.17 shows a multiport CLL-Resonant converter including two source ports and one load port. The phase difference between port-1 and port-2 provides voltage and power regulation of the load port [29]. The suggested topology excels with the benefits of flexible power flow capability. While ports 1 and 2 can do bidirectional power flow, port 0 can only perform unidirectional power flow. In addition, it has fewer switching elements compared to the isolated three port bidirectional DC-DC Converter described in Figure 2.5. The sources at port-1 and port-2 can simultaneously transfer power to port-0. The switching elements are driven by soft switching method. The disadvantage of the proposed topology is that the addition of new ports requires new transformer connections and the stresses of the switching elements in port-1 and port-2 are high.

Three main types of topologies, such as non-isolated, isolated, and fully isolated DC-DC converters, can be employed in various applications. Additionally, it is noted that multiport converters include various sources (such as PVs, batteries, supercapacitors, wind turbines, the grid, etc.) and load types. In summary, different sources and loads with varying voltage levels and characteristics are being combined and operated synchronously. Therefore, in order for sources with different characteristics to transmit power simultaneously at some point (DC-Link or transformer input voltage, etc.), they need to be regulated and synchronized. Conventional topologies have been insufficient in regulating RES with low output voltage levels. For this purpose, new generation high-gain converter circuits (such as z-source, quasi-z-source, switch-capacitor) have been improved and are being further developed.

### 2.1.4 Z-Source Converter

The Z-Source Converter[30], [31] was first introduced as an alternative to conventional voltage-source and current-source converters. It was developed to address limitations such as restricted voltage gain, short-circuit protection, and power quality issues associated with traditional converters.

The Z-source converter is so named because it uses a unique impedance network, known as a "Z-source" network, to provide a high degree of flexibility and control over the power flow. The Z-source network consists of two passive components, namely a capacitor and an inductor, that are connected in a unique configuration to form a "shunt" or "shoot-through" circuit.

One of the main advantages of the Z-source converter is its ability to handle a wide range of input voltage variations without the need for additional components such as voltage regulators. This is achieved by controlling the shoot-through time of the Z-source network, which allows the converter to regulate the output voltage or current as required. Additionally, the Z-source converter has a higher voltage gain and lower current stress on the switches compared to traditional converters, which can result in higher efficiency and reliability. Wherever high performance, flexibility, and efficiency are required, such as in renewable energy systems, motor drives, and power supply, the Z-source converter is frequently utilized.

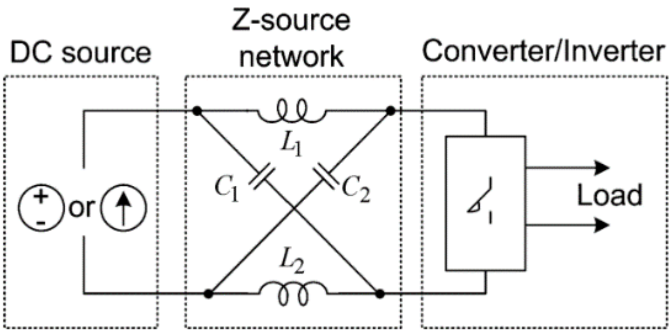


**Figure 2.18** Z-Source Converter

Especially in multiport converters, z-source converters are crucial for combining source ports with various voltage levels since they have high gain, can function as both step-up and step-down converters, and don't require additional switching components.

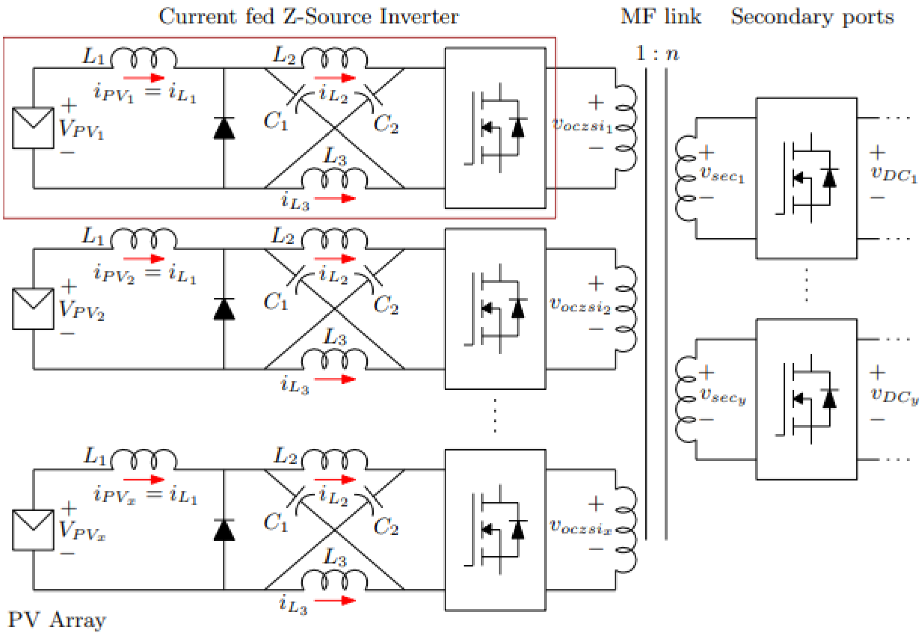


**Figure 2.19** Current-Fed Z-Source Multiport Isolated Converter[32]

A fully isolated multiport DC-DC converter architecture with a built-in Z-Source structure is shown in Figure 2.19. In this architecture, the transformer's main and secondary ports are expanded to produce a multiport converter. The topology's principal ports employ PVs as sources. A Z-Source Inverter is also present in each port. To give high gain, Z-Source converters must be used in shoot-through mode. All switches are in the conduction state during the shoot-through condition, which induces voltage on the z-source circuit. The conduction state takes over when the shoot-through state is finished. The main voltage of the transformer will be equal to the sum of the PV voltage and the z-source voltage in the conduction condition.

The proposed topology has some advantages as; all ports are galvanically isolated, low voltage PVs can be upgraded with a high gain z-source circuit; the source ports can transfer power simultaneously at different power levels. The disadvantages of this topology are that MPPT and Shoot-Though control algorithms are intertwined, and the control algorithm is complex. In addition, the MPPT algorithm limits the duty cycle value.

A Quasi Z-source converter, also known as a Quasi-Z-source inverter (qZSI), is a type of power electronics converter that combines the features of both Z-source converters and traditional voltage-source converters. It was introduced as an extension of the Z-source converter concept. Similar to the Z-source converter, the Quasi Z-source converter utilizes an impedance network to provide unique power flow control capabilities. Quasi z-source converter topology is different from conventional z-source converter topology.

Quasi z-source topology is created with one capacitor and two coils. With the impedance network created with these passive elements, it achieves high gain and increases the energy sources with low voltage values to higher voltage levels. In addition, the passive elements used provide protection of the switching elements during shoot-through.

One of the most important advantages of the quasi z-source topology is that it provides high gain and achieves an output voltage higher than the input voltage. With this feature, it has been frequently used in the developing electric vehicle industry and renewable energy systems where power sources with different voltage values are used.

The Quasi Z-source converter offers improved power quality and increased efficiency compared to traditional voltage-source converters. It can provide a sinusoidal output voltage with reduced harmonic distortion, and it offers bidirectional power flow capability. Due to its unique characteristics, the Quasi Z-source converter has found applications in various fields, including renewable energy systems, motor drives, uninterruptible power supplies (UPS), and electric vehicle charging systems.

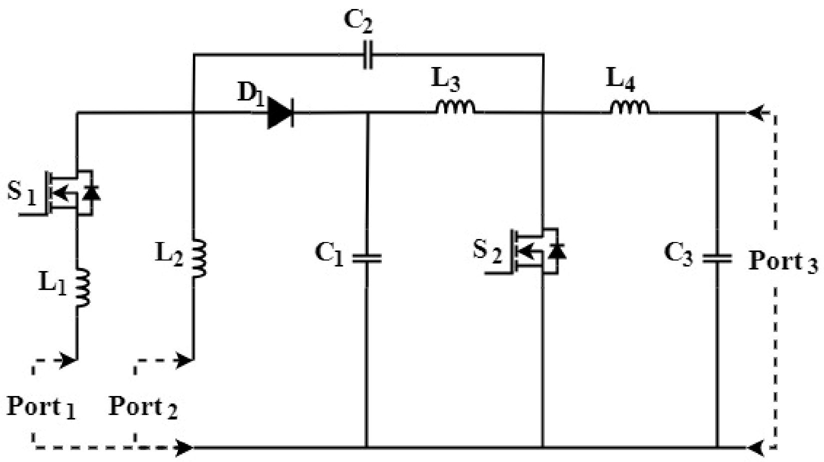


**Figure 2.20** Dual input Single Output Quasi-Z Resonant Multiport Converter[33]

The topology in [33] suggests a multiport next-generation EV battery charger in Figure 2.20. The topology is composed of two source ports, the grid port, and the renewable energy port as well as one load port the energy storage port . Three alternative operating modes are included in the suggested structure.

The topology uses fewer switching elements employed than in the other non-isolated multiport converters under study. Low voltage stress is placed on the switching components. Power can be transferred from the source ports to the load port simultaneously and separately. The Quasi-Z Source resonant circuit allows for high voltage gain. The voltage levels of the source ports must have the same magnitude, which can be notated as a drawback of this topology. An additional converter is needed for MPPT if a RES is connected to the source ports. There is no CC, or CV charging method if an ESU is attached to the load port. Only the power flow is controlled by the topology's control mechanism.

### 2.1.5 Switch Capacitor Converter

A switched capacitor DC-DC converter consists of a capacitor and switching elements. The switched capacitor DC-DC converter topology, which is frequently used in low power applications, converts the power with a certain voltage level to a specified voltage level and transfers the power to the output.

The basic principle of the switched capacitor converter is to charge and discharge the capacitors through the switching element to achieve the desired voltage gain. A switched capacitor converter converts the input voltage to the output voltage as follows. First, the switching element is turned off and charges the capacitor up to the input voltage value. The switching element is switched to conduction according to the control circuits and connects the capacitors to each other. The signals to the switching components are then relocated, and the stored energy is transmitted to the output in conjunction with the input voltage. Finally, the capacitor is connected to the switching element's output port to guarantee that the output voltage remains constant.

However, switched capacitor converters have several drawbacks. When compared to other DC-DC Converter topologies, they are often utilized at low power levels and have a low efficiency ratio. They are more susceptible to noise and require more filtering to enhance voltage quality.

Overall, switch capacitor converters provide a flexible and compact voltage conversion alternative in low-power electronic systems, particularly where size and cost are critical factors.

### 2.1.6 Resonant Converter

Resonant converters aim to increase system efficiency compared to conventional DC-DC converters by reducing switching losses with the help of resonant tanks created with the help of passive elements called capacitors and coils. Resonant converters are widely used in switching power supplies, electric vehicle subsystems and microgrid applications to increase efficiency. Resonant converters reduce switching losses by switching at the resonant frequency within the system and switching on and off at points where the voltage and current values of the switching elements are close to zero.

Resonant converters can be classified into different topologies, such as the series resonant converter [34]–[36], parallel resonant converter [37], and the LLC [38]–[40] resonant converter. Each topology has its own characteristics and suitability for specific applications.

Overall, resonant converters are an important class of power electronic converters that offer advantages in terms of efficiency, size, and weight compared to conventional converters. They have found wide application in various industries, contributing to the development of more efficient and compact power systems.

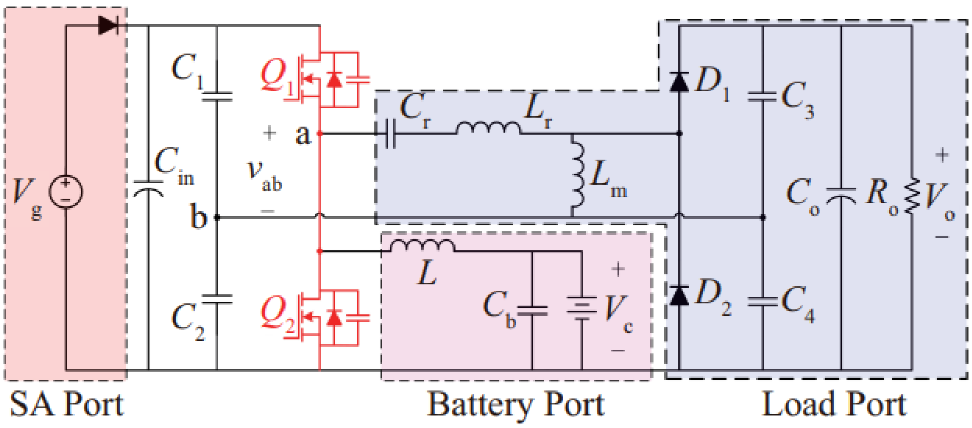


**Figure 2.21** Non-Isolated LLC Multiport Converter

A non-isolated multiport LLC converter architecture [41] is suggested in Figure 2.21. The half bridge topology without a HFT is used to construct the topology. It is suggested to use the low side switching component of the half bridge architecture as a common port for a two input, one output multiport converter. A PV is endowed to one of the input ports, while a battery, an ESU, is placed into the other input port. Three alternative operating modes are included in the suggested structure. If the electricity supplied by the PV is insufficient for the load port, the battery can drain and transmit power to the load port in the event that the PV fails to generate power due to environmental factors. Finally, if the PV produces more energy than the load port requires, the extra energy is sent to the battery to charge it.

The following are some of the topology's benefits: By minimizing the number of switching components, a cost-effective topology is suggested. Furthermore, power can be sent in both directions through the battery port. Resonant topology makes it feasible to implement soft switching.

The following are the topology's drawbacks: The topology, which derives from the half-bridge architecture, puts a lot of strain on capacitors $C_1$, $C_2$, $C_3$, and $C_4$ when used in high power applications. On the rectification side, passive rectification is utilized.

# 3. POWER CIRCUIT MODELLING

## 3.1. Interleaved Based Isolated Multiport Converter

The literature studies exposes the multiport converters redundant switching components, high control complexity, and high computational load. With the benefits of a decreased element count, cheap cost, and high efficiency, a unique isolated multiport DC-DC converter with interleaved based bidirectional operation is given in this chapter. The suggested topology provides;

1. The integration of a relatively low voltage battery system.
2. It has several input connections for various power production and ESU and two independently controllable output ports.
3. A minimal number of switching components allows for a low-cost power electronics system,
4. It is possible to construct a multi-loop control structure that enables quick switching between control loops to regulate the power transmission between RES and loads.

The suggested multiport converter's operating theory is described in this section, and its control structure is detailed in part 4.1. Section 5.1 concludes with a performance analysis.

The interleaved based isolated multiport DC-DC converter power circuit is seen in Figure 3.1 and consists of a half-bridge rectifier, an HFT, and interleaved step-down and step-up converters. The suggested converter is built to deliver the best power flow possible from the PV to the battery and loads, or from the PV and battery to the loads, while maintaining the load voltages consistently at the appropriate level.

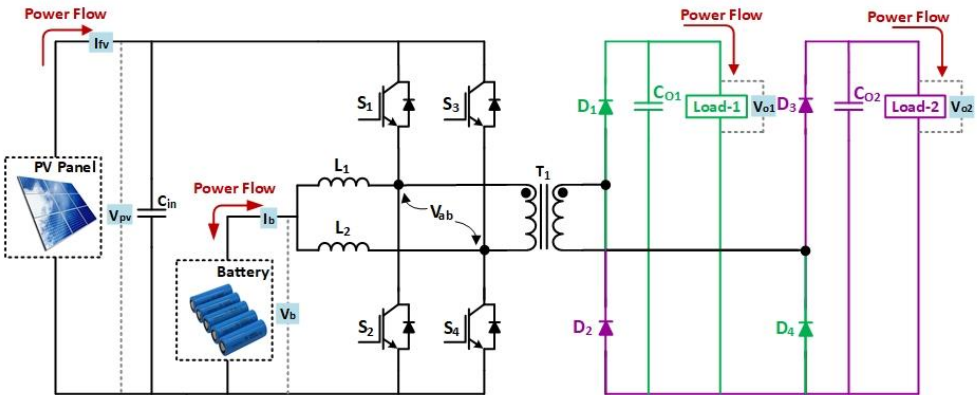


**Figure 3.1.** Interleaved Based Isolated Multiport DC-DC Converter

The incorporation of a battery with a relatively low voltage as well as two-way power transmission between the PV and the battery are both made possible by the interleaved DC-DC converter. This makes sure that under various operating situations, the loads maintain consistent voltage levels. A large voltage gain with a HFT turns ratio is also possible with the converter under consideration. Half bridge rectifier circuits are present on the HFT's secondary side.

Figure 3.2 depicts the interleaved based isolated multiport DC-DC converter's switching waveforms. Various control loops activate the switching components. Switches $S_3$ and $S_4$ are activated by load control loops to provide voltage regulation of loads, whereas switches $S_1$ and $S_2$ are actuated by MPPT, CC, and CV control algorithms. The switching element signals function in a complimentary manner since switches $S_1$ and $S_2$ are on the same arm and are short-circuited if they are both triggered at the same time.

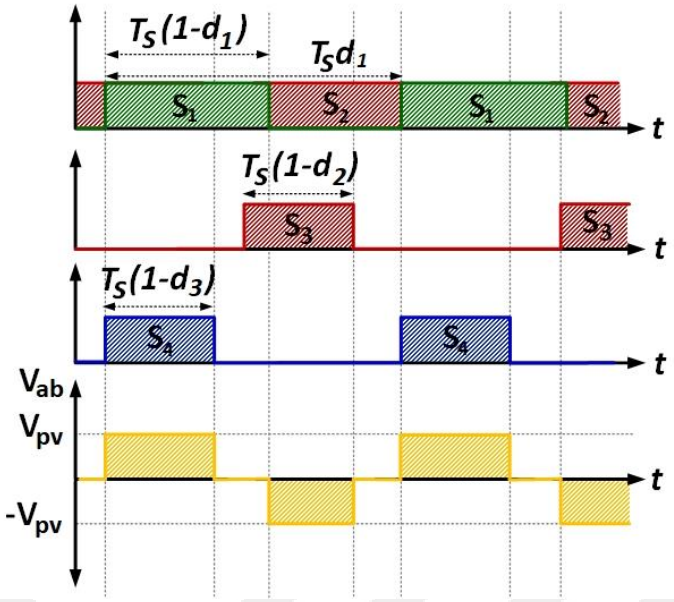


**Figure 3.2.** Interleaved Based Isolated DC-DC Converter Control Method

$T_s$ denotes a transitional era. The MPPT, CC, and CV control loops proportional-integration (PI) compensation outputs influence the duty cycle value known as $d_1$. Switching elements $S_3$ and $S_4$ ($d_2$ and $d_3$) duty cycle values have a maximum value of 50%. This is due to the 180° degree phase discrepancy between when the $S_3$ and $S_4$ switches are actuated. At this point, if the relevant switches have a duty cycle of more than 50%, both the upper and lower switches will open simultaneously, resulting in a short circuit. The load control cycles define the duty cycle values for switches $S_3$ and $S_4$.

The switch capacitive structure has a exceeds voltage gain than the interleaved structure utilized in the interleaved based multiport converter design. The isolated multiport converter with switch capacitors is described in Section 3.2. Supporting the switch capacitor-based multiport converter design with a lower voltage PV result in a novel topology.

### 3.2. Switch Capacitor Based Isolated Multiport Converter

Researchers are frequently interested in lowering the quantity of switching components and control complexity in multiport DC-DC converter research. In addition, to get the most power out of RESs, unidirectional DC-DC converters with high gain ratios are frequently utilized. In terms of effectiveness and application, resonant, z-source, and switch capacitor converters are the best high gain converters. The switched-capacitor boost converter and the half-bridge converter stand out at this point among the pertinent DC-DC Converter topologies thanks to the benefits outlined above.

To combine the RES and the battery with an isolated DC-DC converter via a common bus connection, it is introduced a novel multiport DC-DC converter outfitted with a switched capacitor DC-DC converter in this section. The power flow of the battery is controlled by the existing converters taking into account the operating circumstances since adding another DC-DC converter would greatly increase the size and expense of the whole system. A multi-loop control structure that operates adaptively and enables instantaneous switching between loops is a feature of the switched-capacitor multiport DC-DC converter.

The switched-capacitor DC-DC converter, controlled full-bridge rectifier, half-bridge converter, and HFT constitute the multiport DC-DC converter seen in Figure 3.3. The converter interface, that is being suggested, intends to combine the battery, PV, and load while managing the best possible power flow between the input and output ports.

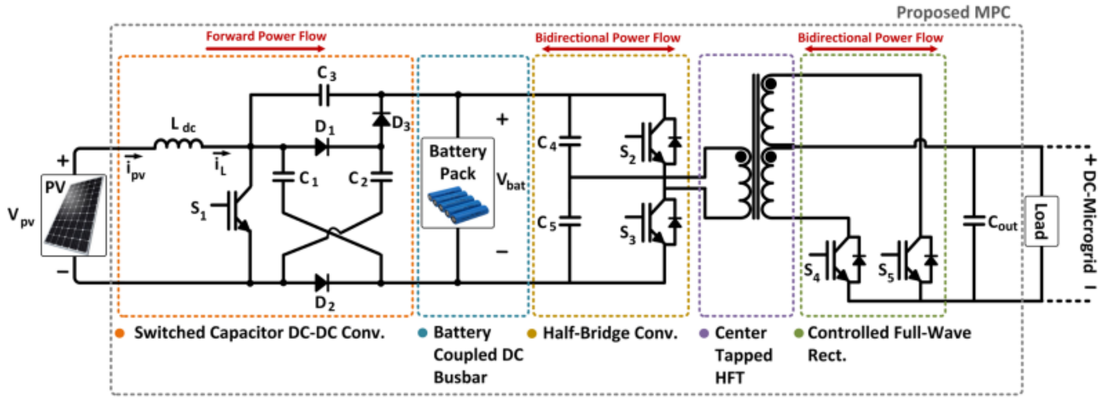


**Figure 3.3.** Switch-Capacitor Multiport DC-DC Converter

With great efficiency, electricity is transferred from the PV to the battery or load via a switched-capacitor DC-DC converter. In addition, the associated DC-DC converter's high voltage conversion ratio capabilities enable the connection of low voltage PV into a relatively high voltage battery. By transmitting power from input ports to the output port and from the output port to the battery, half-bridge converters enable bidirectional power flow. When electricity is flowing forward, the half-bridge converter acts as an inverter; when it is flowing backward, it acts as an uncontrolled full-wave rectifier. HFT with low turns ratios enable the galvanic isolation between the input and output ports. Contrary to a half-bridge converter, the controlled full wave rectifier on the secondary side functions as an inverter during reverse power flow and as an uncontrolled full wave rectifier during forward power flow. The switch capacitor based MPC integrates three different converters;

1. Switched-capacitor DC-DC converter,
2. Half-bridge converter
3. Controlled full-wave rectifier via battery coupled common DC-Link and HFT.

The switched-capacitor DC-DC converter performs the MPPT, CC, and CV charging operations on the primary side, while the battery serves as a common DC-Link. The half-bridge converter DC-Link is fed by PV and buffered by batteries. Thus, the load receives constant power transfer. The PV-battery voltage relationship is calculated using the $S_1$ duty cycle. It is spoken in the following way:

$$Gain = \frac{V_{bat}}{V_{pv}} = \frac{2}{1-D} \tag{1}$$

where the battery voltage ($V_{bat}$) and the PV output voltage ($V_{pv}$), respectively, are shown. $D$ is the duty cycle of switch $S_1$ and ranges from 0 to 1 depending on the system's operational circumstances. In addition, controlled complete bridge rectification is accomplished using switches $S_4$ and $S_5$. In section 4.2, the gate signals of the switching components and control modelling will be discussed.

Typically, several power stages are integrated together to create multi-port converters, as is the case with the switch capacitor design described in section 3.2. However, combining several power stages necessitates the use of more switching components. Two separate power stages are integrated by sharing the same switching element in the quazi z-source multiport converter design described in section 3.3.

### 3.3. Quasi Z-Source Multiport Converter

For a PV supplied EV with a supercapacitor and battery, this research suggests a unique isolated multiport bidirectional DC-DC converter architecture combined with a quasi-Z-source converter. Additionally, a management strategy of power flow and associated control plan are recommended. The quasi-Z-source MPC (qZ_iMPC) converter is comprised of a controlled full-wave rectifier, an H-bridge converter, a secondary center-tapped HFT, and a quasi-Z-source converter. Through the quasi-Z-source converter, the quasi-Z-source enables low input battery/supercapacitor voltage and lower duty cycle to obtain a large voltage gain. The suggested converter less active switches are needed when incorporating four ports than the converters described in the literature and supports bidirectional power flow. Numerous case studies are used to demonstrate how well the suggested approach performs.

This study proposes a new four-port converter architecture. Figure 3.4 shows the suggested qZ_iMPC, which comprises of a quasi-Z-source converter, a controlled full-wave rectifier, an H-bridge converter, and a secondary center-tapped HFT. To supply CV to the EV's motor drive, a PV system feeds the electric motor (EM), which is thought to be a load, and an ESU buffers it. To prevent harm to the battery pack during transients, the ESU is made up of a supercapacitor pack to reduce the effect of the inrush current and a battery pack to provide the EM in steady-state circumstances. High-voltage gain is made achievable by the qZ_iMPC by employing a quasi-Z-source converter on the ESU side. As a result of the low supercapacitor pack voltage and reduced duty cycle capability, the number of series supercapacitors also reduces. There is a regulated full wave rectifier on the HFT's secondary side. The switching components are rectified by free-wheeling diodes to assure power flow to the EM side, whilst active switches are actuated for the power flow toward the ESU.

The phase-shifted full-bridge DC-DC converter and the quasi-Z-source DC-DC converter share the $S_2$ switch, as seen in Figure 3.4. The supercapacitor and battery pack can be charged either toward PV or through EM when regenerative braking is in place when PV production capacity exceeds EM demand. The ESU meets the EM's energy needs if there is insufficient irradiation over the PV. Real-time monitoring of the fluctuating EM requirements and PV power output is done by a power flow management system.

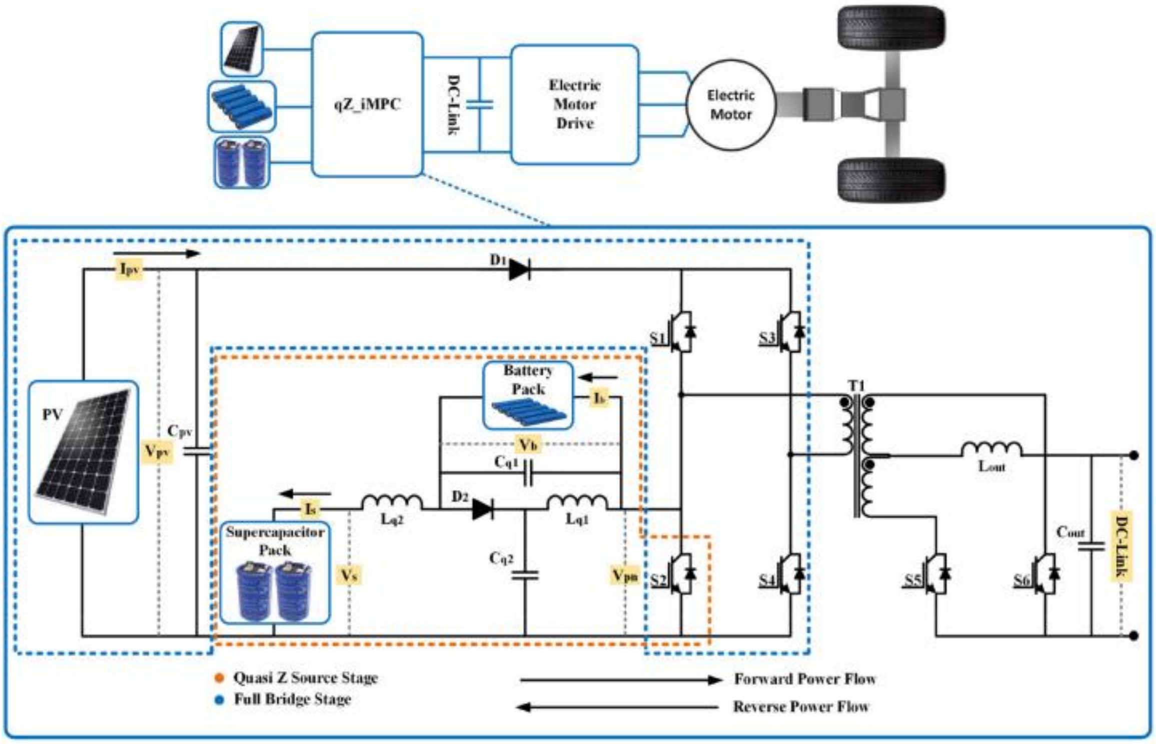


**Figure 3.4.** Quasi-Z-Source Integrated Isolated Multiport DC-DC Converter

As determined by the PV and EM instantaneous power values, the qZ_iMPC topology has three different operating modes. When energy is transmitted from PV, the converter works in mode 1. to EM and ESU; mode 2 shortly after the power is transferred from PV and ESU to EM; and mode 3 when the power generated on the EM side is transferred to the ESU. In Figures 3.5-3.8, a thorough representation of the phase of implementation and current flows throughout the modes is provided. The switching sequence diagram for mode 1 operation of the converter is shown in Figure 3.5a, where Ts represent the switching cycle for $S_1$–$S_6$. The converter is in mode 1 and has four operating phases during one switching cycle, as seen in Figure 3.5a. The duty cycle value of the quasi-Z source converter topology is 0-0.5 and determines the power flow direction and the gain of the system. $S_5$ and $S_6$ switches are in the off state, but their freewheeling diodes function as a full-wave rectifier. The current flow in mode 1 is seen in Figure 3.6.

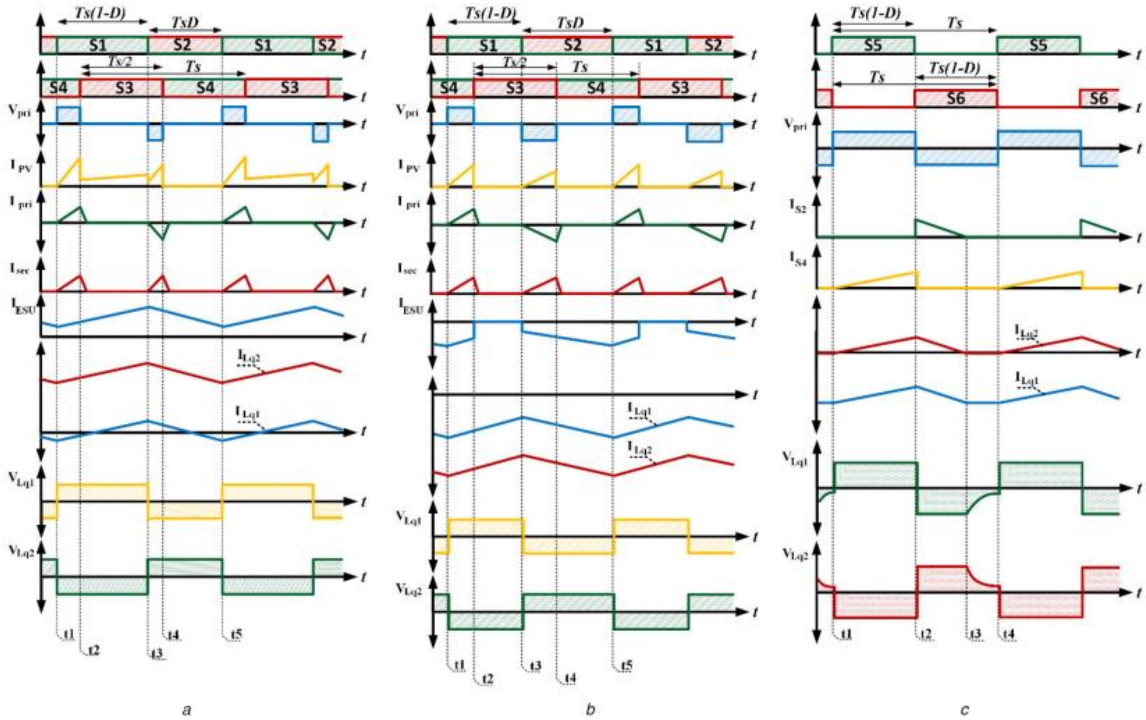

**Figure 3.5** Diagrams of switch sequences (a) Mode 1, (b) Mode 2, (c) Mode 3

Stage 1 [$t_1$-$t_2$]: $S_1$ switch is switched ON at time $t_1$. $I_{Lq1}$ and $I_{Lq2}$ currents steadily rise until the time point $t_2$ as a quasi-Z-source circuit works in a non-shoot through condition. The PV is also used to charge the battery pack and supercapacitor pack. The $S_4$ switch, on the contrary, turns on up to time point $t_2$. In this way, the HFT's main voltage matches the PV voltage. The HFT primary and ESU current are added to determine the PV current. In the meantime, PV power is sent to the EM while the freewheeling diode of the $S_5$ switch is switched ON.

Stage 2 [$t_2$-$t_3$]: The $S_3$ switch is switched ON at time $t_2$. Since the quasi-Z-source circuit is still exist in a non-shoot through condition, $I_{Lq1}$ and $I_{Lq2}$ currents progressively grow until time point $t_3$. The PV is also used to charge the battery pack and supercapacitor pack. However, because $S_1$ and $S_3$ switches are ON at this point, power transmission from PV to EM is complete. The HFT's primary and secondary currents both reach zero, and the PV current reaches parity with the ESU current. In the meantime, the $S_5$ switch's freewheeling diode is turned ON, transferring the energy from the HFT to the EM. The output capacitor ($C_{out}$) is supplied EM and the freewheeling diode of the $S_6$ switch is turned ON when the primary and secondary currents of the HFT are zero.

Stage 3 [$t_3$-$t_4$]: The $S_2$ switch is switched ON at time $t_3$. $I_{Lq1}$ and $I_{Lq2}$ currents steadily diminish until the time point $t_4$ because a quasi-Z-source circuit operates in a shoot-through condition and prevents the battery pack and supercapacitor pack from being charged through the PV. On the other side, at time $t_3$, the $S_2$ switch is turned ON.

Stage 4 [$t_4$-$t_5$]: The $S_2$ switch is switched ON on the opposite side at time $t_3$. To prevent the battery pack and supercapacitor pack from being charged by the PV while a quasi z-source circuit operates in a shoot-through scenario, hence $I_{Lq1}$ and $I_{Lq2}$ currents steadily decline up to the point of time $t_4$. Up to time point $t_5$, the ESU current steadily drops. In the meanwhile, the $S_6$ switch's freewheeling diode is turned ON, transferring the power from the HFT to the EM. When the primary and secondary currents of the HFT arrive at zero, the freewheeling diode of switch device S5 turns ON and the power demanded by EM is supplied by Cout.

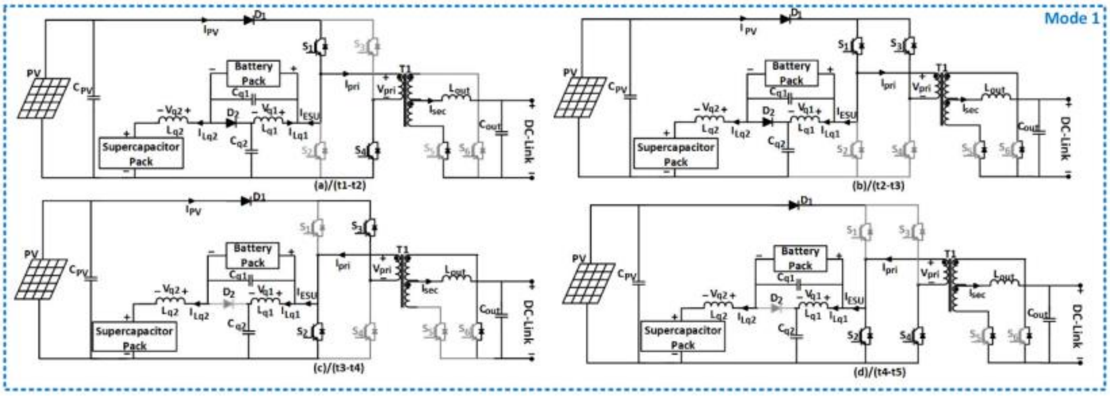

**Figure 3.6** Current flow paths of mode 1 (a) Stage 1 ($t_1$–$t_2$), (b) Stage 2 ($t_2$–$t_3$), (c) Stage 3 ($t_3$–$t_4$), (d) Stage 4 ($t_4$–$t_5$)

The switching pattern scheme for the converter's mode 2 operation is shown in Figure 3.5b. The converter operates through four operating phases in mode 2 over the period of one switching cycle. D might be anything between 0.5 and 1. The diodes of the $S_5$ and $S_6$ switches operate as a full-wave rectifier even when the switches are off. In Figure 3.7, the current flow in mode 2 can be seen.

Stage 1 [$t_1$-$t_2$]: At time $t_1$, the $S_1$ switch is turned ON. The currents in the circuit $I_{Lq1}$ and $I_{Lq2}$ continuously rise until the time point $t_2$ when a quasi-Z-source circuit is working in a non-shoot-through situation. Both the battery and supercapacitor packs have been discharged. However up until time point $t_2$, the $S_4$ switch is turned on. In this way, the PV voltage and the HFT's main voltage are matched. The HFT main current is calculated by adding the PV current and ESU current. Power from the PV and ESU is transferred to the EM in the meantime, and the $S_5$ switch's freewheeling diode is turned ON.

Stage 2 [$t_2$-$t_3$]: The $S_3$ switch is switched ON at time $t_2$. Until the time point $t_3$, the $I_{Lq1}$ and $I_{Lq2}$ currents of quasi-Z-source circuit progressively increase as it continues to run in a non-shoot-through condition. Because $S_1$ and $S_3$ switches are now ON, the power transfer from PV to EM is complete. At time point $t_2$, the primary and secondary currents of the HFT decline to zero, and the currents of the PV and ESU are equal to zero as well. In the meantime, the diode of $S_5$ switch is switched ON, transferring the HFT's energy to the EM. The diode of switch $S_6$ turns ON and the $C_{out}$ supplies power to the EM as the primary and secondary currents of the HFT arrive zero.

Stage 3 [$t_3$-$t_4$]: The $S_2$ switch is switched ON at time $t_3$. The shoot-through condition of a quasi-Z-source circuit causes $I_{Lq1}$ and $I_{Lq2}$ currents to steadily diminish until time point $t_4$. On the other side, at this point the $S_3$ switch is switched ON. The main voltage of the HFT is equivalent to the negative PV voltage in this way. Additionally, the negative PV current and the HFT main current are both equal. However, until time point $t_4$, the ESU current progressively decreases. As this is occurring, PV power is switched over to the EM and the freewheeling diode of the $S_6$ switch is turned ON.

Stage 4 [$t_4$-$t_5$]: The $S_4$ switch is activated at time $t_4$. The shoot-through condition of a quasi-Z-source circuit is remained active, and the currents in the circuit, $I_{Lq1}$ and $I_{Lq2}$, progressively decrease until time point $t_5$. Because the $S_2$ and $S_4$ switches are now turned on, power has been transferred from the PV to the EM is complete. As a result, the PV current is zero at time point $t_5$, and the primary and secondary HFT currents are dropping. Until time point $t_5$, the ESU current steadily drops. Meanwhile, the $S_6$ switch's freewheeling diode is turned on, moving energy from HFT to EM. When the primary and secondary currents of the HFT reach zero, the $C_{out}$ is supplied with EM, which also activates and switches on the $S_5$ switch's freewheeling diode.

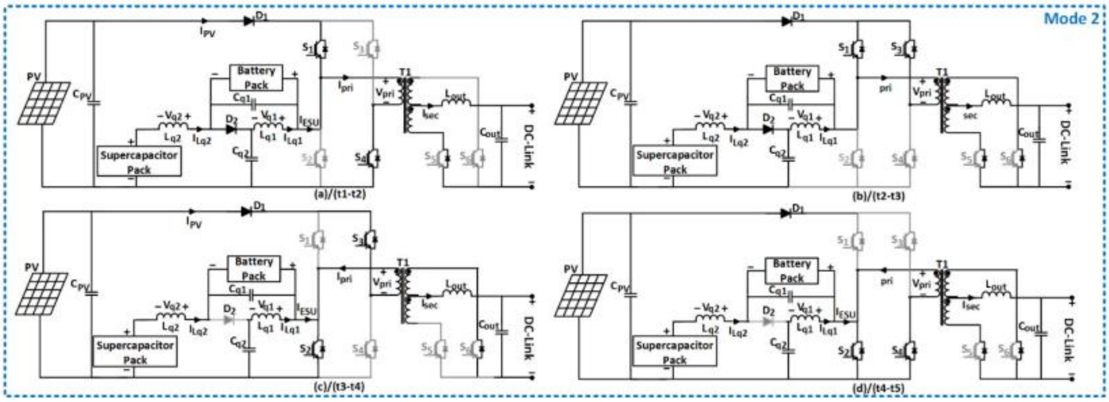


**Figure 3.7.** Current flow paths of mode 2 (a) Stage 1 ($t_1$–$t_2$), (b) Stage 2 ($t_2$–$t_3$), (c) Stage 3 ($t_3$–$t_4$), (d) Stage 4 ($t_4$–$t_5$)

The switching pattern scheme for the converter's mode 3 operation is shown in Figure 3.5c. During a switching cycle, the converter goes through three operational phases. *D* fluctuates from 0 to 1 in the range. Because of the orientation of diode $D_1$, power cannot travel to the PV.  The current flow in mode 3 is seen in Figure 3.8.

Stage 1 [$t_1$-$t_2$]: At time $t_1$, the $S_5$ switch is turned ON. Currently, the HFT main voltage is the same as the DC-link voltage. As a consequence, the $S_2$ switch's freewheeling diode is turned off, while the $S_4$ switch's freewheeling diode is switched on. The quasi-Z-source circuit remains in non-shoot-through mode, and the $I_{Lq1}$ and $I_{Lq2}$ currents slowly grow up to the point of time $t_2$.

Stage 2 [$t_2$-$t_3$]: At time $t_2$, the $S_6$ switch is turned ON. HFT's primary voltage is now equal to its negative DC-Link voltage. As a result, the freewheeling diode on the S2 switch is activated, while the freewheeling diode on the S4 switch is deactivated. Meanwhile, the quasi-Z-source circuit is in a shoot-through state, and the $I_{Lq1}$ and $I_{Lq2}$ currents are dropping progressively until time point $t_3$.

Stage 3 [$t_4$-$t_5$]: Although the $S_2$ switch current hits zero at this time, the HFT’s main voltage is identical to the negative DC-link throughout this period. Additionally, at this period, $I_{Lq1}$ and $I_{Lq2}$ remain stable. As a result, the voltages of $V_{Lq1}$ and $V_{Lq2}$ steadily decrease until time point $t_4$.

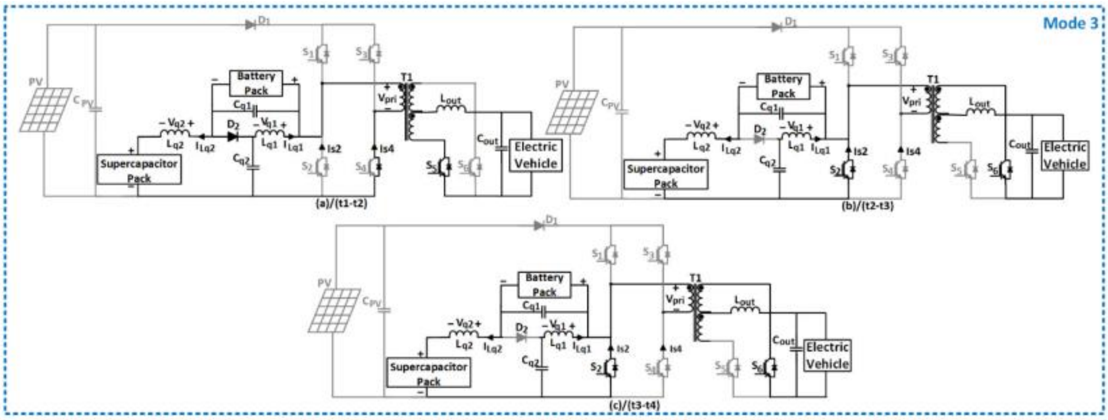


**Figure 3.8.** Current flow paths of mode 3 (a) Stage 1 ($t_1$–$t_2$), (b) Stage 2 ($t_2$–$t_3$), (c) Stage 3 ($t_3$–$t_4$)

The S2 duty cycle (D) is used to compute the relationship there among PV voltage ($V_{PV}$) and battery voltage ($V_{bat}$), taking into consideration the ESU's operating modes. It is stated in the following way:

$$V_{PV} = \frac{V_{bat}}{D} \tag{2}$$

The quasi-Z-source converter's inductor voltages and currents are computed in accordance with (3) and (4) during the time interval between the non-shoot-through and shoot-through states, respectively.

$$V_{Lq2} = V_S - V_{Cq2}, V_{Lq1} = -V_{Cq1}, V_{pn} = V_{Cq2} - V_{Lq1} = V_{Cq1} + V_{Cq2}, V_{D2} = 0 \tag{3}$$

$$V_{Lq2} = V_S + V_{Cq1}, V_{Lq1} = V_{Cq2}, V_{pn} = 0, V_{D2} = (V_{Cq1} + V_{Cq2}) \tag{4}$$

where $V_{PN}$ and $V_S$ stand for, respectively, the quasi-Z-source converter's output and the supercapacitor voltage.

At steady-state, inductors have an average voltage of zero at one switching cycle. As a result, the following is how the capacitor voltages may be determined:

$$V_{Lq1} = \frac{DT_s(V_{Cq2}) + (1-D)T_s(-V_{Cq1})}{T_s} = 0 \tag{5}$$

$$V_{Lq2} = \frac{DT_s(V_{Cq1} + V_s) + (1-D)T_s(V_s - V_{Cq2})}{T_s} \tag{6}$$

$$V_{Cq1} = \frac{D}{1 - 2D} V_S \tag{7}$$

$$V_{Cq2} = \frac{1 - D}{1 - 2D} V_S \tag{8}$$

The following is a definition of the connection between battery voltage and supercapacitor voltage in steady state.

$$V_{pn} = V_{Cq1} + V_{Cq2} = \frac{1}{1 - 2D} V_S \tag{9}$$

Hard switching in multi-port converter topologies results in significant power losses, much like in general-purpose DC-DC converters. In section 3.3, a resonant tank circuit is introduced to the qZ_iMPC topology, and in section 3.4, a soft switching quasi z-source multiport converter architecture is described.

### 3.4. Resonant Tank Integrated Isolated Quasi Z-Source Multiport Converter

Figure 3.9 depicts the suggested isolated resonant tank integrated isolated quasi-Z-source multiport DC-DC converter (qZ_RiMPC) topology. It consists of a controlled full wave rectifier, an H-bridge converter, a resonant tank, a quasi-Z-source converter, and a secondary center-tapped HFT. It includes four ports, three of the input ports for connecting supercapacitor, battery, and PV and fourth port which is the output port. The two input ports which allow bidirectional power flow, ESUs, also known as the battery and supercapacitor ports, supply electricity in both directions to the PV port and the load. The best features of each of two energy storage systems have been combined into the ESUs, a battery and supercapacitor. While the supercapacitor with the highest energy density lowers the inrush currents during transient situations, the battery with the highest power density buffers the load during steady-state conditions. Additionally, the battery and supercapacitor are charged when the PV produces more energy than the load requires, improving system efficiency. While the high gain quasi-Z-source converter enables bidirectional power flow by lowering the rated voltages of the battery and supercapacitor, the H-bridge converter offers power flow from PV to ESUs and load. Additionally, the $S_z$ switch of quasi-Z-source converter enables for the independent adjustment of the currents in each ESUs unit.

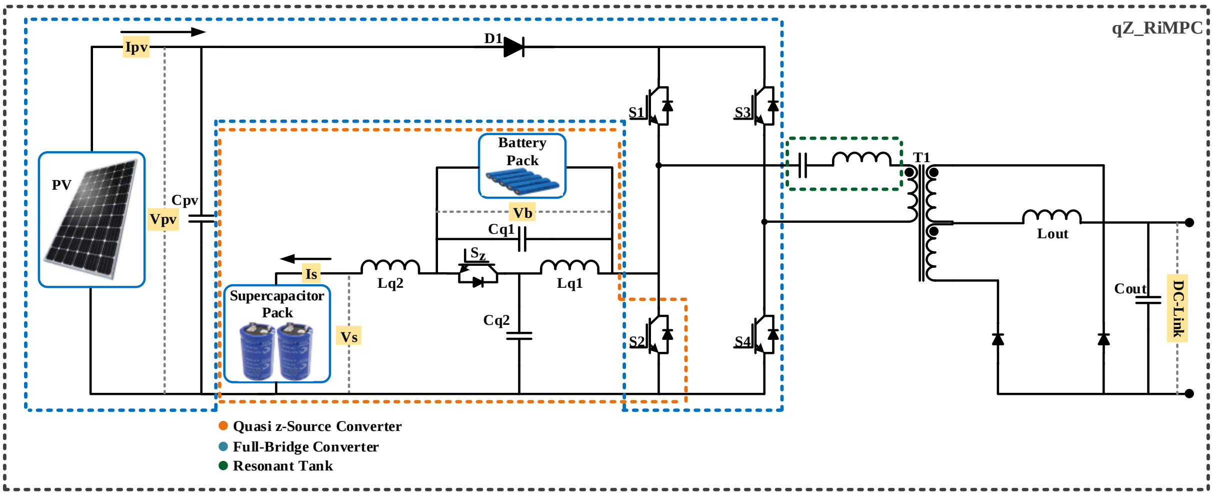


**Figure 3.9.** Resonant Tank Integrated Isolated Quasi Z-Source Multiport Converter

The non-shoot-through and the shoot-through are the two different operating states for the quasi-Z-source converter. Figure 3.10 (a) and (b) respectively depict the corresponding circuits for the shoot-through and non-shoot-through states. Considering that the interval of the shoot-through state is $DT_s$ during a switching cycle $T_s$ and the interval of the non-shoot-through state is $(1-D)T_s$. $D$ stands for the duty cycle of switch $S_2$ since the switch shutting symbolizes the shoot-through condition.

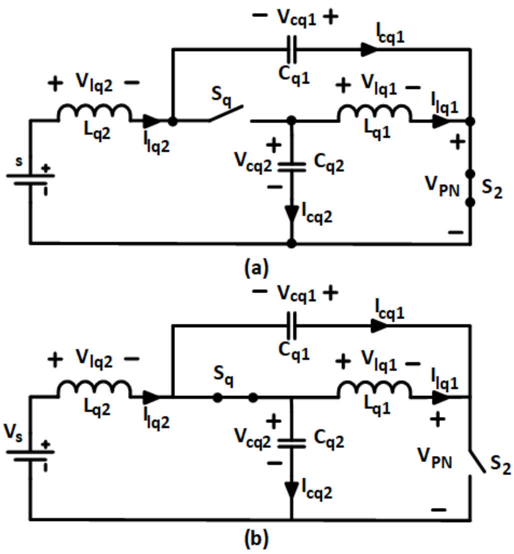


**Figure 3.10.** Equivalent circuits of resonant quasi z-source converter for (a) non-shoot through and (b) shoot through states

From Figure 3.10(a) and 3.10(b), the voltages of the quasi z-source converter may be derived throughout the time period between non-shoot-through and shoot-through states as;

$$V_{Lq2} = V_S - V_{Cq2}, V_{Lq1} = -V_{Cq1}, V_{pn} = V_{Cq2} - V_{Lq1} = V_{Cq1} + V_{Cq2}, V_{D2} = 0 \quad (10)$$

$$V_{Lq2} = V_S + V_{Cq1}, V_{Lq1} = V_{Cq2}, V_{pn} = 0, V_{D2} = V_{Cq1} + V_{Cq2} \quad (11)$$

where $V_{PN}$ and $V_S$ stand for, respectively, the quasi-Z-source converter's output and the supercapacitor voltage.

At steady-state, inductors have an average voltage of zero at one switching cycle. Consequently, the capacitor voltages may be calculated as follows:

$$V_{Lq1} = \frac{DT_s\left(V_{Cq2}\right) + (1-D)T_s\left(-V_{Cq1}\right)}{T_s} = 0 \quad (12)$$

$$V_{Lq2} = \frac{DT_s\left(V_{Cq1} + V_s\right) + (1-D)T_s\left(V_s - V_{Cq1}\right)}{T_s} = 0 \quad (13)$$

$$V_{Cq1} = \frac{D}{1-2D} V_S \quad (14)$$

$$V_{Cq2} = \frac{1-D}{1-2D} V_S \quad (15)$$

The integrated bidirectional buck/boost converter connecting ESUs and PV shares switches $S_1$ and $S_2$ with the H-bridge converter connecting the load and PV. The following formula is used to determine the transfer function during buck mode of operation of buck/boost converter, which is defined as the ratio of the output voltage ($V_{Cq2}$) to the input voltage ($V_{PV}$).

$$\frac{V_{Cq2}}{V_{PV}} = 1 - D \quad (16)$$

The $V_S$ voltage can be derived in terms of $V_{PV}$ by rearranging the Eq.15 and Eq.16.

$$V_S = V_{PV}(1-2D) \quad (17)$$

The ratio of $V_{Cq1}$ and $V_{PV}$ can be computed by substituting the $V_S$ (Eq.17) in Eq.14.

$$\frac{V_{Cq1}}{V_{PV}} = D,\ V_{Cq1} = V_{bat} \quad (16)$$

The supercapacitor and battery voltages are taken into account while calculating the duty cycle. However, the duty cycle is the only factor that affects the PV and battery ratio.

Depending on the duty cycles of complementary switches $S_1$ and $S_2$, the system functions as a bidirectional buck-boost converter. As can be calculated using Eq. 16;

$$\begin{cases} Buck\ Mode\ \ D\ \geq 50\% \\ Boost\ Mode\ \ D < 50\% \end{cases} \tag{17}$$

An equivalent circuit model of the converter equipped with primary-side H-bridge and secondary-side rectifier circuits is created, as demonstrated in Figure 3.11, to make it easier to analyze the relationship between PV and load. A square-wave voltage source is used to represent the secondary side of HFT and the full-bridge converter. The resonant tank is made up of a series-connected inductor *Lr* and a capacitor *Cr*.

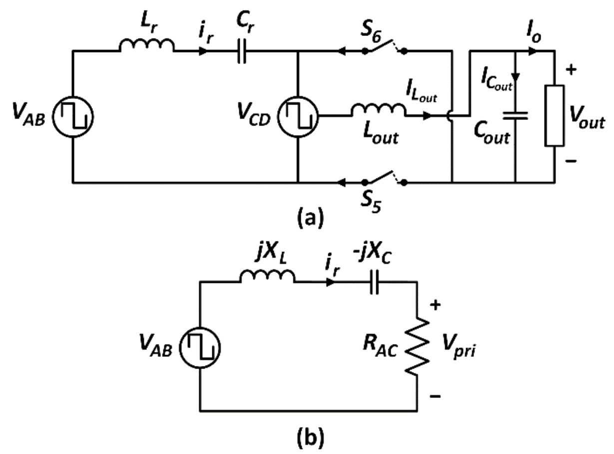


**Figure 3.11.** Equivalent circuit of the converter (a) with rectifier circuit, (b) with ac equivalent resistance

In order to ensure ZVS and little stress on the resonant tank, the resonance frequency ($f_r$) is chosen just slightly below the switching frequency ($f_{sw}$). The $f_r$ in Eq. (11) resonates with the tank. The system runs in continuous conduction mode (CCM), and the rectifier stage may be treated as a simple AC circuit because the operational condition in Eq. (12) is true, and the load current is almost sinusoidal. It is anticipated that the suggested converter employs a capacitive output filter with a large enough capacitance to produce a constant output voltage. As a result, the equivalent AC resistance of the rectifier load is calculated using Eq (13).

$$f_r = \frac{1}{2\pi\sqrt{L_r C_r}} \tag{18}$$

$$f_r < f_{sw} \tag{19}$$

$$R_{ac} = \frac{8\,R_o}{\pi^2} \tag{20}$$

The quality factor can be derived in terms of $R_{ac}$ considering the characteristic impedance $Z_r = \sqrt{L_r/C_r}$ as follows,

$$Q = \frac{Z_r}{R_{ac}} \tag{21}$$

The connection between the PV voltage and the load voltage is computed using the AC equivalent circuit in Figure 3.11(b).

$$M = \frac{V_{out}}{V_{PV}} = \frac{\sin(\frac{\pi}{2}D)}{\sqrt{1 + Q^2\left(\frac{f_{sw}}{f_r} - \frac{1}{\frac{f_{sw}}{f_r}}\right)^2}} \tag{22}$$

where M is the gain, $V_{out}$ and D represent the output voltage and duty cycle of $S_1/S_3$.

The qZ_RiMPC has three different operating modes:

- Mode 1 corresponds to the requirement that PV feeds both the load and the ESUs,
- Mode 2 to the requirement that the ESUs buffers while PV feeds the load,
- Mode 3 to the requirement that the ESUs is fed through the DC microgrid at the appropriate times.

Additionally, the power transfer from ESUs to load is provided, and the power transfer from battery to supercapacitor is conducted out by a quasi-Z-source converter that enables independently regulating the currents of each ESUs unit. Table 1 displays the switching states of the converter that were developed considering the various operation modes. Combining the four switching states of the H-bridge converter, the three switching states of the controlled full-wave rectifier, and the two switching states of the quasi-Z-source converter results in the switching patterns of the qZ_RiMPC. The power flow direction of the ESUs and gain of the quasi-Z-source converter are controlled by duty cycle control, whilst power transfer is carried out by phase shift modulation in the pertinent switching cycles. In addition, duty cycle control and phase shift control enable Perturb and Observe (P&O), MPPT, and CC/CV charging controls.

**Table 1**. Switching Patterns of switch for modes of qZ_RiMPC

| | | Switch Positions | |
|---|---|---|---|
| **Switching States** | Operation Modes | $S_1$, $S_2$, $S_3$, $S_4$,-$S_z$ | $S_5$, $S_6$ |
| **1** | Mode 1 | 1001-0 | 00 |
| **2** | | 1010-0 | 00 |
| **3** | | 0110-0 | 00 |
| **4** | | 0101-0 | 00 |
| **5** | Mode 2 | 1001-1 | 00 |
| **6** | | 1010-1 | 00 |
| **7** | | 0110-0 | 00 |
| **8** | | 0101-0 | 00 |
| **9** | Mode 3 | 0001-0 | 10 |
| **10** | | 0001-0 | 01 |
| **11** | | 0001-0 | 01 |

# 4. CONTROLLER MODELLING

## 4.1. Interleaved Based Isolated Multiport Converter

As seen in Figure 4.1, the interleaved based isolated multiport DC-DC converter system's controller is consisted of several control loops, including MPPT, CC, CV, and load control loops. In collaboration with the management algorithm shown in Figure 4.2, the suggested controller structure chooses the most suitable control loop while considering the power of the PVs, the demand of the loads, and the battery state to offer the best power flow between the PVs, batteries, and loads. The top priorities of controller are;

1. To maintain the continuity of their voltage and to continuously provide loads with electricity,
2. In order to increase the battery's service life, CC and CV charging methods are used.
3. To guarantee the PV generates the most electricity possible.

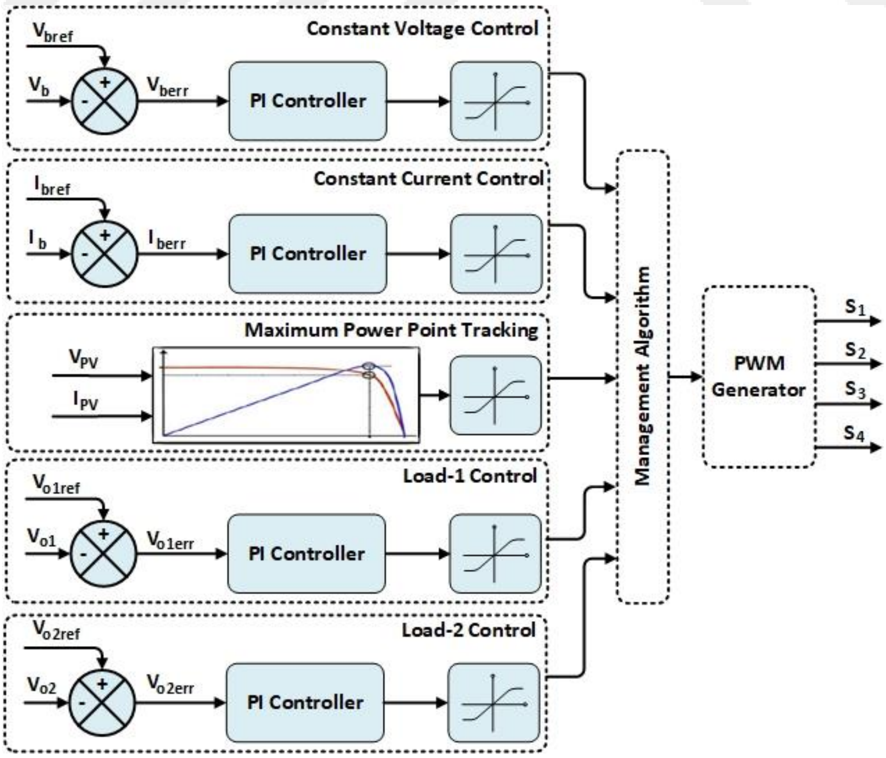


**Figure 4.1.** Controlling the Interleaved Based Isolated Multiport Converter Topology Effectively

In accordance with the PV and load instantaneous states, the suggested topology features two distinct operating modes.

1. **Mode 1:** In comparison to the power required by the loads, it equates to a lower instantaneous PV power. This happens when loads are using a lot of electricity or when there is little sunlight. In this mode of operation, the battery compensates for the PV to maintain consistent load voltages and deliver continuous power to the loads.As a consequence, both the PV and the battery are used to send electricity to the loads.
2. **Mode 2:** The PV has the capacity to provide more energy than the loads need. In this functioning mode, the extra energy of PV is transmitted to the battery to recharge it. As a result, the battery may be charged by the PV while the loads continue to get electricity.

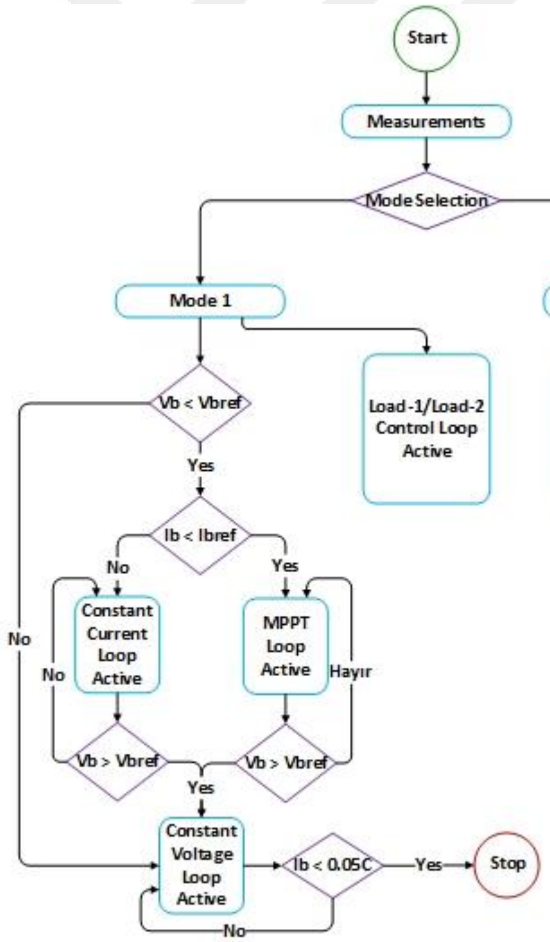


**Figure 4.2.** Power Flow Control Algorithm of Switch Capacitor Based Multiport DC-DC Converter

The relevant controllers govern the flow of power, and the management algorithm determines when to switch between control loops. The MPPT, CC, and CV control loops are switched while the load control loops are continually engaged. Since they all control the same switching element, MPPT, CC, and CV control loops are incompatible.

The $S_3$ and $S_4$ switching elements are utilized to regulate the load voltages in the load control loop. The $S_3$ and $S_4$ trigger signals have a $180^{\circ}$ phase difference and can have duty cycle levels between 5% and 50%. According to the power consumption of the loads, the PI control technique determines the duty cycle value. As of right now, duty cycle value of switch $S_3$ controls the voltage for load 1 whereas duty cycle value of switch $S_4$ controls the voltage for load 2.

To get the most power possible out of the PV is the goal of the MPPT control loop. The P&O approach, which has the characteristics of low computational load and usability, is commonly utilized in the literature and in applications to accomplish the maximum power extraction procedure. The controller determines the instantaneous available power by monitoring the PV output voltage ($V_{PV}$) and current ($I_{PV}$). Additionally, the controller monitors the power change by shifting the PV output voltage in a certain direction while taking the computed power change into account. In light of the computed power, the MPPT control loop dynamically determines the duty cycle value and activates switches $S_1$ and $S_2$.

When the rapid PV power surpasses the total loads power, the CC control loop is designed to make sure that the battery is charged with a CC. Half of the battery nominal capacity is represented by the CC figure, or maximum charging current. The system battery has a nominal capacity of 100 Ah. Therefore, a maximum of 50 A can be used to charge the battery. By comparing the observed battery charging current ($I_b$) with the reference ($I_{bref}$) 50A values and applying the resultant error value ($I_{berror}$) to the PI controller, the CC control loop establishes the duty cycle values of switches S1 and S2. A CV control loop comes after the CC control loop. After the battery reaches the designated maximum voltage value, this control loop which may be seen as a continuation of the CC control is turned on. The battery pack charging current declines exponentially under CV management, and the charging process is complete when the charging current equals 0.5% of the nominal battery capacity. By comparing the observed battery voltage ($V_{bat}$) with the battery reference voltage ($V_{bref}$), 82.5 V, and applying the resultant battery error value ($V_{berr}$) to the PI controller, the CV control loop calculates the duty cycle values of switches $S_1$ and $S_2$.

## 4.2. Switch Capacitor Based Isolated Multiport Converter

Figure 4.3 depicts the intricate control framework. The three major goals of the overall controller system are to

1. Enable bidirectional power flow between the ports,
2. Transfer surplus power generated by PV to the battery,
3. Assure the continuity of power transfer to the load with constant DC-link voltage.
4.

Power flow management, MPPT, CC/CV charging, and DC-link control consists of the multi-loop control structure that serves as the switch capacitor based isolated multiport converters efficient control structure. To transition between the control loops instantly, the system uses adaptive operation.

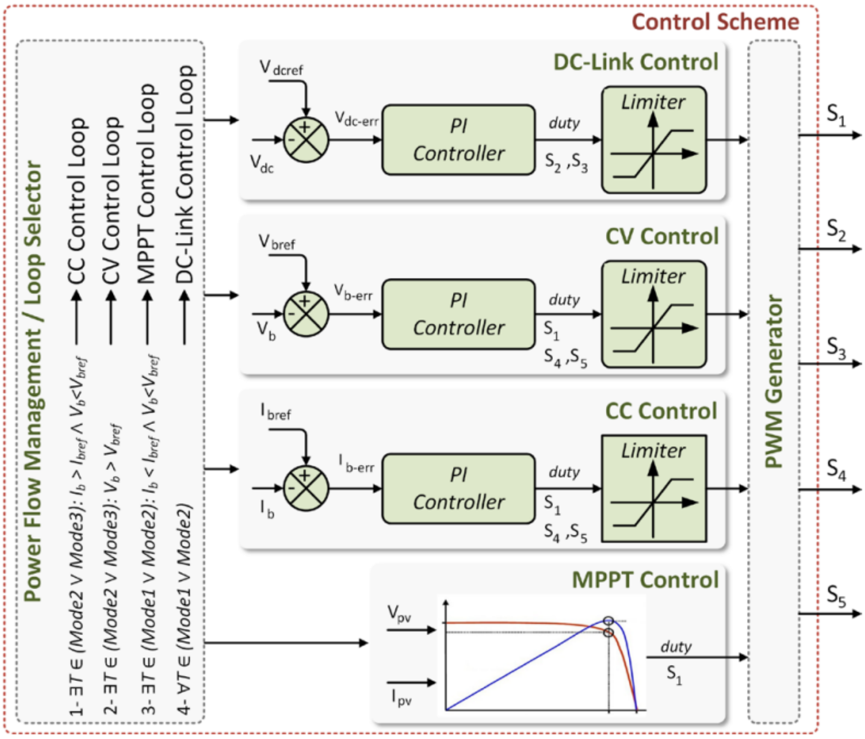


**Figure 4.3.** Control Scheme of the Switched-Capacitor Multiport DC-DC Converter

The fundamental goal of the switch-capacitor multiport DC-DC converter operation is to provide the best possible power flow between input energy units and the output load considering instantaneous PV generation, battery charge characteristics, and load changes. There are three distinct power flow scenarios, known as mode 1, mode 2, and mode 3, based on the current statuses of the ports. Power is sent to the load in Mode 1 through PV and batteries. The battery operates in discharging mode in this mode. In mode 2, PV charges the battery while in mode 1 it feeds the load. The reverse power flow, which is from the load side to the battery, is represented by mode 3. The battery runs in charging mode in this mode.

In mode 1, the PV and batteries are both used to power the load simultaneously. There are two scenarios that may occur in this situation. When the load power consumption is more than the PV power that is available, the main condition may occur. The battery buffers the PV during this period to send electricity to the load continuously. The PV operates below its rated power as a result of environmental factors like irradiation (i.e., the PV output power falls as irradiation increases). The analytical connection between the power flows is shown in the following equation.

$$\int_{t_0}^{t_1} P_{load}(t)dt = \int_{t_0}^{t_1} P_{pv}(t)dt + \int_{t_0}^{t_1} P_{bat}(t)dt \quad (23)$$

In mode 2, the load, namely the electricity generated by the PV, feeds the load, and charges the battery simultaneously. Under low load consumption ratings, this scenario is possible. When the low power is utilized, the PV power could be reduced. The battery must be charged to maintain the DC-link voltage constant by buffering the PV in situations where the PV generation is insufficient to serve the load. In situations where the battery state of charge is below 100%, the PV surplus electricity is used to charge the battery. During this time interval, power flows are expressed mathematically in the following equations.

$$\int_{t_1}^{t_2} P_{load}(t)dt = \int_{t_1}^{t_2} P_{pv}(t)dt - \int_{t_1}^{t_2} P_{bat}(t)dt \quad (24)$$

In charging mode 3, the load side of the battery is used. In this scenario, the battery could be charged by the DC-microgrid to which the load is attached even when there is no solar radiation. In this manner, there is no power passing through the PV. The following is how the power flow for this condition is expressed:

$$\int_{t_2}^{t_3} P_{load}(t)dt = \int_{t_2}^{t_3} P_{bat}(t)dt \quad \int_{t_1}^{t_2} P_{pv}(t)dt = 0 \quad (25)$$

While the later control loops are activated taking into account the immediate power production value of PV, the power transfer towards the load is continually carried out utilizing the DC-link control loop. The CC/CV charging algorithms are used to transmit electricity from the load side to the battery. The usage of the pulse width modulation (PWM) technique is a feature that unites the aforementioned control loops. By altering the voltages of the output DC-link and battery-coupled DC busbar, the duty cycle values of the switches control the power flow rating.

By activating $S_2$ and $S_3$ switching components, the DC-link control loop controls the output DC-link voltage. Switches $S_2$ and $S_3$ have duty cycles that range from 0 to 50%, with a 180-degree phase difference among them. The relevant switches open simultaneously and short circuit with a duty cycle of more than 50%. Using a PI controller, the duty cycles of the switches are calculated. The PI controller receives the difference between the reference ($V_{dcref}$) and actual voltages ($V_{dc}$) of the output load.

Activation of the MPPT control loop occurs in mode 1 and in some mode 2 conditions. By activating the $S_1$ switching device, the MPPT control loop is employed to maximize the power from the PV. Due to its simplicity and light computing effort, the P&O MPPT approach is used to track maximum power. The controller calculates the instantaneous available power while monitoring the output voltage ($V_{pv}$) and current ($I_{pv}$) of the PV. The algorithm modifies the duty cycle of switch $S_1$ to disturb the operational voltage in order to assure maximum power.

Computing the instantaneous duty cycle of the $S_1$ switch results in the operational voltage perturbation as follows;

$$D_{new} = D_{old} + \Delta D \quad (if\ P > P_{old}) \tag{26}$$

$$D_{new} = D_{old} - \Delta D \quad (if\ P < P_{old}) \tag{27}$$

$$D_{new} = D_{old} \quad (if\ P = P_{old}) \tag{28}$$

One of the MPPT or CC control loops must be enabled for surplus PV power to be made accessible. The battery charging scenario is crucial for extending the battery useful life. As a result, the battery charge current is typically limited to 0.5 C (where C stands for the battery nominal capacity).

The associated control loops are enabled while taking the battery charging current restrictions into account. The MPPT control loop changes to the CC control loop if the battery charge current exceeds the charge current limit. The battery voltage is increased by the CC control loop to reach its reference level of 242 V. After the CC loop has finished operating as specified, the CV control is activated. The CV control loop continues to charge until the charging current slowly drops to 0.05C. The duty cycle of the switch S1 is changed to accomplish CC/CV charging. Additionally, mode 3, which is another stage of power flow towards the battery, also has the CC/CV control loops active. Utilizing PI controllers and enabled associated control loops, the duty cycle value of the S1 switch is calculated. The CV control loop computes the duty cycle by using the error value there among the reference ($V_{bref}$) and actual ($V_b$) values of the battery voltage, whereas the CC control loop uses the difference there among the battery current reference ($I_{bref}$) and actual ($I_b$) values to determine the duty cycle.

### 4.3. Quasi Z-Source Multiport Converter

Many control goals are achieved by the qz_iMPC system controller, including power flow management, MPPT, CC/CV charging, and DC-link control. The controller's power allocation capabilities enables for the optimum possible power flow between the PV, ESU, and EM. Power flow management's key objectives are to

1. Maintain the EM's supply while taking into account the PV and ESU's restrictions.,
2. To offer negative power flow in order to recover braking energy.

The overarching controller structure seen in Figure 4.4 is responsible for controlling the whole system.

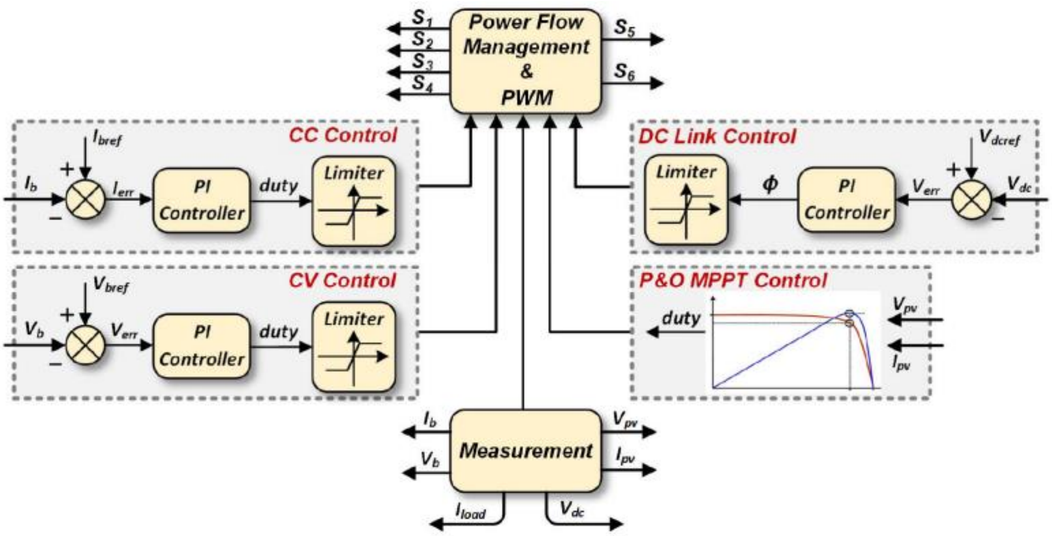


**Figure 4.4.** Overall Control Structure of Quasi Z-Source Converter

The strategy management of the power flow determines the system operation mode based on the amount of PV power available, EM demand, and ESU status, such as

Mode 1: This mode, the PV power ($P_{PV}$) is higher than the EM ($P_{EM}$) requirement for power. Energy can be stored in excess in the ESU ($P_{ESU}$) in this state. The following equations show how PV provides reference powers to the EM while charging the battery and supercapacitor:

$$P_{PV} > P_{EM} \tag{29}$$

$$P_{ESU} = P_{PV} - P_{EM} \tag{30}$$

Mode 2: In mode 2 implies a lower PV power than is required by the EM. The ESU should serve as a buffer in this situation since there is a paucity of energy. As a result, both the PV and the ESU feed the EM. The following equations provide the reference powers:

$$P_{PV} < P_{EM} \tag{31}$$

$$P_{EM} = P_{PV} - P_{ESU} \tag{32}$$

Mode 3: When an EV with regenerative capabilities brakes, this mode reflects the braking force that is applied. In this condition, energy is converted from kinetic energy to electrical energy and stored in the ESU. So, the EM charges the battery and supercapacitor. The following equations provide the reference powers:

$$P_{PV} = 0 \tag{33}$$

$$P_{EM} = P_{ESU} \tag{34}$$

The operation of the qZ-iMPC is regulated to operate in various modes in accordance with the various PV and EM power values. It is possible to realize an automated switch between these modes by spreading the control domain effectively. The suggested converter's control diagram is shown in Figure 4.4. The P&O MPPT, DC-link, CC, and CV control loop are the four control loops. Under situations of forward power flow, a modified phase-shift modulation method is used to regulate the full-bridge. The duty cycles of complimentary switches $S_1$ and $S_2$ change depending on the state defined by the management system of the power flow, but the duty cycles of switches $S_3$ and $S_4$ have a constant duty cycle (50%) with a 180° phase shift between them. While the duty cycle of the switches $S_1$ and $S_2$ gives maximum power transfer by managing the output voltage of the PV or enables bidirectional power flow for the ESU, the phase shift between $S_1$ and $S_4$/$S_2$ and $S_3$ provides DC-link control.

The P&O MPPT technique performs the highest power transfer due to its simplicity and low computing burden. The controller calculates instantaneous available power while monitoring PV output voltage and current. To provide maximum power, the algorithm modifies the operating voltage. A pseudo-code in Figure 4.5 explains the P&O method operating algorithm.

```
begin
number v, v_old, i, p, p_old, ref, ref_old, ref_delta
input v,i
p = v*i
if ((p – p_old) != 0) then
        if ((p – p_old)  <  0) then
                if (v – v_old < 0) then
                        ref = ref_old – ref_delta
                else
                        ref = ref_old + ref_delta
                endif
        else
                if (v – v_old < 0) then
                        ref = ref_old + ref_delta
                else
                        ref = ref_old – ref_delta
                endif
        endif
else
        ref = ref_old
endif
ref_old = ref
v_old = v
p_old = p
output ref
end
```

**Figure 4.5** P&O Pseudo-code

The PV excess power is purportedly transmitted to the ESU during mode 1 using the CC-CV charging algorithms.

The controller limits the charging current to 0.5 C, which is equal to the capacity of the battery pack. The controller maintains a steady charge current until the battery pack charge current reaches the reference value of 30 A ($I_{bref}$). The CC control continues until the battery voltage reaches 217.8 V ($V_{bref}$), the reference value. The CV charging comes after the CC charging, and once the charge current reaches 0.05 C, the charging procedure is finished. By adjusting the duty cycles of the switches $S_1$ and $S_2$, the CC-CV charging is accomplished. Additionally, $S_5$ and $S_6$ switch duty cycles in mode 3 are modified to execute CC-CV charging. For each control, the difference between the calculated reference current ($I_{bref}$)/voltage ($V_{bref}$) and the measured current ($I_b$)/voltage ($V_{bat}$) is acquired and implemented to the PI controllers for the CC and CV charging algorithms, in turn.

In mode 2, the DC-link reference voltage is controlled by the ESU and PV via P&O MPPT control and DC-link control loops. Between the $S_1$ and $S_4$/$S_2$ and $S_3$ there is a phase shift angle adjustment made by the DC-link controller. To determine the error, the measured DC-link voltage ($V_{dc}$) is taken out from the reference value of the EM DC-link voltage ($V_{dcref}$). To produce the phase shift angle (ø), the error signal is sent into the PI controller. The system overall control algorithm is shown in Figure 4.6.

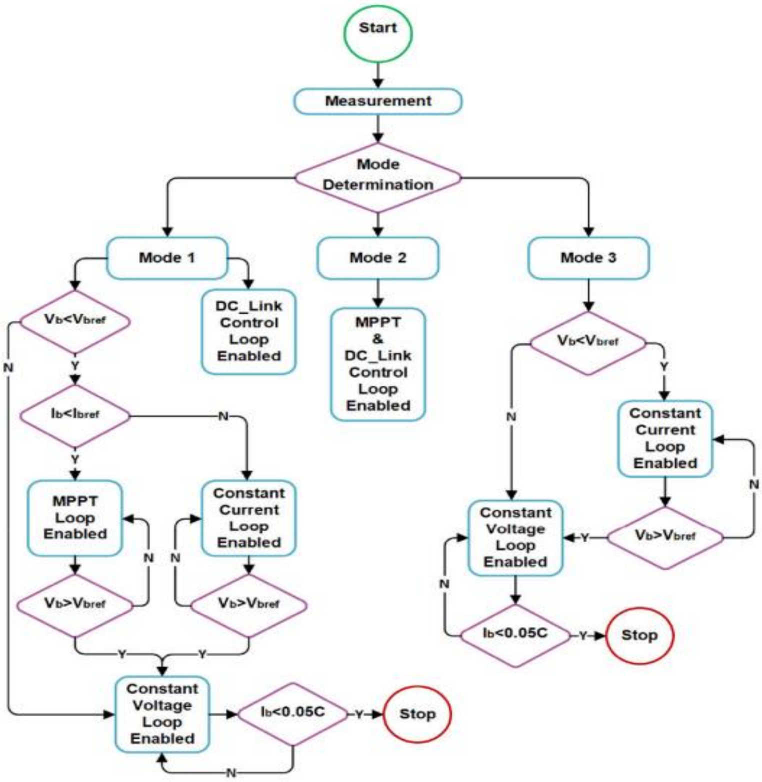


**Figure 4.6.** Overall Control Algorithm of Quasi Z-Source Multiport Converter

$$\text{CC Charging } V_b < V_{bref} \text{ and } I_b \geq I_{bref} \quad (35)$$

$$I_b \text{ Charging } V_b < V_{bref} \text{ and } I_b < I_{bref} \quad (36)$$

$$CV \text{ Charging } V_b < V_{bref} \quad (37)$$

## 4.4. Resonant Tank Integrated Isolated Quasi Z-Source Multiport Converter

A multi-loop control system is what the suggested converter is made of. The controller is made up of an MPPT loop, a DC-Link control loop, a CV loop, and a CC loop. The system has an instantaneous transition between controller loops and functions adaptively. As a result, the linked controller scheme uses a controller scheduling technique and is a form of closed-loop system. The controller primary goals are;

(i) Maintain the dc link voltage,

(ii) Use the CC/CV charging algorithm to prolong battery life,

(iii) Maximize PV power,

(iv) Charge and discharge the supercapacitor independently of the battery.

In Figure. 4.7, the controller for the entire system is depicted.

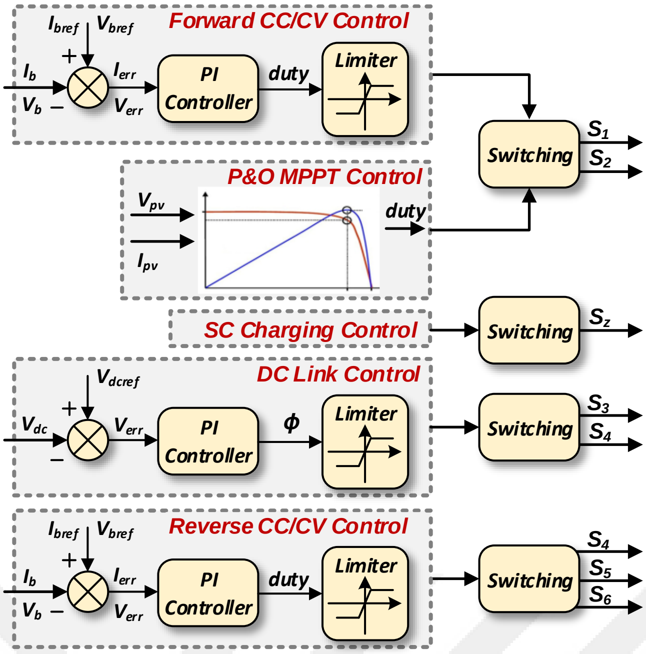


**Figure 4.7.** Control Scheme of the qZ_RiMPC

Phase shift and duty cycle control are the two primary control methods used in the qZ_RiMPC. Phase shift control is used to govern the power flow between the main and secondary sides, whereas duty cycle control is used for MPPT, CC/CV charging, and supercapacitor charging and discharging. The phase shift control alters the H-bridge shift angle between the left and right legs. Switches $S_3$ and $S_4$ on the right leg have a fixed duty cycle of 50% and a 180° phase shift between them. The enabled control loop modifies the duty cycle of the complementary left leg switches $S_1$ and $S_2$. Under circumstances of forward power flow, the phase shift angle is continuously adjusted by the DC-Link control loop. When the PV generation power or load demand power is different, the latter control loops are enabled considering the modes of operation that are stated in Eq. (38) in the qZ_RiMPC system. An automated switch between these modes is made possible by tracking the current condition of every port.

$$\begin{cases} Mode\ 1\ P_{PV} > P_{LOAD}, & P_{ESUs} = P_{PV} - P_{LOAD} \\ Mode\ 2\ P_{PV} < P_{LOAD}, & P_{LOAD} = P_{PV} + P_{ESUs} \\ \quad Mode\ 3 \quad P_{PV} = 0, & P_{ESUs} = P_{DC-Link} \end{cases} \tag{38}$$

To maintain the DC-Link voltage constant at the target value of 350 V, the qZ_RiMPC DC-Link control loop executes phase-shifting operations on the primary side. With the aid of a PI controller, the phase shift value is calculated. The observed DC-Link voltage is taken out from the established reference value to calculate the error signal. The PI controller is then sent the error signal. The controller calculates the H-bridge legs' phase shift angle.

While the DC-link control loop is engaged continually, the other control loops are triggered based on the various operating modes. According to Eq. (38), the extra PV power is transmitted to the ESUs during mode 1 using either the MPPT or CC/CV charging algorithm, depending on the charging power. The controller employs the CC/CV charging algorithm to manage the charging current when the charging power is high. If not, the MPPT algorithm is applied to draw the most electricity possible from PV. Based on the battery voltage and level of charge, the CC/CV charging algorithm works. As long as the battery voltage gets its reference value of 378 V, the CC control sets the charging current of the battery to 0.5C (rated battery pack capacity is regarded as 1C). After the mentioned CC loop procedure is complete, the CV control is activated. Up until the charging current progressively drops to 0.05C, the CV is still charging. By altering the duty cycle of the switches $S_1$ and $S_2$, the CC/CV charging is accomplished. In addition to mode 1, which is another power transfer state geared towards ESUs, mode 3 also employs CC / CV charging algorithms.

During both ESUs charging and discharging processes, the MPPT control loop is enabled. The conventional P&O MPPT technique is employed in the qZ_RiMPC system because of its simplicity and lower processing effort. The duty cycle of the switches $S_1$ and $S_2$ is changed by the controller to extract the most power possible. The associated approach is dependent on the PV voltage-power characteristic. The controller continually records the PV instantaneous voltage and current measurements as well as the power it has harvested at each sample interval. The controller modifies the PV output voltage in two directions in response to changes in the positive and negative extracted power from the PV.

Because of its quicker reaction to inrush current during transient to relieve the burden on the battery, the supercapacitor is utilized as a collaborator. In the second operating mode, the supercapacitor may be charged both concurrently with the battery charging and concurrently with the battery discharging. The battery can tolerate transitory circumstances since the supercapacitor is continually charged. By turning on the switch $S_z$, independent control of the supercapacitor charging current is enabled in addition to the aforementioned control loops. Figure 4.8 contains the overall controller flowchart.

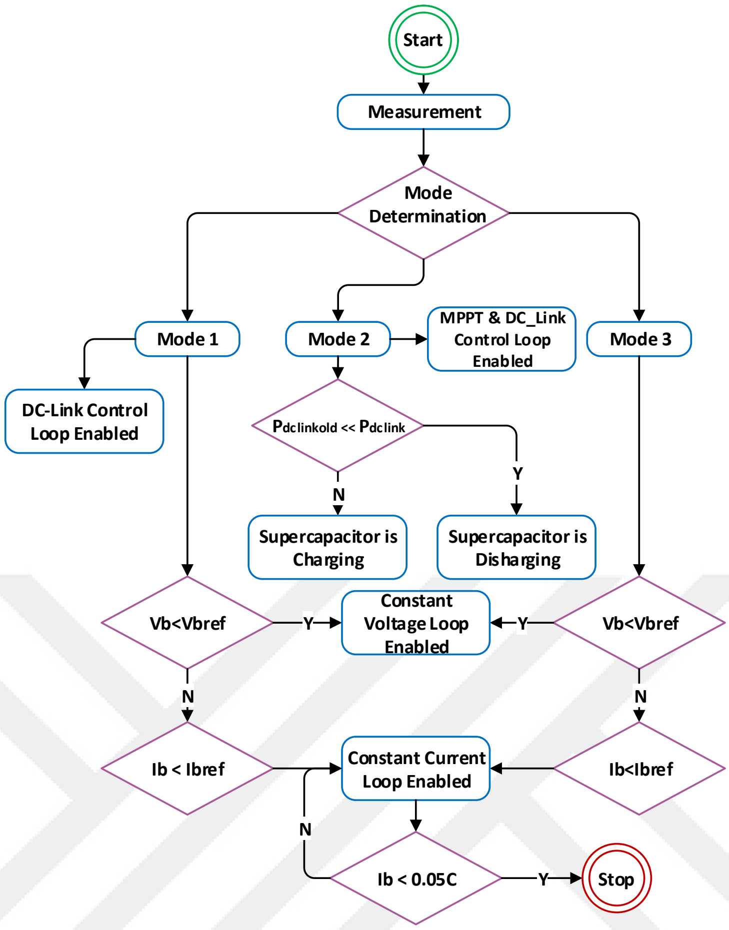


**Figure 4.8.** Flowchart of the qZ_RiMPC

# 5. SIMULASTION STUDY AND PERFORMANCE ANALYSIS

## 5.1. Interleaved Based Isolated Multiport Converter

In the PSIM simulation environment, simulation investigations of the interleaved based isolated MPC and controller are conducted. In the simulation experiments, 10 kW electricity is produced utilizing 1Soltech Company's 1sth-215-p seven parallel seven series PV. A 72 V 100Ah battery also serves as additional support for the PV. The loads have voltage levels of 60 Vdc and 40Vdc, and modeling tests have revealed that each load may consume up to 2 kW of electricity. Table 2 contains the simulation model parameters. Two case studies are utilized to evaluate the efficacy of the interleaved based isolated multiport converter modes and control loops. Table 3 provides a summary of these case studies.

**Table 2.** System Parameters of Interleaved Based Isolated Multiport Converter

| System | Parameter | Unit |
|---|---|---|
| **PV** | Maximum Power (1000 W/$m^2$ ) | 10500 W |
| | MPP Voltage (1000 W/$m^2$ ) | 207 V |
| | MPP Current (1000 W/$m^2$ ) | 50 A |
| **Battery** | Capacity | 100 Ah |
| | Nominal Voltage | 72 V |
| | Maximum Charge Voltage | 82.5 V |
| | Maximum Charge Current | 50 A |
| **Interleaved Converter** | Inductor ($L_1$) | 20 uH |
| | Inductor ($L_2$) | 20 uH |

**Table 2.** System Parameters of Interleaved Based Isolated Multiport Converter (Continued)

| | | |
|---|---|---|
| **General** | Nominal Voltage of Load-1 | 60 V |
| | Output Capacitor of Load-1 | 1 mF |
| | Nominal Voltage of Load-2 | 40 V |
| | Output Capacitor of Load-2 | 1 mF |
| | Switching Frequency | 20 kHz |
| | HFT Magnetizing Inductance | 1 mH |
| | HFT Primer Leakeage Inductance | 4 uH |
| | HFT Seconder Leakeage Inductance | 4 uH |
| | HFT Turn Ratio | 1:1 |

**Table 3.** Case Studies of Interleave Based Isolated Multiport Converter

| | **Case Study – 1** | | | | **Case Study – 2** | | |
|---|---|---|---|---|---|---|---|
| **Time** | 0-0,02 | 0,02-0,04 | 0,04-0,063 | 0,063-0,08 | 0- 0,02 | 0,02-0,04 | 0,04-0,06 |
| **Radiation (W/m$^2$)** | 300 | 600 | 1000 | 1000 | 350 | 350 | 350 |
| **Temperature (oC)** | 25 | 25 | 25 | 25 | 25 | 25 | 25 |
| **Load-1 Power (W)** | 2000 | 2000 | 2000 | 2000 | 2000 | 1000 | 1000 |
| **Load-2 Power (W)** | 2000 | 2000 | 2000 | 2000 | 2000 | 2000 | 1500 |
| **Battery Charge/Discharge** | Discharge | Charge | CC Charge | CV Charge | Discharge | Charge | Charge |
| **Mode** | Mode 1 | Mode 2 | Mode 2 | Mode 2 | Mode 1 | Mode 2 | Mode 2 |

In the first case study in Figure 5.1, the PV and battery can both transfer power to the loads simultaneously as well as show the effectiveness of the MPPT and battery charging algorithms that the battery is in the charging state. This illustrates the applicability of the MPPT, CC, and CV control algorithms. The system reactions and changes between these various operating modes and control loops are also examined, in addition to the power transfer states and control loops discussed in the first case study. With a steady state temperature of 25 °C, a 300 W/m2 irradiance, and a 4-kW total load demand, mode 1 is represented by the steady state time interval of 0-0.02 s. The PV instantaneous power generation value during this time period is lower than the total power required by the loads. To keep the loads powered up without interruption, the battery is depleted. During this period, MPPT and load control loops are in use.

The first case study irradiance is raised from 300 W/m$^2$ to 600 W/m$^2$ at 0.02 s, and the system dynamic response in the transient state is noticed. With irradiance of 600 W/m$^2$, a temperature of 25 °C, and a total load demand of 4 kW, mode 2 is represented by the steady state time interval of 0.02-0.04 s. The PV instantaneous power generation value during this time period exceeds the total power required by the loads. The MPPT and load control loops are active during the pertinent operation interval since the battery charging current is lower than the maximum charging current that has been defined.

The PV irradiance is raised from 600 W/m$^2$ to 1000 W/m$^2$ at 0.04 s of the first case study, and the PV power peaked at that time. With 1000 W/m$^2$ irradiance, 25 °C, and a total load demand of 4 kW, mode 2 is represented by the steady state period of 0.04-0.063 s. The battery charging current rose in tandem with the improved ability of the PV to produce electricity instantly, reaching its maximum charging current limit. As a result, the CC control loop is turned on throughout the pertinent period in place of the MPPT control loop, activating switches $S_1$ and $S_2$. The load control loops continue to manage the load voltages. The active control loop switches to the CV control loop when the voltage of battery arrives the designated reference voltage at 0.063 seconds into the initial state operation. The CV and load control loops are in operation in mode 2, which is represented by the power flow in the time range 0.063-0.08 s.

In the second case study, the suggested topology performance is examined for instantaneous load fluctuations while the PV temperature and irradiance remain constant. The second case study performance waveforms are displayed in Figure 5.2. The second case study's

0-0.02 s steady state time interval corresponds to mode 1 with 350 W/$m^2$ irradiance, 25 °C, and 2+2 kW load requirements. The PV powers the loads during the appropriate time, while the battery stores energy and releases it. The power requirements of load 1 and load 2 changed to 1 kW and 2 kW, respectively, at 0.02 s in the second case study. At that point, the battery begins to charge since the power depletion of the loads from the PV is less than the instantaneous PV output. Therefore, mode 2 is represented by the time range of 0.02-0.04 s. The power requirements of load 1 and load 2 changed to 1 kW and 1.5 kW, respectively, at 0.04 s in the second case study. The PV is simultaneously providing power to the loads and recharging the batteries throughout this period.

The performance waveforms include details on fluctuations in power flow as well as the projected converter efficiency. Considering the established operating modes, the efficiency of mode 1 is calculated to be 98%, but efficiency of mode 2 changes depending on the system active control loop. The computed efficiency values for mode 2 while the MPPT, CC, and CV control loops are engaged are 98%, 98.5%, and 98.5%, respectively. The suggested converter efficiency statistics demonstrate its usefulness in all conceivable power flow scenarios.

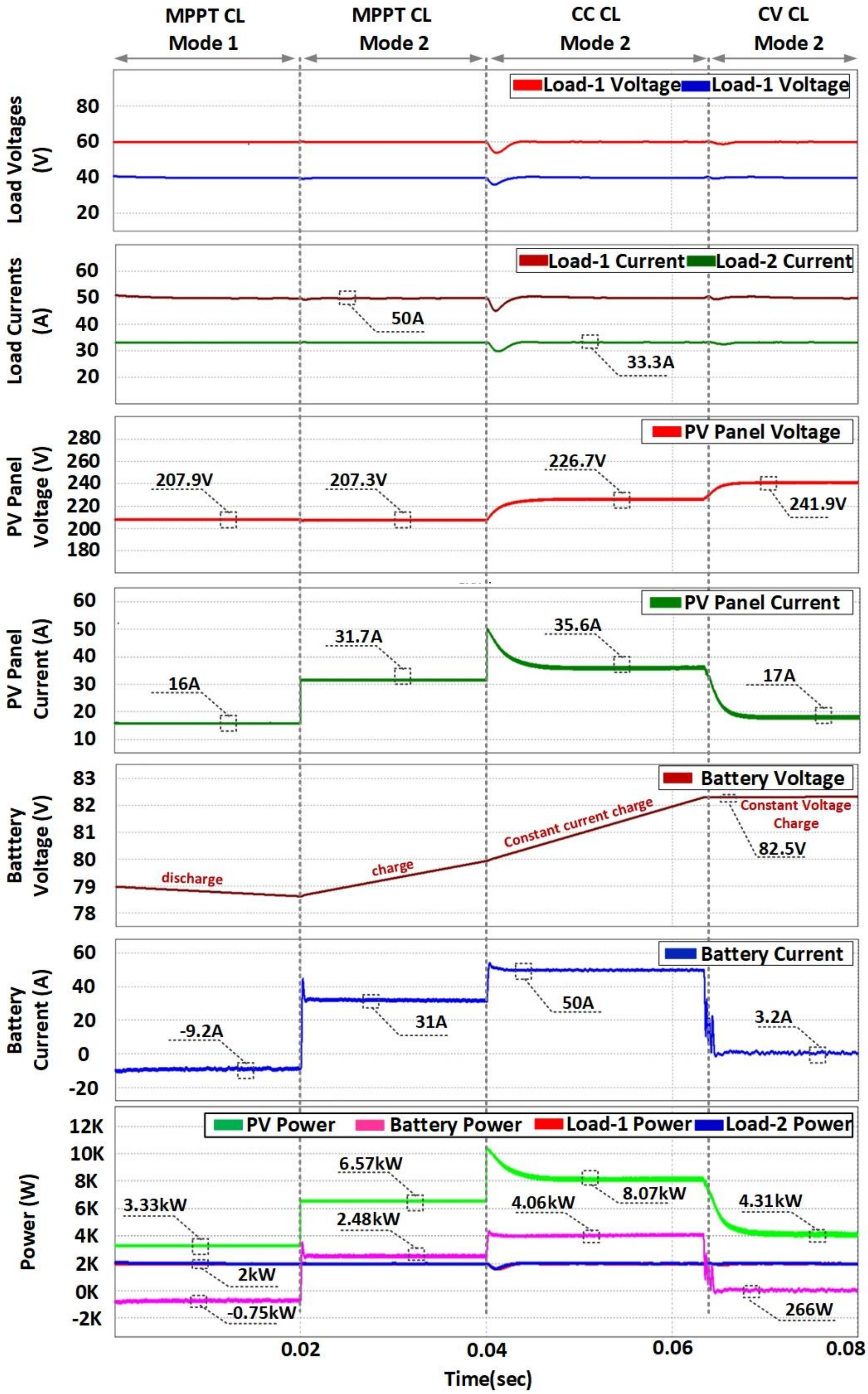


**Figure 5.1.** Case study "1" performance analysis of Interleaved Based Isolated Multiport Converter

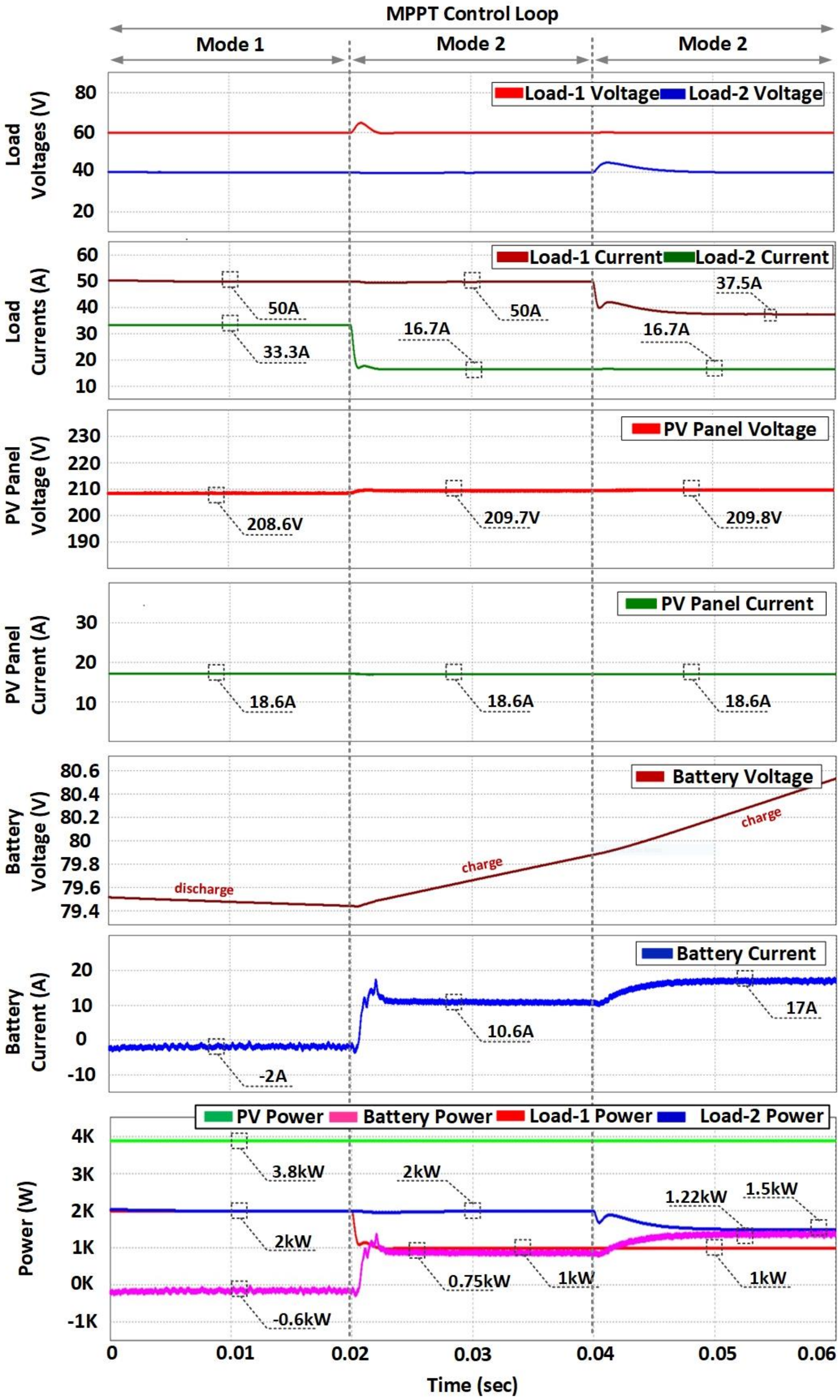


**Figure 5.2.** Case study "2" performance analysis of Interleaved Based Isolated Multiport Converter

## 5.2. Switch Capacitor Based Isolated Multiport Converter

In this part, a 3 kW proof-of-concept model consisting of 3 kW PV and a 220 V 12 Ah battery has been created using MATLAB/Simulink to assess the efficacy and practicality of the switch capacitor based MPC and the controller. Table 4 displays the simulation model parameters. Two case studies testing the switch capacitor based MPC performance in all operational modes are conducted. The case studies that are listed in Table 5 were created by adjusting the PV dosage and irradiation.

**Table 4.** Parameters of the Switch Capacitor Based Isolated MPC

| System | Parameters | Value |
|---|---|---|
| **PV** | Maximum Power (1000W/$m^2$) | 3197 W |
| | MPP Voltage (1000W/$m^2$) | 87 V |
| | MPP Current (1000W/$m^2$) | 36.75A |
| | Maximum Power (250W/m2) | 801.3 W |
| | MPP Voltage (250W/$m^2$) | 86.9 V |
| | MPP Current (250W/$m^2$) | 9.221 A |
| **Battery** | Capacity | 12 Ah |
| | Nominal Voltage | 220 V |
| | Maximum Charge Current | 6A |
| **Switched Capacitor** | Inductor ($L_{dc}$) | 1 mH |
| | Capacitor ($C_1$) | 250 uF |
| | Capacitor ($C_2$) | 250 uF |
| | Capacitor ($C_3$) | 500 uF |
| **General** | Half Bridge Capacitors ($C_4$, $C_5$) | 2 mF |
| | DC-Link Capacitor ($C_{out}$) | 1 mF |
| | Nominal DC-Link Voltage | 200 Vdc |
| | Switching Frequency | 200 kHz |
| | HFT Turns Ratio | 1:2:2 |

**Table 5.** Case studies of the Switch Capacitor Based Isolated MPC Details

| | Case 1 | | | | Case 2 | |
|---|---|---|---|---|---|---|
| **Time** | 0-0.25 s | 0.25-0.5 s | 0.5-0.75 s | 0.75-1 s | 0-0.25 s | 0.25-0.5 s |
| **Irradiation** | 300W/m$^2$ | 650W/m$^2$ | 1000W/m$^2$ | 1000W/m$^2$ | - | - |
| **Temperature** | 25 C$^{\circ}$ | 25 C$^{\circ}$ | 25 C$^{\circ}$ | 25 C$^{\circ}$ | - | - |
| **DC-Link Request** | 1500 W | 1500 W | 1500 W | 1500 W | -2000 W | -2000 W |
| **Battery Charge/Discharge** | Discharge | Charge | Charge (CC) | Charge (CV) | Charge (CC) | Charge (CV) |
| **Mode** | Mode 1 | Mode 2 | Mode 2 | Mode 2 | Mode 3 | Mode 3 |

The operating circumstances for the first example include those in which modes 1, 2, and all active control loops (MPPT, CC, CV, and DC-link) are in use, together with the state reactions of the transitions between these modes and loops. Different operating modes and active control loops are corresponding to various time intervals. Figure 5.3 depicts the switch capacitor based isolated MPC steady-state and dynamic responses during loop and mode changes. The findings show that the battery buffers and continuously powers the load when the instantaneous power value of the PV is less than the load demand.

The battery switches to charging in parallel with the rise in PV instantaneous power after the increase in irradiation. The MPPT control loop limits the power flow from the PV during the condition where it has relatively low output power, and the battery is overcharged. However, the CC control loop is triggered, and the battery current is limited in the case of high-power output from PV. The CV control loop kicks in when the voltage of battery gets a specific level and maintains the PV output voltage there. The power of the PV system grows with increasing irradiation to 1 kW, 2 kW, and 3 kW while the battery is first discharged and then charged to its maximum voltage value.

The second example shows mode 3 functioning, in which the DC microgrid charges the battery. The switch capacitor based isolated MPC steady-state and dynamic reactions under situations of reverse power flow are shown in Figure 5.4. A steady current is employed in this case study to charge the battery over the length of 0-0.5 s. The CC control loop modifies the battery charge current. Following CC charging, CV charging occurs between 0.5 and 1 seconds later.

The performance waveforms show that under various irradiation and loading fluctuations, the switch capacitor based isolated MPC, and controller smoothly manages the steady state and transient power sharing. Additionally, the switch capacitor based isolated MPC effectiveness has been assessed. Figure 4.3-4.4 shows that the efficiency values when taking the operating modes into account are 96%, 96.8%, and 90%, respectively. The suggested converter efficiency demonstrate its usefulness in all potential power flow scenarios.

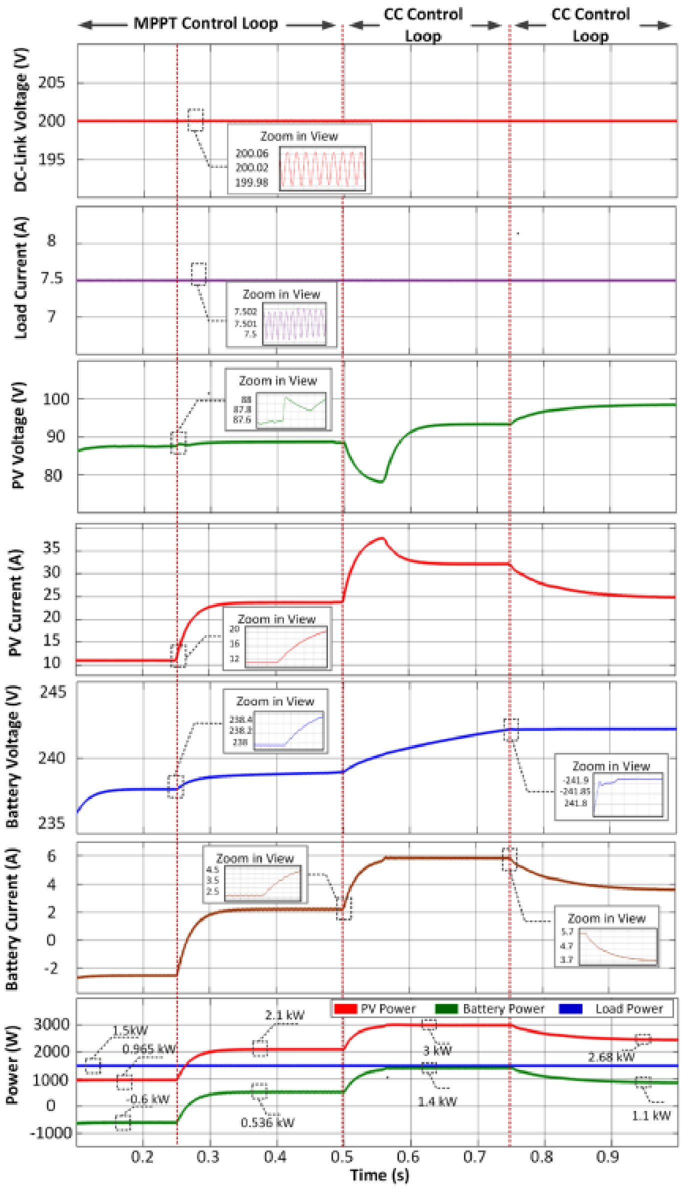


**Figure 5.3** Performance Results for Case 1 of the Switch Capacitor Based Isolated MPC

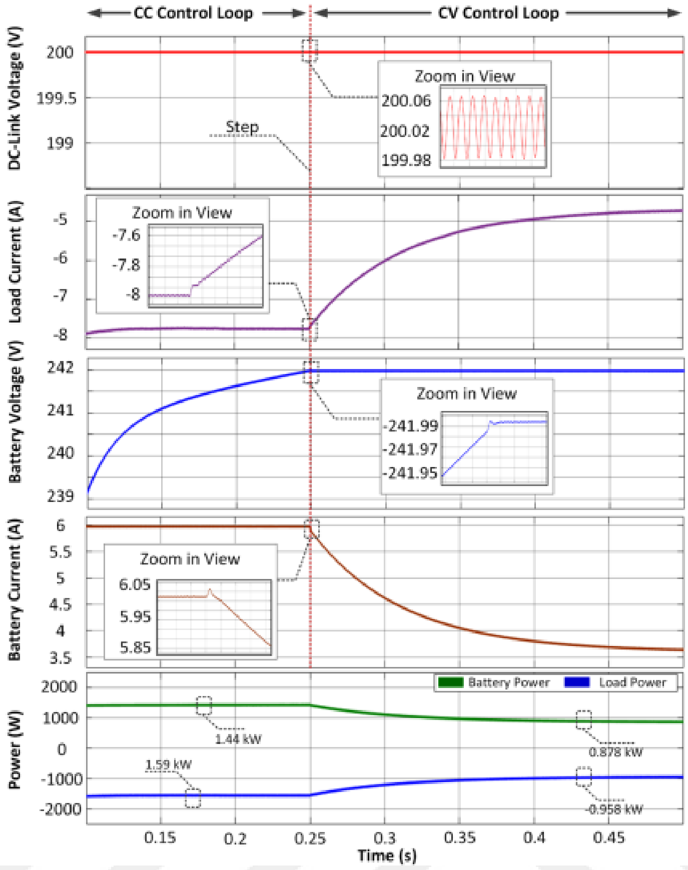


**Figure 5.4** Performance Results for Case 2 of the Switch Capacitor Based Isolated MPC

## 5.3. Quasi Z-Source Converter

The suggested qz_iMPC system performance evaluation is presented in this section. A standalone prototype for a PV powered 10 kVA EM and ESU is created in a MATLAB/Simulink platform to test the performance of the qz_iMPC and controllers. The 9.6 kW 1STH-215-P PV module from Soltech is employed in this investigation while the irradiation parameter is taken into account. Figure 5.5 depicts the characteristic PV curves with varied irradiance and constant temperature.

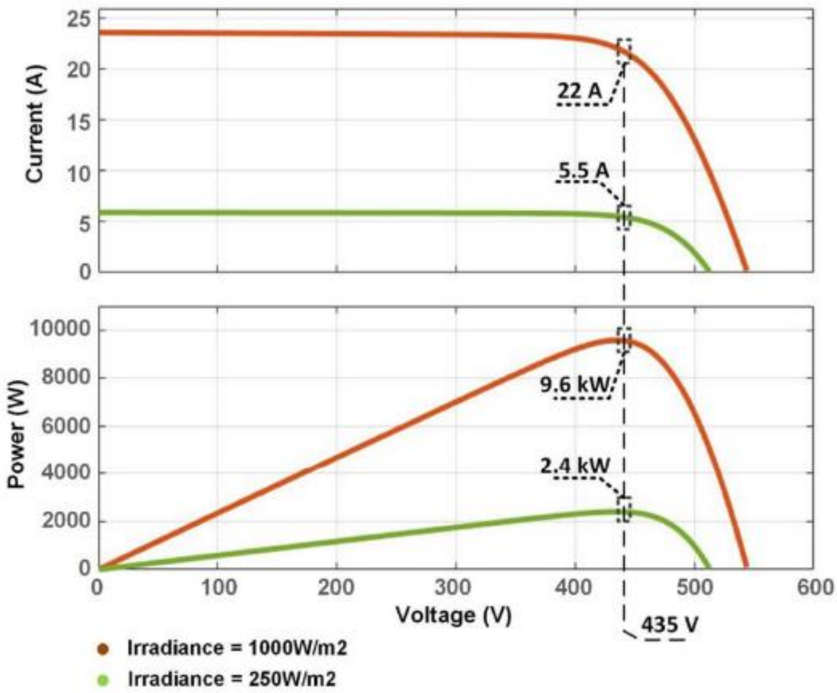


**Figure 5.5** 1STH-215-P PV Modules Characteristics

Table 6 displays the qZ_iMPC parameters. Two case studies are used to test the provided system, and they are compiled in Table 7. In order to confirm that the suggested system can handle all modes, case studies are created in this manner.

**Table 6.** Parameters of the qZ_iMPC

| System | Parameter | Value |
|---|---|---|
| **PV** | Maximum Power (1000 W/m$^2$) | 9.6 kW |
| | MPP Voltage (1000 W/m$^2$) | 435 Vdc |
| | MPP Current ( 1000 W/m$^2$) | 22 A |
| | Maximum Power ( 250 W/m$^2$) | 2.4 kW |
| | MPP Voltage ( 250 W/m$^2$) | 435 Vdc |
| | MPP Current ( 250 W/m$^2$) | 5.5 A |
| | PV Capacitor ( $C_{pv}$ ) | 300 µF |

**Table 6.** Parameters of the qZ_iMPC (Continued)

| **ESU** | **Capacity of Battery** | **60 Ah** |
|---|---|---|
| | Nominal Voltage of Battery | 200 Vdc |
| | Maximum Charge Current of Battery | 30 A |
| | Rated Capacitance of Supercapacitor | 1 F |
| | Rated Voltage of Supercapacitor | 10 Vdc |
| | Number of Series Capacitor of Supercapacitor | 4 |
| | Number of Parallel Capacitor of Supercapacitor | 1 |
| **quasi-Z-Source converter** | quasi-Z-Source Inductor ($L_{q1}$, $L_{q2}$) | 1 mH |
| | quasi-Z-Source Capacitor ($C_{q1}$, $C_{q2}$) | 100 µF |
| **General** | DC-Link Capacitor ($C_{out}$) | 1000 µF |
| | Nominal DC Link Voltage | 350 Vdc |
| | Switching Frequency | 20 kHz |
| | Transformer Turns Ratio | 1:1:1 |

**Table 7.** Case Studies of the qZ_iMPC Details

| | **Case 1** | | **Case 2** | |
|---|---|---|---|---|
| | 0 – 0.5 s | 0.5 – 1 s | 0 – 0.12 s | 0.12 – 0.5 s |
| **Irradiation** | 1000 $W/m^2$ | 250 $W/m^2$ | 1000 $W/m^2$ | 250 $W/m^2$ |
| **Temperature** | 25 C° | 25 C° | 25 C° | 25 C° |
| **EM Request** | 5000 W | 5000 W | -3000 W | -3000 W |
| **ESU Charging/Discharging** | Charging | Discharging | Charging (CC) | Charging (CV) |
| **Mode Transition** | Mode 1 | Mode 2 | Mode 3 | Mode 3 |

The first scenario is supported by modes 1 and 2, together with dynamic reactions during the transition these among the two modes. Mode 1 is represented by the time range 0-0.5 s under conditions of 1000 W/m2 illumination, 25 °C, and 5 kW EM demand. Figure 5.6 displays the suggested system steady-state and dynamic responses for case 1. The EM power consumption is more than the instantaneous PV power. As a result, the DC-link controller uses PV to regulate the EM DC-link. As seen in Figure 5.6, the DC-link is maintained under the appropriate voltage value, and the EM power requirements are met. The charge power of an ESU is equal to the difference there among the EM request and the PV's instantaneous power. It is evident that the PV, ESU, and EM have instantaneous power levels of 9.58, 4.2, and 5 kW, respectively. Because the quantity of PV power that can be communicated to the ESU is limited, the ESU is charged using its nominal charge current, as seen in Figure 5.6.

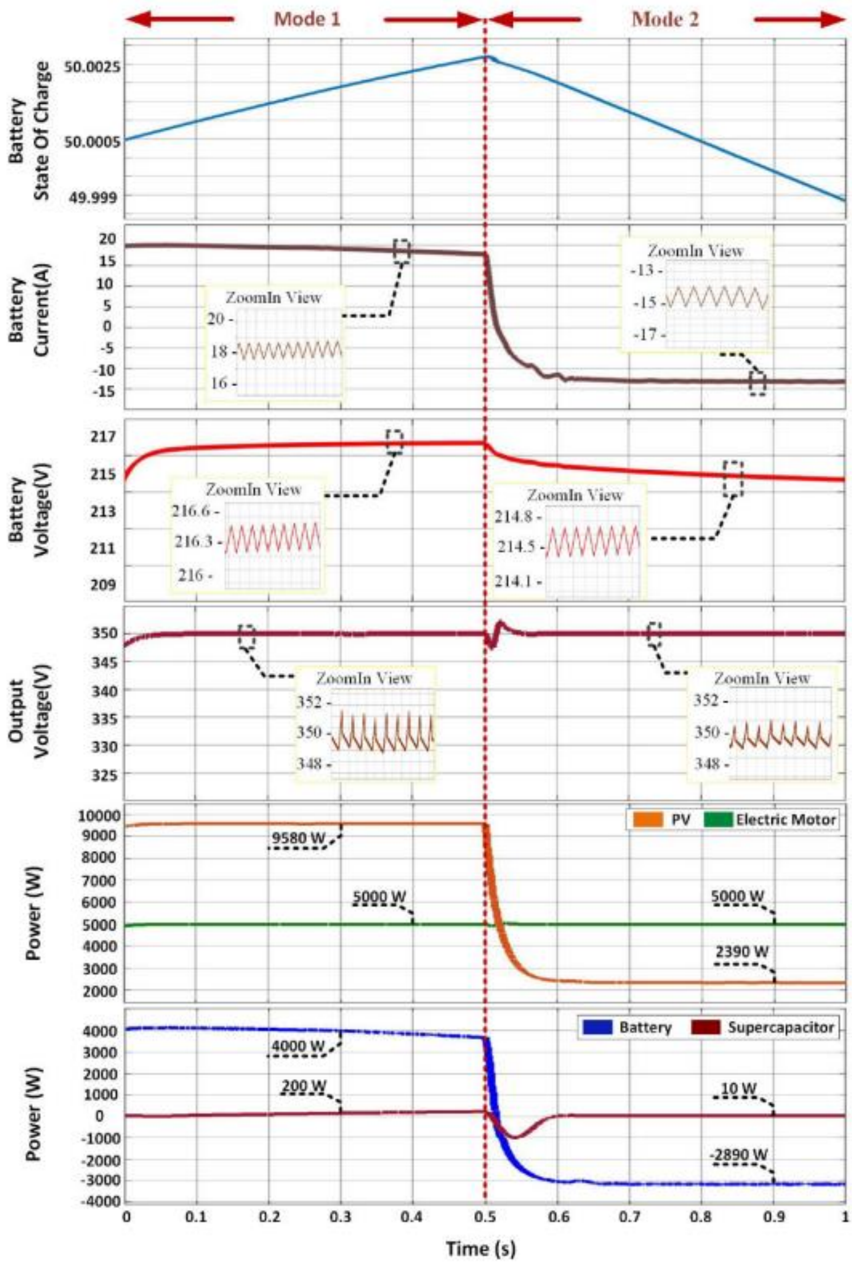


**Figure 5.6** Results for case 1 of qZ_iMPC

The abrupt reduction in PV irradiation from 1000 W/m2 to 250 W/m2 is evidence of the standalone system dynamic performance. With 250 W/m2 of irradiation, a temperature of 25 degrees, and a 5 kW EM demand, the time range of 0.5–1 s reflects mode 2. The PV generating power is insufficient to provide the EM at this moment in time. PV cannot maintain a consistent DC-link voltage. As seen in Figure 5.6, the DC-link is maintained constant while ESU buffers the power shortage. It is obvious that the PV, ESU, and EM have instantaneous power levels of

2.39, 2.88, and 5 kW, respectively. As a result, the ESU is run in discharge mode. Following the abrupt shift in PV irradiation, the supercapacitor discharges in milliseconds. The P&O MPPT controller continually monitors the highest power point in the current two time periods with output voltage of 435 V and output current of 22 and 5.5 A, respectively.

The second situation fits mode 3. The braking power is now delivered to ESU since it is not possible to transfer electricity to PV. The qZ_iMPC steady-state and dynamic responses for scenario 2 are depicted in Figure 5.7. The CC charging of the ESU unit for 3 kW of braking power is represented by the time range from 0.00 to 0.12 seconds. Until it enters CV mode, as shown in Figure 5.7, the charging current stays constant at its maximum permitted value. It is obvious that 12.5 A is the charging current. The voltage of the ESU linearly rises with the braking power throughout the present time interval. The controller enters the CV charging mode when the battery voltage hits the threshold level. The ESU unit CV charging for 3 kW of braking power is represented by the time range of 0.12–0.5 s. The charging current reduces depending on the battery condition, as shown in Figure 5.7.

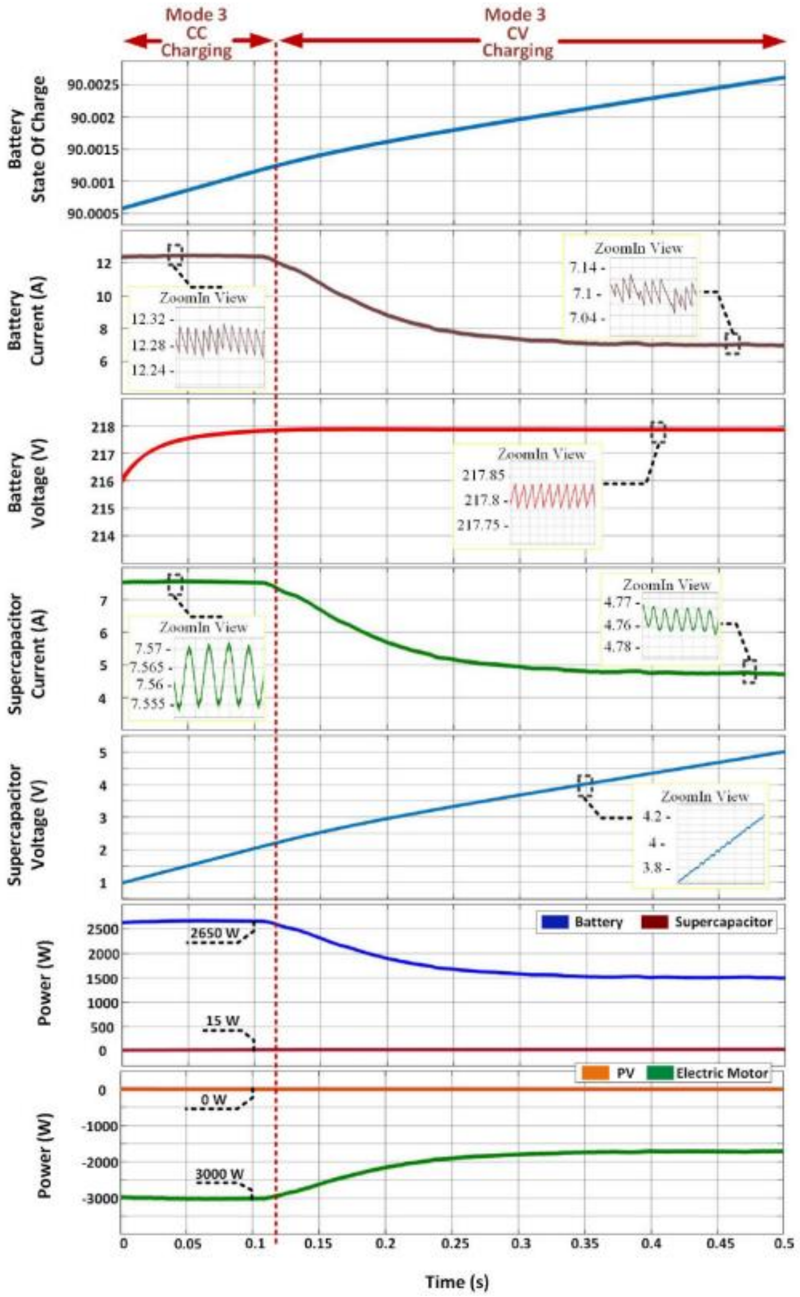


**Figure 5.7** Results for case 2 of qZ_Impc

For cases 1, 2, and 3, the quantity of electrical power generated by the PV and the amount of absorbed/injected power from the EM are taken into consideration during the efficiency study of the qZ_iMPC. Figures 5.6 and 5.7 demonstrate that the qZ_iMPC has efficiency values of 96.03, 94.87, and 88.83% for instances 1, 2, and 3, in turn. The findings show that the proposed approach is extremely efficient.

## 5.4. Resonant Tank Integrated Isolated Quasi Z-Source Multiport Converter

The performance assessment of the suggested converter is shown in this section. A proof-of-concept model with a power circuit and control strategy, as shown in Figure 5.8, has been created in PSIM in order to evaluate its performance. The qZ_RiMPC has been built with a 10 kW power rating, 15 kHz switching frequency, 435 V PV voltage, 333 V battery voltage, 16 V supercapacitor voltage, and 350 V output voltage.

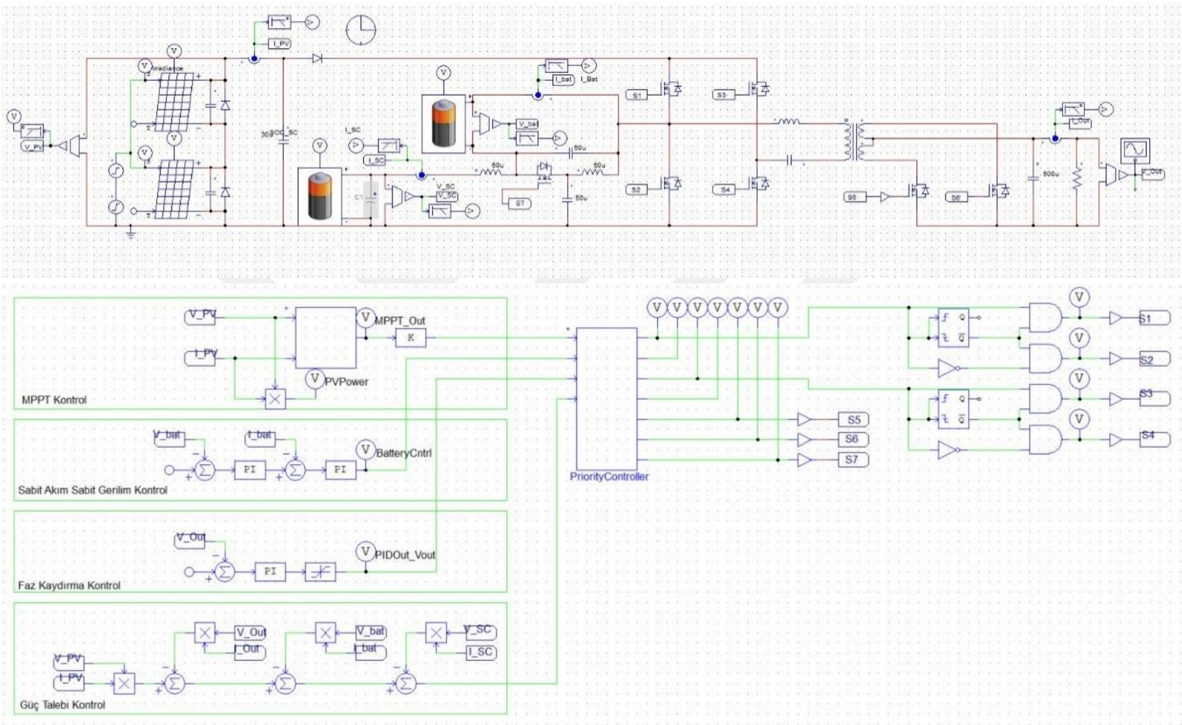


**Figure 5.8.** Proof-of-concept model of qZ_RiMPC (PSIM)

9.6 kW PV module 1STH-215-P from Soltech, a battery pack with a 66 Ah rating, and a supercapacitor pack with a 1 F rating are all installed in the input ports of the qZ_RiMPC. In Figure 5.9, the typical curves of PV (with constant temperature) are depicted. The characteristics of the key components used in the qZ_RiMPC, as well as the specifications of the input/output ports, are shown in Table 8. Utilizing a discrete solver with a 2 MHz sample frequency, the analysis was carried out. Two case studies with transient and steady-state settings are evaluated in order to validate the qZ_RiMPC performance. The results are described in Table 9. The examples are made to allow testing of all the qZ_RiMPC operational modes. The second scenario is about mode 3, whereas the first is about modes 1 and 2, as well as dynamic reactions while transitioning between the two modes.

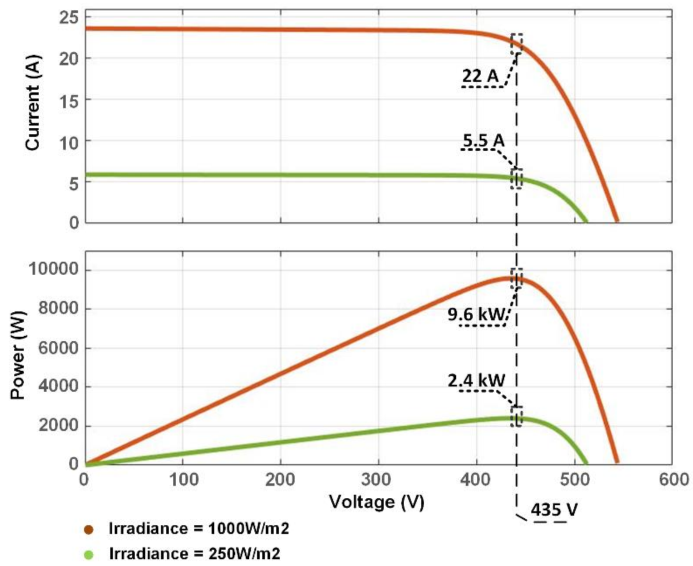

**Figure 5.9.** Characteristic curves of PV

**Table 8.** Parameters of the qZ_RiMPC

| System | Parameter | Value |
|---|---|---|
| **PV** | Maximum Power (1000W/m$^2$) | 9.6 kW |
| | MPP Voltage (1000W/m$^2$) | 435 V |
| | MPP Current (1000W/m$^2$) | 22 A |
| | Maximum Power (250W/m$^2$) | 2.4 kW |
| | MPP Voltage (250W/m$^2$) | 435 V |
| | MPP Current (250W/m$^2$) | 5.5 A |
| | PV Capacitor ($C_{pv}$) | 300 uF |
| **Energy Storage Unit** | Capacity of Battery | 66 Ah |
| | Nominal Voltage of Battery | 333 V |
| | Maximum Charge Current of Battery | 33 A |
| | Rated Capacitance of Supercapacitor | 1 F |
| | Rated Voltage of Supercapacitor | 16 V |
| | Number of Series Capacitor of Supercapacitor | 4 |
| | Number of Parallel Capacitor of Supercapacitor | 1 |
| **Quasi Z-Source Converter** | Quasi Z-Source Inductors ($L_{q1}$,$L_{q2}$) | 1 mH |
| | Quasi Z-Source Capacitors ($C_{q1}$,$C_{q2}$) | 100 uF |
| **General** | DC-Link Capacitor ($C_{out}$) | 1000 uF |
| | Nominal DC Link Voltage | 350 V |
| | Switching Frequency | 20 kHz |
| | Transformer Turns Ratio | 1:1:1 |

**Table 9.** Case Studies of qZ_RiMPC Details

| | Case 1 | | | Case 2 |
|---|---|---|---|---|
| **Time** | **0 – 0.05 s** | **0.05 – 0.11 s** | **0.11 – 0.16 s** | **0 – 0.12 s** |
| **Irradiation** | 500 W/m$^2$ | 250 W/m$^2$ | 1000 W/m$^2$ | 1000 W/m$^2$ |
| **Temperature** | 25 C$^o$ | 25 C$^o$ | 25 C$^o$ | 25 C$^o$ |
| **Load Demand** | 5000 W | 5000 W | 5000 W | -5900 W |
| **Battery Charging/Discharging** | Discharging | Discharging | Charging | Charging (CC) |
| **Supercapacitor Charging/Discharging** | Discharging | Charging | Charging | Charging |
| **Mode Transition** | Mode 1 | Mode 2 | Mode 1 | Mode 3 |

The evaluation of performance starts with the load receiving constant power. PV and battery/supercapacitor storage units may be utilized for this purpose as energy units, and if PV has extra energy, PV can be used as an energy unit and the storage unit can be used as a power-transferred load group. The waveforms of the battery/supercapacitor SOC, output voltage, and power ratings for all ports are displayed in Figure 5.10 under conditions of constant load consumption and variable irradiation. Energy storage units are utilized as a buffer to make up for the absence of PV power when power is transmitted from the PV to the load within the time range of 0-0.05 s, which represents mode 2. Using an MPPT control loop, the PV system generates 3.56 kW with a 500 W/m$^2$ irradiation, while the battery and supercapacitor generate 1.11 kW and 0.67 kW, respectively, using a DC Link control loop. As a result, the storage units are discharged, as illustrated in Figure 5.10. As a result, the load receives constant power supply, and the output DC-Link stays constant. To continuously supply electricity to the load, mode 2 with restricted PV generation is likewise represented by the time range of 0.05-0.11 s. However, when operating in this mode, some power flow directions have changed. As seen in Figure 5.10, PV generates 1.76 kW at a 250 W/m$^2$ irradiance, and the battery buffers it with 4.4 kW to supply the load with a steady output voltage and to charge the supercapacitor pack that can stabilize the system under transient situations. It is evident that the instantaneous SOC value for the supercapacitor pack is increasing (charging), whilst it is decreasing (discharging) for the battery. Due to irradiation of 1000 W/m$^2$, the time range of 0.11–0.16 s indicates mode 1, in which power is delivered from the PV to both the load and energy storage devices. The load request is more than the instantaneous PV power. As a result, PV powers the load continuously while also recharging energy storage devices. According to Figure 8, the load power requirements are met, the DC Link voltage is maintained constant at the required level, and the battery and supercapacitor pack are charged throughout the present time interval. It is obvious that the PV, battery, supercapacitor, and load have instantaneous power values of 9.57, 4.24, 0.05, and 5 kW, respectively. With abrupt fluctuations in PV radiation in scenario 1, the qZ_RiMPC dynamic performance has also been confirmed. The state detection and controller loop transition durations, as illustrated in Figure 5.10, generate instantaneous voltage fluctuations at point-of-irradiation changes, which the controller smooth adjusts for.

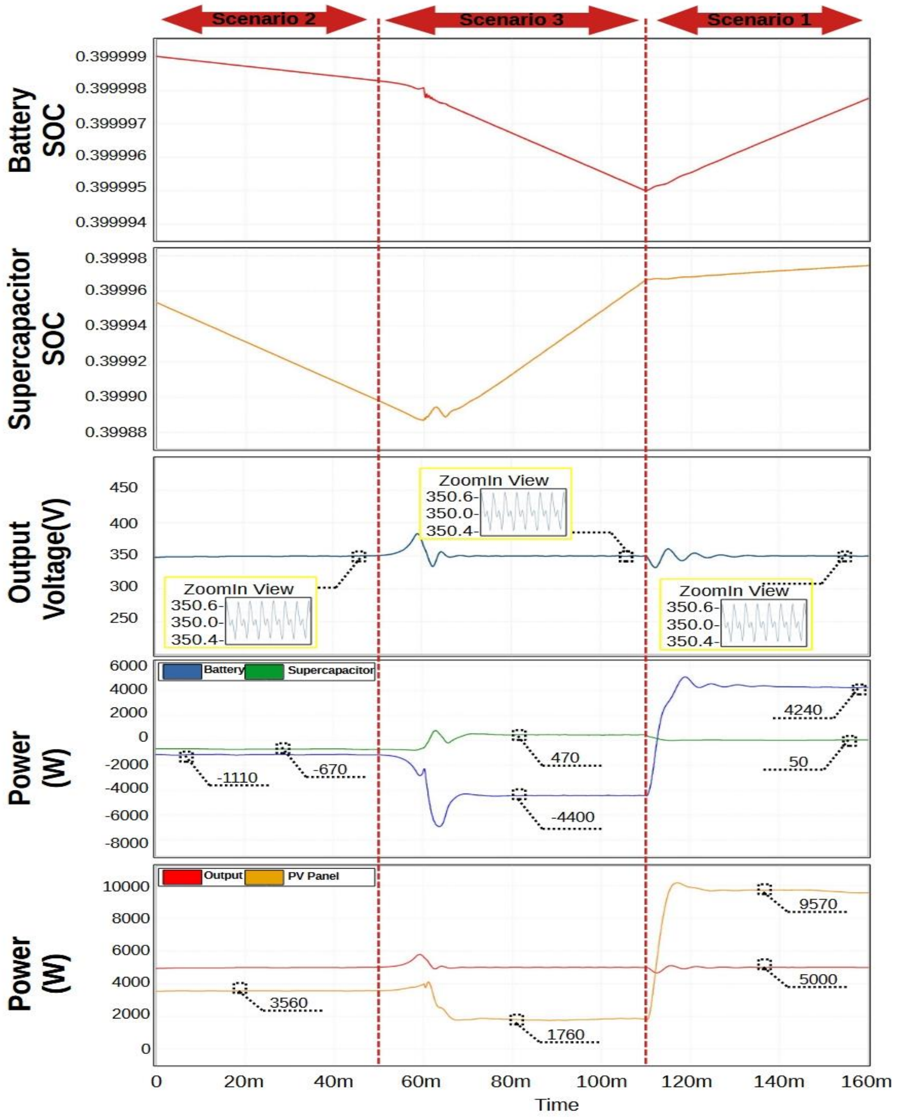


**Figure 5.10.** Performance results of case 1 of qZ_RiMPC

Reverse power transfer, or mode 3, has been carried out in instance 2. In the present mode, the qZ_RiMPC suggested bidirectional power flow capability has been used to charge the storage units from DC Link. The rapid battery power values, supercapacitor, and DC Link are 5.4, 0.05 and 5.9 kW, respectively, as can be seen from Figure 5.10. Storage units are charged with continuous currents of 4.4 A for the supercapacitor and 15 A for the battery during the reverse power flow operation. The switch from the CC to the CV control loop has also been made for reverse power flow operation. The performance outcomes of the relevant condition are shown in Figure 5.11. The charging current stays constant at its maximum permissible value until it enters CV mode, as shown in Figure 5.11. It is obvious that 15 A is being used for charging. The battery voltage rises linearly with the reverse power flow throughout the present time interval. The controller enters the CV charging mode when the battery voltage hits the threshold level. The charging current diminishes exponentially as the battery condition changes, as seen in Figure 5.11.

The system efficiency of the qZ_RiMPC is also assessed. The instantaneous power ratings of ports from Figures 5.10 and 5.11 have been used to calculate the efficiency values for various operating modes. It can be shown that in instance 1, an efficiency of at least 91% is reached in the time range of 0.05-0.11 s, and that efficiency increases to 97% in the range of 0–0.05 s. It has been noted that the system operates at an average efficiency of 95% or higher.

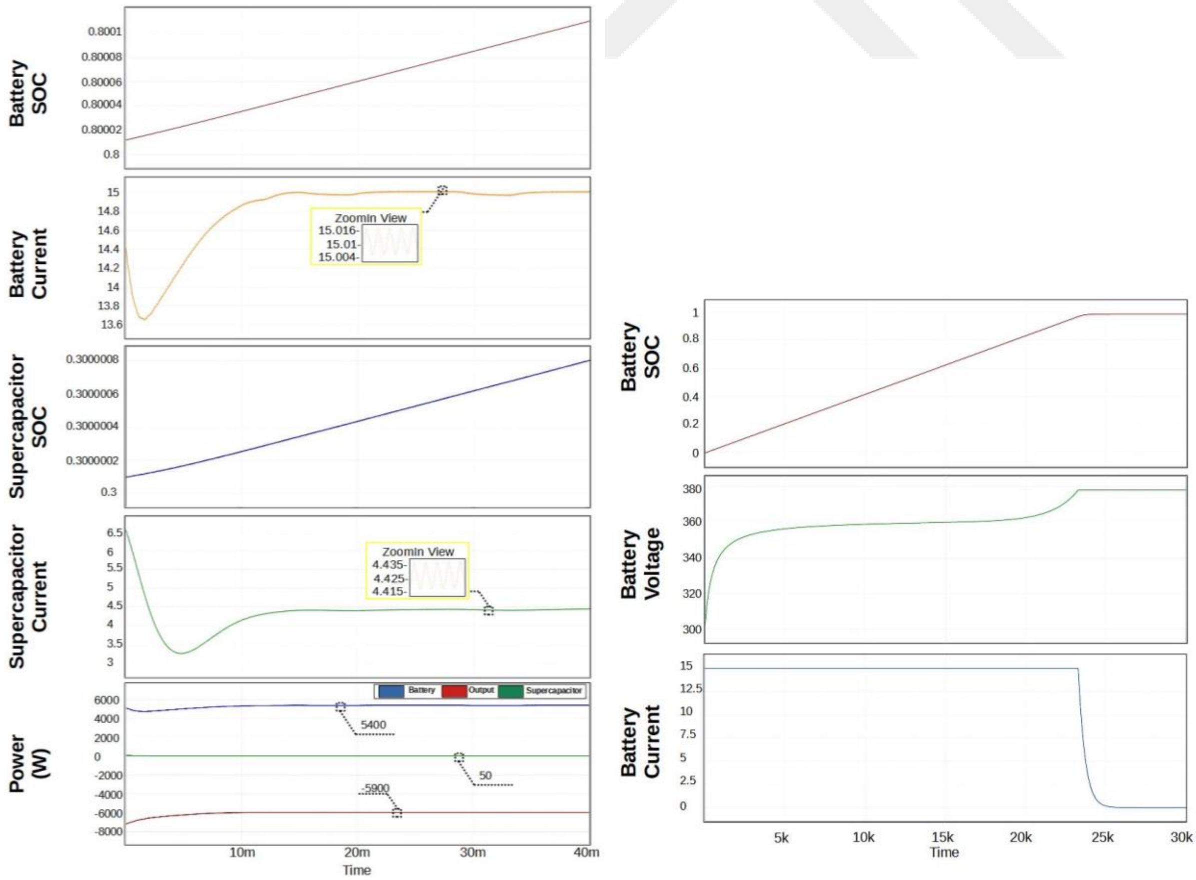


**Figure 5.11.** Performance results of case 2 of qZ_RiMPC

# 6. RESULTS AND DISCUSSIONS

Table 10 compares the four proposed topologies with existing MPC topologies and among themselves in terms of efficiency, number of ports, switches number and potential bidirectional power flow modes. The application areas of multi-port converters are characterized by simplified switch architecture, high efficiency, and power flow characteristics. All multiport converters developed in this thesis are characterized by their high efficiency and simple switch architecture. In the simulation programs of the circuit topologies designed within the scope of the simulation studies carried out at this point, only switching element losses are taken into account, ignoring transformer, coil and conduction losses.

**Table 10.** Comparison of conventional converters and the proposed multiport converters

| Model | Port Number | Number of Switches | Efficiency % | Bidirectional Port |
|---|---|---|---|---|
| **Transformer Coupled Half Bridge [25]** | 3 | 6 | 91.5 | ESU |
| **Transformer Coupled Full Bridge [27]** | 3 | 12 | 91 | ESU |
| **Half Bridge [24]** | 3 | 4 | 94 | ESU |
| **Full Bridge [21]** | 3 | 8 | 91 | ESU |
| **Full Bridge Interleaved [42]** | 4 | 8 | 96 | ESU |
| **Interleaved Based Isolated Multiport Converter** | 4 | 4 | 98 | ESU |
| **Switch Capacitor Based Isolated Multiport Converter** | 3 | 5 | 96.8 | ESU, Load |
| **Quasi Z-Source Multiport Converter** | 4 | 6 | 96 | ESU, Load |
| **Resonant Tank Integrated Isolated Quasi Z-Source Multiport Converter** | 4 | 5 | %97 | ESU |

The various multiport converter types discussed in this thesis each have their own benefits and drawbacks. The control and power circuits of the converters, however, may be able to offset each others drawbacks.  A novel interleaved bidirectional multiport isolated DC-DC converter with an effective control strategy is suggested in Interleaved Based Isolated Multiport Converter for operation with PVs and batteries. These are the benefits of this model:

i) There are many input ports for different power generation/storage units, and there are two separate output ports.
ii) Low voltage battery integration without the use of extra converters or switching components.
iii) The converter having few switching components and it is cost effective.
iv) The multi-loop control mechanism that enables immediate loop transition.

In addition to these benefits, a topology that can drive two distinct motors coupled to load sites is suggested considering the accessibility of EVs. However, the converter is not able to transfer braking energy to the battery. As a result, during nighttime when there is no radiation, and when the battery is completely discharged, uninterrupted power supply to the loads cannot be ensured. The related power flow can be performed by a switch-capacitor-based isolated multiport converter. The power circuit and control algorithm of switch capacitor based isolated multiport converter eliminates this drawback.

Switch capacitor based isolated multiport converter is composed of a half-bridge converter and a switched capacitor converter with an effective control strategy. The following are some benefits of the suggested converter:

i) Low voltage PV integration with a switched capacitor DC-DC converter with a high voltage gain and efficiency,
ii) battery integration without the need of an extra converter,
iii) cost effectiveness,
iv) the ability to transmit power in both directions.

However, to integrate the relevant ports and provide the necessary power flow scenarios, the switch-capacitor converter and the half-bridge converter, in other words, two separate power circuits, need to be integrated. As a result, a larger number of switching components is required.

To address this issue, another proposed topology in the thesis, qZ_iMPC, is capable of fulfilling the functions of two separate converters using a single switching element.

Integrating four ports with a simplified switch converter architecture is the system key superiority of the qZ_iMPC design. Additionally, the suggested converter offers a significant voltage gain at low battery/supercapacitor voltages and lower duty cycle. Additionally, it enables low turn ratio transformer design, increasing HFT efficiency. As a result, the voltage spikes brought on by the HFT leakage inductance are diminished. The suggested architecture has the following functionalities:

(i) PV and ESU continuously supply power to the EM;
(ii) PV charges battery/supercapacitor packs when EM demand is less than instantaneous PV power; and
(iii) EM braking energy charges battery/supercapacitor packs.

Various operating scenarios have been used to test the system's performance. The suggested system, which employs all control techniques including CC/CV charging, MPPT, and DC-Link control, executes all power flow changes between the ports. The outcomes and efficiency figures for many scenarios support the usability of the suggested approach.

The proposed final multiport DC-DC converter topology in the thesis allows for a high-gain, high-efficiency, and supercapacitor-independent charging/discharging capability by leveraging the advantages of both the quasi-z-source converter and the resonant converter. The qZ_RiMPC topology performs the following tasks:

(i) DC-Link is continually powered by PV and ESUs,
(ii) When the power depletion of the load connected to the DC-Link is less than the power generated by the PV panel, the PV panel charges the battery and supercapacitor.
(iii) The utilization of a bidirectional quasi z-source allows for asynchronous charging of the battery and supercapacitor. This allows the supercapacitor to manage the initial inrush current before preparing for the next inrush current while the battery is being depleted.

With testing-ready operating modes, the qZ_RiMPC architecture manages power flow for CC/CV charging, MPPT, DC-Link regulation, and supercapacitor charge/discharge control methods. The system efficiency and the viability of the technique are supported by the simulation findings.

# 7. CONCLUSION

Grid-connected or independent systems have begun to be developed together with renewable energy systems. ESU are also included into renewable energy systems to guarantee the systems' continuity and long-term functioning. Multiport converters are required for this integration to incorporate various power flows and control algorithms. At this stage, it is necessary to combine many independent power circuits to charge and discharge batteries, track the maximum power point of renewable energy systems, and implement various power scenarios. However, this condition significantly raises the cost. Also, with the global chip crisis still going on, the usage of various power circuits limits continuity due to the decline in ICs, switching element, and microcontroller manufacture.

Multiport converters are now widely utilized in renewable energy systems, energy storage systems, and systems with several load groups. Multiport converters, however, require sophisticated control algorithms to manage power flow, track the maximum power point, and regulate battery charging and discharge.

In this thesis, four different multiport converter power circuits and control schemes have been developed in which RESs, ESUs and loads are integrated. Such integrated energy systems are becoming increasingly important to meet increasing energy demands and reduce environmental impacts. The proposed topologies offer cost-effective solutions by reducing the number of switching elements used in conventional MPC topologies. The control of RESs and ESUs is challenging due to the complex control algorithms (MPPT, CC, CV, DC-Link) required by MPC. However, these challenges have been overcome in the studies and harmonization with RESs and ESUs has been achieved. In this way, it is possible to maximize power from RESs and efficiently manage energy storage units. Performance analyses of the developed models have been carried out extensively. These analyses have shown that the models exhibit high performance and efficiency.

# REFERENCES


[1] M. M. Savrun, “Z-source converter integrated dc electric spring for power quality improvement in dc microgrid,” *Eng. Sci. Technol. an Int. J.*, vol. 24, no. 6, pp. 1408–1414, 2021, doi: 10.1016/j.jestch.2021.05.004.

[2] M. Das and V. Agarwal, “Design and Analysis of a High-Efficiency DC-DC Converter with Soft Switching Capability for Renewable Energy Applications Requiring High Voltage Gain,” *IEEE Trans. Ind. Electron.*, vol. 63, no. 5, pp. 2936–2944, 2016, doi: 10.1109/TIE.2016.2515565.

[3] I. N. Jiya, H. Van Khang, N. Kishor, and R. M. Ciric, “Novel Family of High-Gain Nonisolated Multiport Converters with Bipolar Symmetric Outputs for DC Microgrids,” *IEEE Trans. Power Electron.*, vol. 37, no. 10, pp. 12151–12166, 2022, doi: 10.1109/TPEL.2022.3176688.

[4] K. Suresh et al., "A Multifunctional Non-Isolated Dual Input-Dual Output Converter for Electric Vehicle Applications," in IEEE Access, vol. 9, pp. 64445-64460, 2021, doi: 10.1109/ACCESS.2021.3074581.

[5] G. Waltrich, J. L. Duarte and M. A. M. Hendrix, "Multiport converter for fast charging of electrical vehicle battery: Focus on DC/AC converter," IECON 2011 - 37th Annual Conference of the IEEE Industrial Electronics Society, Melbourne, VIC, Australia, 2011, pp. 3626-3633, doi: 10.1109/IECON.2011.6119898.

[6] M. M. Savrun, M. İnci, and M. Büyük, “Design and analysis of a high energy efficient multi-port dc-dc converter interface for fuel cell/battery electric vehicle-to-home (V2H) system,” *J. Energy Storage*, vol. 45, no. December 2021, 2022, doi: 10.1016/j.est.2021.103755.

[7] Q. Sun, H. Xie, X. Liu, F. Niu and C. Gan, "Multiport PV-Assisted Electric-Drive-Reconstructed Bidirectional Charger With G2V and V2G/V2L Functions for SRM Drive-Based EV Application," in IEEE Journal of Emerging and Selected Topics in Power Electronics, vol. 11, no. 3, pp. 3398-3408, June 2023, doi: 10.1109/JESTPE.2023.3240434.

[8] T. R. Choudhury, B. Nayak, A. De, and S. B. Santra, “A comprehensive review and feasibility study of DC–DC converters for different PV applications: ESS, future residential purpose, EV charging,” *Energy Syst.*, vol. 11, no. 3, pp. 641–671, 2020, doi: 10.1007/s12667-019-00331-5.

[9] S. Alatai *et al.*, “A review on state-of-the-art power converters: Bidirectional, resonant, multilevel converters and their derivatives,” *Appl. Sci.*, vol. 11, no. 21, 2021, doi: 10.3390/app112110172.

[10] B. G. Dobbs and P. L. Chapman, “A Multiple-Input DC-DC Converter Topology,” vol. 1, no. 1, pp. 6–9, 2003.

[11] W. Jiang and B. Fahimi, “Multi-port Power Electric Interface for renewable energy sources,” *Conf. Proc. - IEEE Appl. Power Electron. Conf. Expo. - APEC*, pp. 347–352, 2009, doi: 10.1109/APEC.2009.4802680.

[12] W. Jiang and B. Fahimi, “Multiport Power Electronic Interface — Concept ,” *Power*, vol. 26, no. 7, pp. 1890–1900, 2011.

[13] V. A. K. Prabhala, P. Fajri, V. S. P. Gouribhatla, B. P. Baddipadiga, and M. Ferdowsi, “A DC-DC Converter with High Voltage Gain and Two Input Boost Stages,” *IEEE Trans. Power Electron.*, vol. 31, no. 6, pp. 4206–4215, 2016, doi: 10.1109/TPEL.2015.2476377.

[14] “H. Wu, J. Zhang and Y. Xing, "A Family of Multiport Buck–Boost Converters Based on DC-Link-Inductors (DLIs)," in IEEE Transactions on Power Electronics, vol. 30, no. 2, pp. 735-746, Feb. 2015, doi: 10.1109/TPEL.2014.2307883.”

[15] B. Chandrasekar *et al.*, “Non-Isolated High-Gain Triple Port DC-DC Buck-Boost Converter with Positive Output Voltage for Photovoltaic Applications,” *IEEE Access*, vol. 8, pp. 113649–113666, 2020, doi: 10.1109/ACCESS.2020.3003192.

[16] T. Kim and S. Kwak, “Single pole switch leg based multi-port converter with an energy storage,” *IET Power Electron.*, vol. 9, no. 6, pp. 1322–1330, 2016, doi: 10.1049/iet-pel.2015.0578.

[17] Z. Qian, S. Member, O. Abdel-rahman, and I. Batarseh, “An Integrated Four-Port DC / DC Converter,” *Power*, vol. 25, no. 7, pp. 1877–1887, 2010.

[18] Z. Jianwu, Q. Wei, Q. Liyan, and Y. Jiao, “An isolated multiport DC-DC converter for simultaneous power management of multiple different renewable energy sources,” *IEEE J. Emerg. Sel. Top. Power Electron.*, vol. 2, no. 1, pp. 70–78, 2014, doi: 10.1109/JESTPE.2013.2293331.

[19] H. Al-atrash and I. Batarseh, “Boost-Integrated Phase-Shift Full-Bridge Converter for Three-Port Interface,” pp. 2313–2321, 2007.

[20] J. Hong, J. Yin, Y. Liu, J. Peng and H. Jiang, "Energy Management and Control Strategy of Photovoltaic/Battery Hybrid Distributed Power Generation Systems With an Integrated Three-Port Power Converter," in IEEE Access, vol. 7, pp. 82838-82847, 2019, doi: 10.1109/ACCESS.2019.2923458.

[21] K. Itoh, M. Ishigaki, N. Yanagizawa, S. Tomura, and T. Umeno, “Analysis and Design of a Multiport Converter Using a Magnetic Coupling Inductor Technique,” *IEEE Trans. Ind. Appl.*, vol. 51, no. 2, pp. 1713–1721, 2015, doi: 10.1109/TIA.2014.2354401.

[22] H. Wu, K. Sun, R. Chen, H. Hu, and Y. Xing, "Full-bridge three-port converters with wide input voltage range for renewable power systems," *IEEE Trans. Power Electron.*, vol. 27, no. 9, pp. 3965–3974, 2012, doi: 10.1109/TPEL.2012.2188105.

[23] J. Zeng, W. Qiao, and L. Qu, "An Isolated Three-Port Bidirectional DC-DC Converter for Photovoltaic Systems With Energy Storage," *IEEE Trans. Ind. Appl.*, vol. 51, no. 4, pp. 3493–3503, 2015, doi: 10.1109/TIA.2015.2399613.

[24] H. Zhu, D. Zhang, H. S. Athab, B. Wu, and Y. Gu, "PV isolated three-port converter and energy-balancing control method for PV-battery power supply applications," *IEEE Trans. Ind. Electron.*, vol. 62, no. 6, pp. 3595–3606, 2015, doi: 10.1109/TIE.2014.2378752.

[25] L. Wang, Z. Wang, and H. Li, "Asymmetrical duty cycle control and decoupled power flow design of a three-port bidirectional DC-DC converter for fuel cell vehicle application," *IEEE Trans. Power Electron.*, vol. 27, no. 2, pp. 891–904, 2012, doi: 10.1109/TPEL.2011.2160405.

[26] D. Liu and H. Li, "A ZVS bi-directional DC-DC converter for multiple energy storage elements," *IEEE Trans. Power Electron.*, vol. 21, no. 5, pp. 1513–1517, 2006, doi: 10.1109/TPEL.2006.882450.

[27] M. Phattanasak, R. Gavagsaz-Ghoachani, J. P. Martin, B. Nahid-Mobarakeh, S. Pierfederici, and B. Davat, "Control of a hybrid energy source comprising a fuel cell and two storage devices using isolated three-port bidirectional DC-DC converters," *IEEE Trans. Ind. Appl.*, vol. 51, no. 1, pp. 491–497, 2015, doi: 10.1109/TIA.2014.2336975.

[28] D. C. D. C. Converter, "Dual-Transformer-Based Asymmetrical Triple-Port Active Bridge ( DT-ATAB ) Isolated," vol. 64, no. 6, pp. 4549–4560, 2017.

[29] E. Asa, K. Colak, M. Bojarski, and D. Czarkowski, "Asymmetrical Duty-Cycle and Phase-Shift Control of a Novel Multiport CLL Resonant Converter," *IEEE J. Emerg. Sel. Top. Power Electron.*, vol. 3, no. 4, pp. 1122–1131, 2015, doi: 10.1109/JESTPE.2015.2408565.

[30] D. C. D. C. Converter, "Distributed Impedance Network ( Z-Network )," *Power*, vol. 25, no. 11, pp. 2722–2733, 2010.

[31] G. Sen and M. E. Elbuluk, "Voltage and current-programmed modes in control of the z-source converter," *IEEE Trans. Ind. Appl.*, vol. 46, no. 2, pp. 680–686, 2010, doi: 10.1109/TIA.2010.2040054.

[32] J. M. Sandoval, V. Cardenas, M. A. Barrios, M. G. Garcia, and J. Alcala, "Multiport isolated link with current-fed z-source converters to manage power imbalance in PV applications," *Electron.*, vol. 9, no. 2, 2020, doi: 10.3390/electronics9020280.

[33] S. Harini, N. Chellammal, B. Chokkalingam, and L. Mihet-Popa, “A Novel High Gain Dual Input Single Output Z-Quasi Resonant (ZQR) DC/DC Converter for Off-Board EV Charging,” *IEEE Access*, vol. 10, no. August, pp. 83350–83367, 2022, doi: 10.1109/ACCESS.2022.3195936.

[34] H. Li and Z. Jiang, “On Automatic Resonant Frequency Tracking in LLC Series Resonant Converter Based on Zero-Current Duration Time of Secondary Diode,” *IEEE Trans. Power Electron.*, vol. 31, no. 7, pp. 4956–4962, 2016, doi: 10.1109/TPEL.2015.2462086.

[35] M. Salem *et al.*, “Three-Phase Series Resonant DC-DC Boost Converter with Double LLC Resonant Tanks and Variable Frequency Control,” *IEEE Access*, vol. 8, pp. 22386–22399, 2020, doi: 10.1109/ACCESS.2020.2969546.

[36] Y. K. Lo, C. Y. Lin, M. T. Hsieh, and C. Y. Lin, “Phase-shifted full-bridge series-resonant DC-DC converters for wide load variations,” *IEEE Trans. Ind. Electron.*, vol. 58, no. 6, pp. 2572–2575, 2011, doi: 10.1109/TIE.2010.2058076.

[37] T. Sensui and H. Koizumi, “Load-Independent Class E2Parallel Resonant DC-DC Converter,” *IEEE Trans. Circuits Syst. II Express Briefs*, vol. 69, no. 11, pp. 4374–4378, 2022, doi: 10.1109/TCSII.2022.3194151.

[38] S. M. Tayebi, H. Hu, S. Abdel-Rahman, and I. Batarseh, “Dual-Input Single-Resonant Tank LLC Converter with Phase Shift Control for PV Applications,” *IEEE Trans. Ind. Appl.*, vol. 55, no. 2, pp. 1729–1739, 2019, doi: 10.1109/TIA.2018.2883015.

[39] Y. Wei, Q. Luo, and A. Mantooth, “Comprehensive Analysis and Design of LLC Resonant Converter With Magnetic Control,” *CPSS Trans. Power Electron. Appl.*, vol. 4, no. 4, pp. 265–275, 2019, doi: 10.24295/cpsstpea.2019.00025.

[40] J. Zeng, G. Zhang, S. S. Yu, B. Zhang, and Y. Zhang, “LLC resonant converter topologies and industrial applications -A review,” *Chinese J. Electr. Eng.*, vol. 6, no. 3, pp. 73–84, 2020, doi: 10.23919/CJEE.2020.000021.

[41] J. Ren, “A Nonisolated Multiport Converter Based on LLC and Bidirectional Buck/Boost for Low Power EH-Battery Systems,” *CPSS Trans. Power Electron. Appl.*, vol. 7, no. 2, pp. 196–205, 2022, doi: 10.24295/cpsstpea.2022.00018.

[42] H. Wu, J. Zhang, X. Qin, T. Mu and Y. Xing, "Secondary-Side-Regulated Soft-Switching Full-Bridge Three-Port Converter Based on Bridgeless Boost Rectifier and Bidirectional Converter for Multiple Energy Interface," in IEEE Transactions on Power Electronics, vol. 31, no. 7, pp. 4847-4860, July 2016, doi: 10.1109/TPEL.2015.2473002.